Journal of
Applied Physics

Electro-optic modulation in integrated photonics EP

Cite as: J. Appl. Phys. **130**, 010901 (2021); https://doi.org/10.1063/5.0048712
Submitted: 25 February 2021 . Accepted: 05 June 2021 . Published Online: 02 July 2021

Georgios Sinatkas, **Thomas Christopoulos**, **Odysseas Tsilipakos**, and **Emmanouil E. Kriezis**

COLLECTIONS

EP This paper was selected as an Editor's Pick

AIP Publishing

Journal of
Applied Physics

PERSPECTIVE

scitation.org/journal/jap

Electro-optic modulation in integrated photonics

Cite as: J. Appl. Phys. **130**, 010901 (2021); doi: 10.1063/5.0048712
Submitted: 25 February 2021 · Accepted: 5 June 2021 ·
Published Online: 2 July 2021

View Online Export Citation CrossMark

Georgios Sinatkas,[1] Thomas Christopoulos,[1] Odysseas Tsilipakos,[2] and Emmanouil E. Kriezis[1,a)]

AFFILIATIONS

[1] School of Electrical and Computer Engineering, Aristotle University of Thessaloniki, GR-54124 Thessaloniki, Greece
[2] Institute of Electronic Structure and Laser, Foundation for Research and Technology-Hellas (FORTH-IESL), GR-70013 Heraklion, Crete, Greece

[a)] **Author to whom correspondence should be addressed:** mkriezis@auth.gr

ABSTRACT

Electro-optic modulators are an indispensable part of photonic communication systems, largely dictating the achievable transmission rate. Recent advances in materials and fabrication/processing techniques have brought new elements and a renewed dynamic to research on optical modulation. Motivated by the new opportunities, this Perspective reviews the state of the art in integrated electro-optic modulators, covering a broad range of contemporary materials and integrated platforms. To provide a better overview of the status of current modulators, an assessment of the different material platforms is conducted on the basis of common performance metrics: extinction ratio, insertion loss, electro-optic bandwidth, driving voltage, and footprint. The main physical phenomena exploited for electro-optic modulation are first introduced, aiming to provide a self-contained reference to researchers in physics and engineering. Additionally, we take care to highlight topics that can be overlooked and require attention, such as the accurate calculation of carrier density distribution and energy consumption, the correct modeling of thin and two-dimensional materials, and the nature of contact electrodes. Finally, a future outlook for the different electro-optic materials is provided, anticipating the research and performance trends in the years to come.

I. INTRODUCTION

It has been over 50 years since early research developments in lightwave transmission systems and almost 45 since the first commercial deployments. The last 20 years have undoubtedly witnessed an explosive development of the field,[1,2] with the coming years anticipated to be equally bright. Light transmission systems penetrate the full spectrum of high-speed communications, from long-reach systems such as transoceanic links down to short-reach interconnects in datacenters[3,4] and on-chip optical interconnects.[5] The transmission capacity of such systems is mainly related to the optical modulation used, apart from various limiting factors imposed by the transmission channel and the associated impairments. In this respect, the optical modulator is one of the key elements, and research in this field has been very active ever since the emergence of optical communications. Publications on optical modulation exceeded 1000 per year since the early 1990s and are constantly above 5000 per year since 2010 (Scopus). Optical modulators constitute a multi-disciplinary field in which physics, materials science, engineering design, fabrication processes, and packaging are all of critical importance.

Optical modulators imprint an electrical signal on an optical wave, termed the optical carrier. Amplitude, phase, frequency, and polarization of the optical carrier and any combination of the above can be exploited for encoding the information. Modulators can be of integrated or free-space type: in the former category, the optical waves are guided modes in a photonic integrated circuit (PIC), whereas in the latter, they are free-space propagating beams. This Perspective will almost exclusively deal with modulation in integrated circuits, with the elementary structure being a waveguide. Free-space optical modulators are also of high importance to a broad range of applications and can be based on multi-layers, metasurfaces, diffraction gratings, or other free-space analogs.[6–11]

Optical modulation requires an electro-optic (EO) effect, which provides the necessary change in the optical properties of certain materials when subjected to electric fields of frequency substantially below that of the light wave. When the EO effect modifies the refractive index (equivalently, the real part of optical permittivity), the modulator is of electro-refraction type, and this is the case with the Pockels effect, the Kerr electro-optic (or DC Kerr) effect, and free-carrier dispersion (plasma effect).[12] On the other hand, when material losses are modified, the modulator is of electro-absorption type, and this is commonly provided by the Franz–Keldysh effect in bulk semiconductors, the quantum-confined Stark effect in quantum-well structures, and free-carrier absorption.[13–15] Electro-refraction modulators employ an interferometer (most commonly a Mach–Zehnder structure) or a resonator (such as a microring). Electro-absorption modulators are straight waveguide sections. In this Perspective, we will mainly cover external modulators and only shortly discuss direct modulation based on the III–V material system in Sec. V.

Modulator performance is typically quantified in terms of a number of metrics, which include the extinction ratio (ER), insertion losses (IL), electro-optic bandwidth (EO BW), optical bandwidth, linearity, driving voltage, energy consumption, chirp, and footprint.[12,15,16] ER quantifies the contrast between the high-transmission and low-transmission levels; it is a measure of the suppression (extinction) of the light wave when the modulator is in the non-transmissive state and should acquire values as high as possible. IL measures the losses suffered by the light wave when the modulator is in the high-transmission state and should acquire values as low as possible. EO BW is of utmost importance as it quantifies if the modulator can cope with rapid variations of the modulating electric signal; this directly relates to the highest bit rate that can be supported. The optical bandwidth corresponds to the wavelength range that allows for satisfactory modulation performance. Linearity is commonly quantified in terms of the spurious free dynamic range (SFDR), which is measured in a two-tone excitation. The driving voltage corresponds to the amplitude of the modulating signal, and for phase modulators, it is quantified with reference to the half-wave voltage, i.e., the necessary voltage to induce a π phase shift (V_π). Energy consumption is also an important performance indicator and reports the mean energy that is lost per bit; it is theoretically estimated rather than measured, and in many cases, the predictions can be inaccurate when over-simplified models are employed, as it will be discussed. Energy consumption relates to the voltage of the modulating signal, among other parameters, and both consumption and the necessary voltage level should be kept as low as possible. Chirp relates to instantaneous frequency changes that are additionally imprinted on the optical carrier; along with the dispersive effects taking place in fiber transmission, they dictate pulse broadening. Ideally, a modulator should introduce zero chirp, though in specific cases, predefined chirp levels can also be available. Finally, the footprint is the physical area occupied by the modulator and should be kept minimal to align with the constantly increasing demands of size shrinkage and higher integration densities in PICs.

In the literature, authors alternatively choose to compare modulators on the basis of various figures of merit that combine more than one of the metrics introduced above and thus consider inherent trade-offs in performance. Very popular are the figures of merit combining modulation efficiency together with losses ($V_\pi\, L\, a_{\mathrm{dB}}$) as well as bandwidth together with energy consumption or voltage. Bandwidth itself is very often reported in terms of the maximum achievable line rate (bit rate), especially in the case of experimentally evaluated modulators. However, it should be noted that it is the EO bandwidth that is the inherent modulator characteristic, unambiguously determining its frequency response. The achievable line rate is additionally determined by the modulation format and coding employed, the digital signal processing (DSP) techniques used on the transmitter and receiver side, and error correction algorithms. All of the above enable an increase in the line rate, especially when the available bandwidth is limited. The mainstream choice from the earliest generations of lightwave systems has been intensity modulation (on–off keying) with direct detection (IM/DD), and it is still dominating access networks. On the other hand, advanced modulation formats with improved spectral efficiency and transmission capacity are used in both IM/DD systems [pulse-amplitude modulation (PAM)/amplitude-shift keying (ASK) modulation] and optical digital coherent systems[17–19] that dominate core/metro networks (long-haul), with quadrature phase-shift keying (QPSK) and quadrature amplitude modulation (QAM) modulations being very popular and extensively deployed in the latter case. The coherent and conventional IM/DD systems can be identified as the two main system types, but also, other alternatives have been proposed especially for short-reach links; they utilize different modulation formats such as the discrete multi-tone (DMT), carrier-less amplitude and phase (CAP), and half-cycle subcarrier modulation (SCM).[20–24] The above formats are often employed for directly modulated lasers of limited bandwidth and are important to the family of advanced direct detection schemes. Advanced DD schemes offer a compromise between coherent and IM/DD systems, constituting a trade-off between system performance and complexity. The end performance depends on the modulation format employed, as highlighted above. However, a detailed discussion of modulation formats and their impact on the achievable bit rate is well beyond the content of this Perspective, which focuses on the physics, materials, and components for EO modulation. For this reason, special effort is made to review the different modulator types based on their inherent EO bandwidth instead of solely relying on the achieved line-rate values.

This paper is organized as follows: Sec. II briefly reviews the most important physical phenomena leading to amplitude and phase EO modulation, including the Pockels effect, the Franz–Keldysh and quantum-confined Stark effects, free-carrier effects (plasma dispersion), and phase-change effects. Section III provides a comprehensive review of recent advances in EO modulation with reference to the material system exploited, covering lithium niobate, III–V semiconductors, silicon, EO polymers, transparent conducting oxides, two-dimensional materials, and phase-change materials. This way of presentation highlights the important traits of different EO materials, which can be accommodated in diverse underlying platforms. Section IV comparatively assesses the various modulator types reviewed and discusses overlooked or misinterpreted topics important to the design and analysis of EO modulators. In Sec. V, direct modulation systems are briefly discussed as an alternative to external modulation for short-range applications. Finally, Sec. VI provides a future outlook for all the considered modulator types, and Sec. VII closes the Perspective with concluding remarks.

II. PHYSICAL PHENOMENA FOR AMPLITUDE AND PHASE ELECTRO-OPTIC MODULATION

Figure 1 summarizes the different instances of contemporary photonic modulators examined in this work. A broad range of

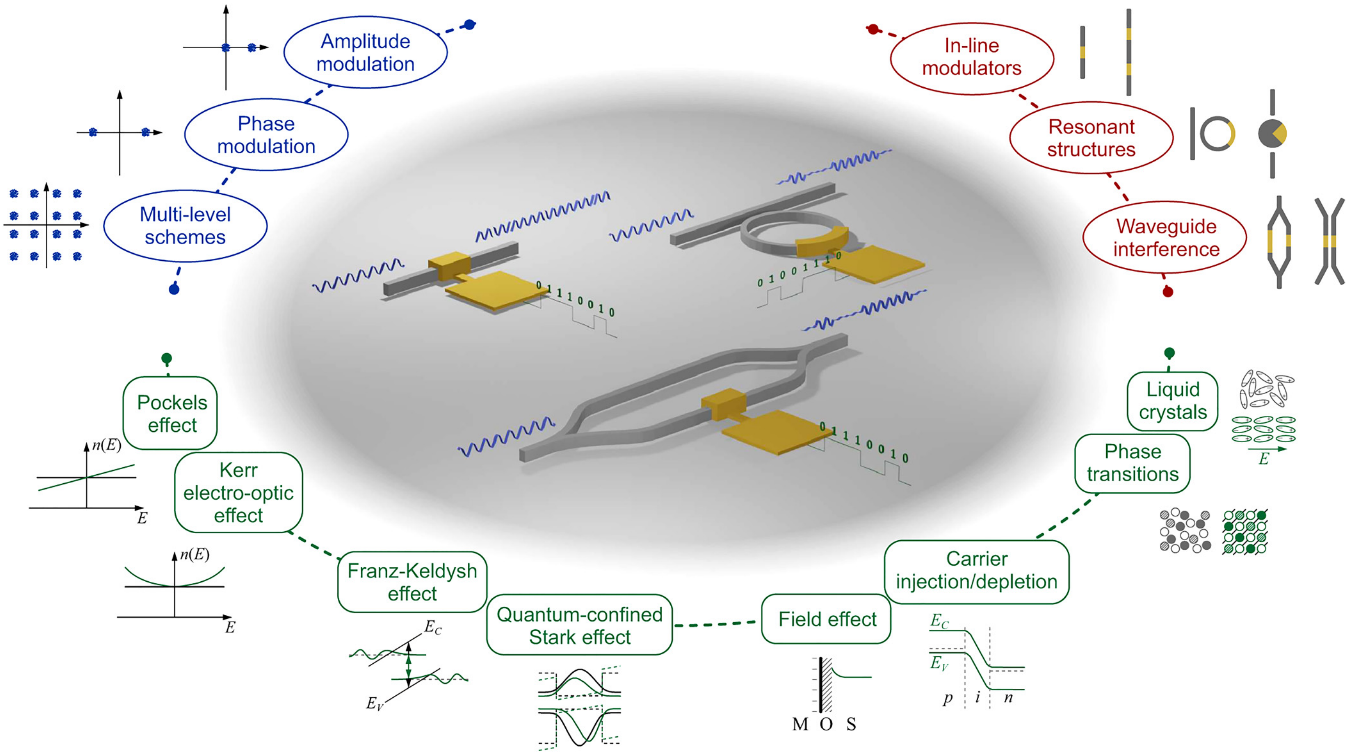

FIG. 1. Components and physical phenomena for amplitude and phase electro-optic modulation. Schematic illustration of an in-line modulator performing phase modulation and a ring resonator and a Mach–Zehnder interferometer performing amplitude modulation.

physical phenomena have been exploited, suited to either amplitude or phase modulation. The basic configurations can be classified into three main categories: in-line modulators, resonant structures, and devices based on waveguide mode interference. In this section, the most prominent physical phenomena are briefly described.

A. Pockels and Kerr electro-optic effects

The term EO effect broadly describes refractive-index changes that are induced by the application of an external electric field that can be static or of low frequency compared to the optical frequency (quasi-static). In the linear EO effect or the Pockels effect, the change in the elements of the impermeability tensor $\tilde{\eta} = \tilde{\varepsilon}_r^{-1}$ (equivalently, the difference between the coefficients of the distorted index ellipsoid and the undistorted one) is a linear function of the externally applied electric field.[25,26] This translates to index changes that are linearly proportional to the applied field. The Pockels effect is nonzero only in non-centrosymmetric crystalline materials and vanishes in amorphous ones. Well-studied EO materials include the crystals potassium dihydrogen phosphate (KH_2PO_4 or KDP), ammonium dihydrogen phosphate ($NH_4H_2PO_4$ or ADP), lithium niobate ($LiNbO_3$), lithium tantalate ($LiTaO_3$), and barium titanate ($BaTiO_3$) as well as semiconductors such as gallium arsenide (GaAs), cadmium tellurite (CdTe), and zinc tellurite (ZnTe). Lithium niobate is a uniaxial crystal of particular importance to integrated photonics due to its very wide use and will be reviewed in Sec. III A.

The EO response in the Pockels effect is described by a set of coefficients that define the third-rank linear EO tensor r_{ijk} (27 elements); given the symmetry properties of the second-rank optical permittivity and impermeability tensors, the maximum number of independent elements in r_{ijk} is reduced to 18. These elements are arranged in a 6×3 matrix using a standard index reduction; some will further end up being zero considering the existing crystal symmetry properties. The independent EO coefficients in $LiNbO_3$ are 4: r_{33}, r_{13}, r_{22}, and r_{51}.[27] When the external electric field is aligned along the optical (crystal) axis of a C_{3v} crystal such as $LiNbO_3$ or $LiTaO_3$, the crystal remains uniaxial and the principal axes are preserved. The most efficient configuration for phase modulation is that of a transverse modulator, with the light wave (optical mode) propagating along the x axis, dominantly polarized along the optical axis z (extraordinary wave), and the external electric field that induces the index changes through r_{33} being also parallel to the z axis.[26]

The Kerr EO effect shares similarities with the Pockels effect, but the changes in the impermeability tensor are now proportional to the second order of the applied electric field. This translates to index changes that are proportional to the square of the applied field.[25] The Kerr EO effect is found in crystalline as well as amorphous materials, and typical examples include the KDP and ADP crystals, as well as certain liquids.

B. Franz–Keldysh and quantum-confined Stark effect

The application of an electric field to atoms and molecules shifts their energy states by changing the energy of their electrons (Stark effect). In bulk semiconductors or insulators, the field effect results in a tilt of their energy band edges, which is referred to as the Franz–Keldysh effect.[28] The electron (hole) wavefunctions near the conduction (valence) band edge do not correspond to plane waves anymore but are described by Airy functions. As a result, they expand into the bandgap in an exponentially decreasing manner, occupying previously forbidden states. The latter is translated into an effective decrease of the bandgap value, rendering the material absorptive to previously transparent wavelengths (see the inset of Fig. 1). The effect can be equivalently described as a photon-assisted tunneling process.

In contrast to the Franz–Keldysh effect, which is independent of the crystal size, the quantum-confined Stark effect (QCSE) manifests in quantum-confined carriers.[29] Electrons and holes can be confined in three-, two-, and one-dimensional potential wells in nanoscale structures such as quantum dots, wires, and wells, respectively. Such structures impede electrons and holes from tunneling out and ensure a strong electron–hole interaction. The latter ensures the formation of stable excitonic states at room temperature. Shifting these quantum-confined states through the application of an electric field (Stark effect) results in the QCSE (Fig. 1, inset). Multiple quantum well (MQW) structures are the most popular, realized by thin semiconductor layers sandwiched between sufficiently thick barrier layers of wider-bandgap semiconductor materials. The thicknesses of the wells and barriers are in the order of a few nanometers. The applied field should be perpendicularly polarized to the quantum wells, pulling electrons and holes toward opposite sides of the layer, thus reducing the energy of the electron–hole pair and red-shifting the excitonic resonance. The applied field can well exceed the value of the ionization field, resulting in large shifts, without significant broadening of the exciton peaks. In bulk crystals, the lack of quantum confinement results in a poor shift and severe broadening of the excitonic resonances for applied fields that exceed only a few times the ionization field.

Both effects are more pronounced in direct-bandgap semiconductors due to the steep change in absorption. Their manifestation is stronger for photon energies near the bandgap value. For telecom applications, III–V semiconductors have been extensively employed due to their direct and suitably wide bandgap. The most studied representatives include the InP and GaAs systems as well as MQW structures utilizing, for example, the InGaAsP–InP platform. Germanium (Ge), a group-IV semiconductor, has also attracted attention for NIR modulators due to its 0.8-eV direct bandgap as well as its compatibility with silicon. Despite being an indirect semiconductor (∼0.66 eV), a strong electro-absorption effect has been demonstrated either through the Franz–Keldysh effect in Ge and $Si_{1-x}Ge_x$ alloys or the QCSE in Ge/SiGe quantum-well structures. Together with changes in absorption, both effects also give rise to changes in the refractive index (electro-refraction effect), as dictated by the Kramers–Kronig relations,[30] which can be exploited for realizing phase-shifting elements. The required electric field is usually applied through reverse-biased p–i–n junctions, allowing for high bandwidth and low energy consumption.

C. Free-carrier effect (plasma dispersion effect)

The free-carrier effect, also widely referred to as the plasma dispersion effect, refers to the dependence of the optical properties (both optical refraction and absorption) on the concentration of free carriers;[31] this effect nominally appears in semiconductors[32–34] and semimetals.[35] Changes in the concentration of free carriers affects the optical absorption of the material, but it inevitably alters its dielectric properties as well, as dictated by the fundamental Kramers–Kronig relations. Hence, both amplitude and phase control of the guided wave are possible, offering opportunities for different modulation realizations. Initially, the practical development of functional integrated photonic devices working with the free-carrier effect was conceptually straightforward due to the broad use of silicon and III–V semiconductors in electronics. Schemes such as p–n and p–i–n junctions or metal–oxide–semiconductor (MOS) capacitors, already studied and well-understood, were widely used to introduce carrier depletion or accumulation regions. In recent years, alternative semiconductors and semimetals have also appeared (transparent conducting oxides and two-dimensional materials), nominally governed by the same operation principle but exhibiting enhanced optical properties.

The simplest configuration to achieve carrier depletion is a reverse-biased p–n junction, where a space-charge region is formed due to a free-carrier (electrons and holes) sweep-out, reducing the optical absorption and modifying the refractive index. On the contrary, in a forward-biased p–n junction, carriers are injected via the induced current flow. Low doping is preferred in carrier-depletion configurations to reduce optical losses, while for carrier injection schemes, p–i–n junctions are favored for the same reason (lower optical losses in the intrinsic semiconductor region).[31] Carrier-accumulation configurations employ a MOS-like structure, where a thin dielectric layer is sandwiched between semiconductors and/or (semi)metals. By applying an external voltage, opposite-charge carriers accumulate on each side of the capacitor. Typical dielectrics such as silicon dioxide are commonly used, while high-κ dielectrics can further intensify the effect. Unlike p–n/p–i–n junctions, which are typical for conventional semiconductor configurations, MOS-like capacitors are preferred in contemporary configurations, involving transparent conducting oxides or low-dimensional materials.[36,37]

D. Phase-change effect

Phase-change materials (PCMs) can experience a phase transition in response to external stimuli (temperature, electric field, optical illumination). They are broadly classified into two main categories: (i) transition metal oxides that undergo a reversible crystalline-to-crystalline (electronic) transition and are suited to volatile applications such as amplitude/phase modulation and routing and (ii) chalcogen-based alloys that undergo an amorphous-to-crystalline (structural) transition and are primarily exploited for non-volatile applications such as memory operation.[38] Prominent materials for the two categories, respectively, are vanadium dioxide (VO_2), which exhibits the phase change close to room temperature, and the ternary germanium–antimony–tellurium (GST) compound $Ge_2Sb_2Te_5$. In both cases, the phase transition can be driven electrically and is associated with a metal to insulator transition, leading to a pronounced change in the infrared optical properties (refractive index, n, and extinction coefficient, κ).

III. CONTEMPORARY PHOTONIC ELECTRO-OPTIC MODULATORS

In this section, we review the advances in contemporary photonic electro-optic modulators, categorized based on the EO material they exploit.

A. Lithium niobate

The lithium-niobate (LN) modulator is one of the most successful and indispensable components in optoelectronics. For decades, lithium niobate has been the material of choice, featuring a very strong Pockels effect (the strongest element in the EO coefficient tensor of bulk $LiNbO_3$ being $r_{33} \sim 31\,\mathrm{pm/V}$),[27] a broadband spectral response with a refractive-index change at the femtosecond timescale, a wide transparency window (0.4–5.5 μm), linearity, good temperature stability with a low thermo-optic coefficient (TOC) of $10^{-5}\,\mathrm{K}^{-1}$, excellent chemical and mechanical stability as well as long-term reliability.

In-diffusion of titanium into bulk LN wafers and annealed proton exchange are the commonly employed methods for defining conventional LN stripe waveguides,[39] mostly in Mach–Zehnder modulator (MZM) configurations. Such waveguides are characterized by low index contrast (~0.02 or less), translating into weak optical confinement in both horizontal and vertical directions and, thus, limited possibility for high density integration. Typical phase shifter lengths are in the cm range (>5 cm) and V_π is 3–6 V; thus, $V_\pi L$ normally exceeds 10 V cm. Due to the poor mode confinement, metal electrodes should be spaced far away from the optical waveguide (approximately 10 μm) to keep losses at a reasonable level. This means that it is typically necessary to use an electrical amplifier to drive a conventional LN-MZM, which is itself energy consuming. The high driving voltages translate into high energy consumption.

Conventional LN modulators have been for years the standard choice for long-haul telecom systems, but they cannot meet the growing demands of short-range datacom systems, being too bulky, costly, and inefficient. Therefore, there is a steadily growing interest for high-performance, miniaturized LN modulators for datacom and data center applications, wireless communications, and quantum applications. Most commercial LN products nowadays still outperform Si-based modulators and offer a 3-dB BW up to 35 GHz, half-wave voltage V_π down to 3.5 V, and possibility for zero to negative chirp.

Evolution of the LN modulator was made possible with the fabrication of single-crystal LN thin films and LN wafers. The crystal ion slice (CIS) method was introduced in Ref. 40, where an LN substrate is ion-implanted and subsequently etched in hydrofluoric acid; initially, separated slices were around 9 μm thick. Rapid progress in CIS and wafer bonding led to sub-micron LN films,[41] where an ion-implanted substrate is thermally treated, leading to a thin layer of lithium niobate being split off and subsequently transferred to another substrate. Transferred layers and bulk lithium-niobate are of comparable quality and properties. Lithium-niobate-on-insulator (LNOI) platforms offer high-index contrast in the range of ~0.7, and bending radii below 20 μm are now possible. LN thin films can be processed in 3–6″ wafers, which is satisfactory though still falling behind the 8–12″ wafers in silicon photonics, with all three crystal cuts (x-, y-, z-cut) possible and commercially available. In x-cut LN modulators, operation is on the quasi-TE mode with the horizontal electric field sensing the large EO coefficient r_{33}, whereas z-cut modulators are intended for quasi-TM mode operation. LN thin-film devices are in the millimeter length scale (<20 mm) and thus can fit in common transceiver packages such as the Quad Small-Factor Pluggable (QSFP). Even more intriguing is the possibility to operate with voltages ~1 V that allow driverless modulation from direct CMOS output.

Contemporary LN devices are broadly classified into two categories: those exploiting a uniform (un-etched) LN thin film and those with patterned (etched) LN films. The first category comprises a broad range of heterogeneously integrated devices or hybrid platforms.[42,43] Uniform LN thin films can be oxide-bonded on prefabricated silicon waveguides at room temperatures, and importantly, the fabrication process is CMOS-compatible,[44–46] with LN integration performed at the back-end respecting the structure already formed. The underlying silicon-photonic circuitry provides the required passive functionality and ensures efficient standardized in/out chip coupling. In Ref. 44, an un-etched LN film having a thickness of 600 nm is bonded on the top of a planarized silicon-on-insulator (SOI) photonic circuit accommodating a Mach–Zehnder interferometer (MZI), with aluminum electrodes defined over the LN film (Fig. 2); a device 5 mm long demonstrated

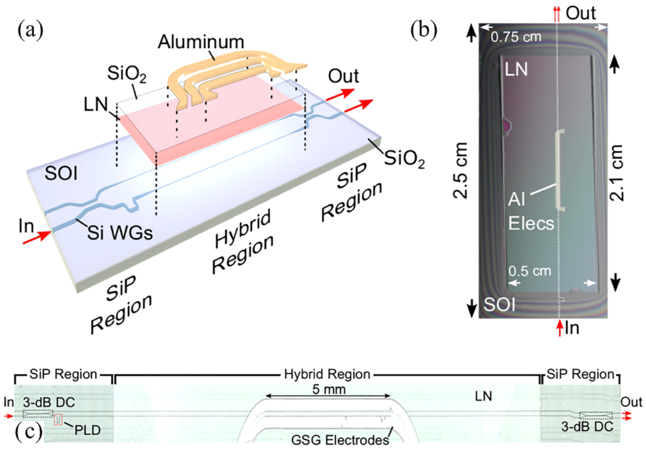

FIG. 2. Hybrid Si–LN EO Mach–Zehnder modulator.[44] (a) General view showing the un-etched (uniform) LN thin film bonded on the top of an MZI written in Si and the aluminum electrodes. The "SiP Regions" accommodate the Si passive circuitry outside the bonded LN film area. (b) SEM image of the hybrid Si–LN modulator. (c) Composite microscope image (not to scale). DC, directional coupler; PLD, path-length difference; GSG, ground-signal-ground; and SiP, Si photonics. Adapted with permission from Weigel *et al.*, Opt. Express **26**, 23728 (2018). Copyright 2018 The Optical Society.

a $V_\pi L$ equal to 6.7 V cm and an ER above 20 dB. More importantly, the measured EO response confirmed a bandwidth exceeding 106 GHz. Devices with two layers of silicon waveguides that are vertically coupled using adiabatic tapers result in lower losses and higher optical overlap with the LN thin film.[46] Other hybrid platforms choose an easy-to-etch material as the device layer (loading), which is bonded on the top of an un-etched LN thin film. Rib waveguides are defined, and loading materials include tantalum pentoxide,[47] chalcogenide glass,[48] and silicon nitride.[49–51] This approach appears promising, though various limitations exist including the incompatibility of some of the materials used (tantalum pentoxide, chalcogenides) with CMOS processing. Hybrid Si–LN waveguides may suffer from reduced light confinement in the LN core and detrimental nonlinearities originating from Si. Silicon nitride (SiN) is deemed a more appealing alternative to Si due to the absence of two-photon absorption (TPA), lower material loss, and a broader transparency window; in addition, SiN has a lower refractive index compared to Si, thus allowing for more light to be confined in the LN film.[50]

The second category of devices includes those with etched single-crystal sub-micron lithium-niobate films.[52–58] Lithium-niobate is considered a material hard to etch and in principle produces rough surfaces that suffer from high scattering losses, in the order of 3 dB/cm or higher.[55,56] The possibility of ultra-low losses in dry-etched subwavelength LN waveguides was demonstrated in Ref. 52 with a value as low as ∼0.027 dB/cm. In Ref. 54, an LN thin film of 600 nm thickness has been etched to define an MZI [Fig. 3(a)], and for a 20-mm-long device, the half-wave voltage V_π is 1.4 V with 30 dB of ER [Fig. 3(b)]; such a modulator allows direct driving by a CMOS circuit. The EO response for a 5-mm device reaches 100 GHz [Fig. 3(c)], and the modulators in Ref. 54 were also evaluated in various ultrahigh data rates including 100 Gbps on–off keying (OOK) and multi-level formats (70 GBd 4-ASK, 70 GBd 8-ASK). Other modulator configurations are also possible, such as those exploiting a ring or racetrack resonator.[55] Lithium-niobate waveguides of rib type were etched on an LN thin film of 600 nm to form the rings/racetracks, and electrode pairs were defined for applying the modulation signal [Figs. 3(d)–3(f)]. EO tuning efficiencies were around 7pm/V, and the 3-dB EO bandwidth was found to be 30 GHz for racetracks, limited by the cavity-photon lifetime; successful high-speed data operation was confirmed up to 40 Gbps. For a detailed theoretical analysis of the EO limitations in the performance of LN microring resonators, see Ref. 59.

Recently, there have also been experimental demonstrations of devices bridging the two categories discussed in the preceding paragraphs,[60,61] as they combine a silicon-photonic layer together with an etched LN thin film: this approach, though classified as hybrid Si–LN, is differentiated over previous hybrid ones with the LN thin film now being etched and vertical adiabatic couplers allowing for full light transfer between the underlying Si layer and the LN waveguides. In Ref. 61, the LN layer is a 600 nm thin film, where rib waveguides are dry-etched on the top of a SOI circuit [Figs. 4(a)–4(c)]. LN waveguides function as the phase modulators, and the bottom SOI circuit implements the grating couplers for in/out chip coupling and the 3-dB multi-mode interference (MMI) couplers that form the MZI (not shown); vertical adiabatic couplers in the form of inverted silicon tapers provide the light coupling up and down between the two guiding layers [Figs. 4(d) and 4(e)]. 3-dB EO BW exceeds 70 GHz for 3 and 5-mm-long devices, with the former ones tested in data transmission experiments at 100 Gbps OOK and 56 GBd 4-PAM (112 Gbps) signals.

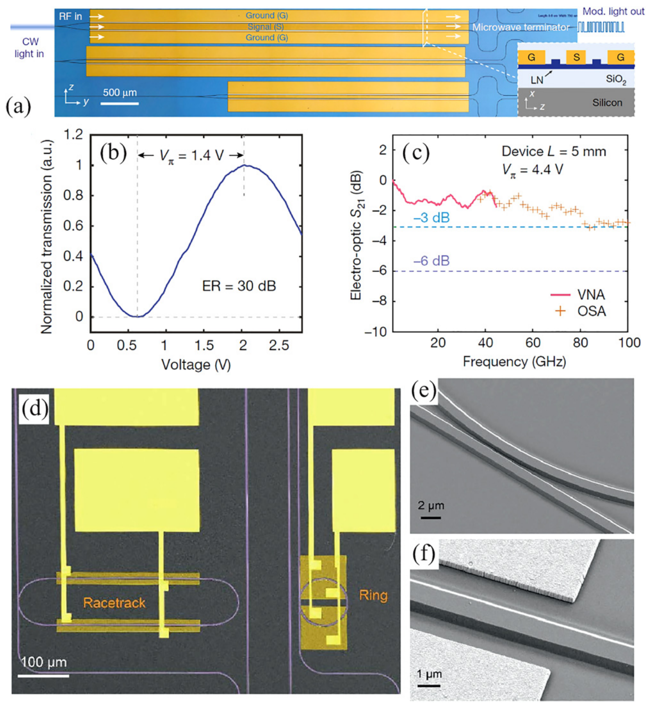

FIG. 3. Electro-optic devices based on etched single-crystal sub-micron LN thin films. (a)–(c) Monolithically integrated LN modulators in an MZI configuration.[54] Microscope image showing three MZIs with a cross-section schematic (inset). Normalized optical transmission for a 20-mm device vs applied voltage showing a V_π equal to 1.4 V and an ER of 30 dB. The EO response for a 5-mm device shows a 3-dB bandwidth of 100 GHz. Adapted with permission from Wang *et al.*, Nature **562**, 101 (2018). Copyright 2018 Springer Nature. (d)–(f) EO racetrack and ring LN modulators.[55] SEM image of a racetrack and ring modulator, showing also bottom and top electrodes together with the contact pads. Close-up image of the coupling region in the racetrack resonator and close-up view of the metal electrodes with the LN rib waveguide. Adapted with permission from Wang *et al.*, Opt. Express **26**, 1547 (2018). Copyright 2018 The Optical Society.

As already discussed, experimental demonstrations of devices with an EO bandwidth around 100 GHz have appeared in recent years.[44,45,54,61] However, there are strong indications that substantially higher bandwidths are feasible[62] that can exceed 500 GHz as estimated in Ref. 53. Support of data rates even above 1 Tbps is possible with advanced modulation formats (64-QAM at 200 GBd).[54] Although most LN modulators follow the Mach–Zehnder layout, other alternatives such as the Michelson interferometer[60,63] have been assessed in the hybrid Si–LN platform.[61] A Michelson interferometer outperforms the corresponding MZI in terms of $V_\pi L$ by a factor of two, but it presents appreciably lower BW, which is mainly attributed to the velocity mismatch between the RF signal and the counter-propagating optical wave reflected

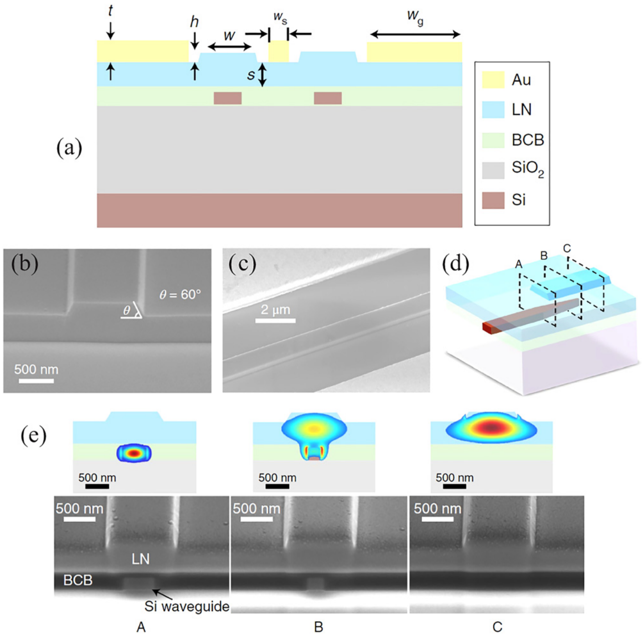

FIG. 4. Hybrid Si–LN EO Mach–Zehnder modulator with an etched LN thin film.[61] (a) Schematic of the device cross section. (b) SEM image of the LN waveguide and (c) SEM image of the metal electrodes and the optical guide. (d) Schematic of the vertical adiabatic coupler that provides light transfer between the silicon layer and the LN waveguides. (e) Calculated mode distributions and SEM images at different positions along the vertical adiabatic couplers. Adapted with permission from He *et al.*, Nat. Photonics **13**, 359 (2019). Copyright 2019 Springer Nature.

from the MMI-based Sagnac loop mirror. Plasmonic EO modulators based on LN substrates are also possible. In a very recent publication,[64] a plasmonic directional coupler was made by two metal stripes on an un-etched LN substrate, serving both as plasmonic waveguides and signal electrodes. The device length was around 15 μm and resulted in a record-low $V_\pi L$ value of 0.21 V cm, with a theoretically estimated modulation BW in excess of 800 GHz.

The performance of LN modulators is strongly tied to the RF circuitry delivering the modulation signal. Reduced overlap between electrical and optical modes and inefficient microwave signal delivery are identified as the main limiting factors in performance. In the case of LN modulators, traveling-wave electrodes (TWEs) are the default choice, typically in the form of a coplanar waveguide (CPW)[49,53,54,65,66] in a ground-signal-ground (GSG) configuration. Electrodes are commonly gold electroplated, but also, thin deposited aluminum electrodes are used in CMOS-compatible devices. Three main prerequisites should be met for the RF circuitry:[62,67] (i) minimum mismatch between the optical mode group velocity and the RF wave, (ii) the characteristic impedance of the transmission line should match the source and load impedance (typically 50 Ω), and (iii) RF losses should also be as low as possible. To better appreciate the various restrictions related to the RF circuitry that delivers the modulation signal, we quote the low-frequency relative permittivities of LN, $\varepsilon_{xx}^T = \varepsilon_{yy}^T = 84.5$, $\varepsilon_{zz}^T = 27.8$ (free or unclamped) and $\varepsilon_{xx}^S = \varepsilon_{yy}^S = 45.5$, $\varepsilon_{zz}^S = 26.2$ (rigid or clamped).[68] Thus, the dielectric permittivity of LN at RF frequencies is much higher than the value presented at optical frequencies ($\varepsilon_{\text{opt}} \sim 4.6$-5). This usually necessitates to additionally incorporate a material with lower dielectric permittivity that will accommodate part of the RF mode and will consequently increase the RF velocity. Successful strategies to this end include tall electrodes to pull the RF electric field in air,[65] placing an SiO_2 buffer layer between the electrodes and LN,[65] extra mechanical LN thinning,[69] tuning the thickness of the oxide layer (SiO_2) underneath the LN device layer,[54] and silicon layer thinning.[45] In the case of LN thin-film modulators where $n_{\text{eff,RF}}$ is lower compared to the $n_{\text{eff,opt}}$, a higher index cladding material such as UV15 can be used[53] to increase $n_{\text{eff,RF}}$. Though V_π can be traded-off with the device length, longer devices present lower bandwidths as the mismatch between the optical and microwave velocities is intensified, apart from the obviously higher losses.

For devices with EO bandwidth approaching or exceeding 100 GHz,[44,45,53,54,61,69] length is restricted to values below 5 mm, leading to increased driving voltages. For such high bandwidth, the RF line of choice is still the CPW with metal thickness in the range of 1–2 μm. RF losses include the contribution of the conductor and substrate as well as radiation and reported experimental values are around 7–8 dB/cm at 100 GHz,[44,45,61] aligned with theoretical predictions. CPW radiation losses are expected to dominate above 200 GHz. Maintaining the characteristic impedance close to 50 Ω in such an extended frequency range has been proven possible, with a variation of a few percent around the nominal value. Despite the technical challenges and the high material dispersion of LN, neither RF losses nor velocity matching turn out as fundamental limitations for accessing bandwidths above 100 GHz.

B. III–V semiconductors

The family of III–V semiconductors includes compounds between group-III (Al, Ga, In) and group-V (N, P, As, Sb) elements of the periodic table. The most important representatives are the binary compounds GaAs, InP, GaP, and GaN as well as the ternary InGaAs, InGaP and the quaternary InGaAsP, InGaAlP semiconductors. The EO effect in III–V semiconductors is the resultant of multiple optical processes, including the linear EO effect, the Franz–Keldysh effect in bulk semiconductors or the QCSE in quantum-confined structures, as well as free-carrier effects. All effects contribute to changes in both real and imaginary parts of the optical permittivity, but they can often have a predominant electro-refractive or electro-absorptive nature by engineering the material and system parameters.

The linear EO property stems from the non-centrosymmetric crystal structure of III–V semiconductors, which renders the crystal polarizable, giving rise to a field-induced birefringence in addition to a piezoelectric effect. The change in the refractive index depends in sign and magnitude on the crystal orientation, the RF field, and the light polarization. For the standard (100) cut and an RF field parallel to the surface vector, the linear EO effect becomes maximum for light polarization parallel to [011], modulating only the TE-polarized light. The change in the refractive index is given by $|\Delta n| = (1/2)\, n_0^3\, r_{41}\, E$, where n_0 is the ordinary refractive index, r_{41} the EO tensor component, and E the RF field. For GaAs, it is $r_{41} \sim 1.6\,\mathrm{pm/V}$,[28,70] which is considerably weaker compared to the EO coefficient in $LiNbO_3$ (Sec. III A). Nevertheless, the higher refractive index of III–V semiconductors (∼3) can partially compensate for the weaker EO coefficient, while their lower dielectric constant (∼12) also allows for easier phase-matching in traveling-wave designs. Early studies have already shown that GaAs modulators can be highly competitive to conventional LN designs.[71]

The Franz–Keldysh effect manifests in bulk III–V semiconductors as changes in the absorption of near band-edge wavelengths under the application of an electric field due to the broadening and red-shifting of the absorption edge. The induced refractive-index change scales with the square of the applied field and thus constitutes a quadratic EO effect. For near band-edge wavelengths, the effect is strong and surpasses the linear EO effect, diminishing for longer wavelengths. Operation at the desired wavelength is limited by the maximum allowed field value and the absorption at the unbiased ("transparent") state, which is in fact non-zero even for photon energies below the bandgap, despite the absence of an external electric field, due to the exponential decay of the absorption coefficient (Urbach tail) for wavelengths below the band edge. The latter is caused by deviations from the model of an ideal crystal lattice due to, e.g., defects. Bandgap engineering is frequently employed for tuning operation at the desired wavelength. The effect can be enhanced through the QCSE in quantum-confined structures.

Free-carrier effects in doped III–V semiconductors can also contribute to the modulation effect. An accumulation of free carriers increases the effective bandgap when the conduction and/or valence bands are partially filled (bandfilling effect), blueshifting the absorption edge. Such changes impact both the real and imaginary part of the complex refractive index.[30] The influence of electrons is particularly strong due to their smaller effective mass, while holes exhibit a much weaker EO effect, with a larger contribution to the optical loss. Suitably designing the waveguide doping profile can enhance the impact of free-carrier effects on the total index change.

Under specific conditions, all effects can contribute constructively to the aggregate EO effect. Specifically, the linear EO effect results in a positive change to the refractive index when the waveguide axis is perpendicular to the (011) facet. A positive change is also evidenced due to the quadratic EO effect, independently of the mode polarization or crystal orientation. An additional index rise can be induced in the case of carrier depletion.

Simple rib or ridge waveguides as well as buried-heterostructure formations with a width between 1.5 and $2\,\mu$m are employed for the III–V-based modulators. The RF field is usually applied through a p–i–n junction, and the optical mode is guided in the high-index intrinsic semiconductor region. The dopant concentrations in the p–i–n diode are a trade-off between optical and RF losses. A strong optical confinement (large guiding layer) allows for a greater overlap with the RF electric field, lower waveguide capacitance per unit length, and reduced RF losses. The optimal design should provide a balance between high EO overlap and high RF-field intensity, while avoiding a detrimental increase in the capacitance.

The predominant representative is the electro-absorption modulator (EAM), typically employing the QCSE in quantum-confined structures to modulate the light intensity at near band-edge wavelengths. The most popular choice is the MQW structure (Fig. 5), which exhibits superior modulation properties compared to quantum dots but also higher chirp values. A compromise is sought by alternative structures such as quantum dashes.[73] EAMs are simple in-line structures, usually integrated with distributed-feedback lasers (DFBs), butt-coupled on the same chip, to form electro-absorption modulated lasers (EMLs). EAMs have demonstrated bandwidth values exceeding 40 GHz for driving voltages as low as a few volts and modulation lengths in the order of a hundred of microns.[74–76] The short modulation length results in lumped-electrode modulators with an RC-limited bandwidth. The latter is in a competing relation with ER, which rises for longer devices at the expense of higher capacitance and increased ILs. A compromise is usually achieved by enhancing the modulation effect through, e.g., increasing the quantum confinement or the number of quantum wells. The latter also decreases the p–i–n capacitance and lowers the necessary bias for achieving the targeted ER but still with a penalty on IL. Note that maintaining low ILs is important for the efficiency of the modulator and for ensuring high values of the optical modulation amplitude (OMA) to facilitate detection at the receiver. In Ref. 77, the modulation effect (Franz–Keldysh effect) is enhanced by embedding the InGaAsP waveguide in an InP photonic-crystal platform. In this approach, EAMs as long as 100 μm are demonstrated with modulation rates up to 56 Gbps (NRZ-OOK) and driving voltages below 1 V. The employed air-bridge structure provides a capacitance reduction, and the energy consumption is calculated below 2 fJ/bit. Lumped-electrode EAMs have demonstrated bit rates exceeding 100 Gbps using 4-PAM modulation formats.[78,79] A bit rate up to 200 Gbps (4-PAM) is demonstrated in Ref. 80, where a flip-chip interconnection technique between the RF circuit and the modulator allows for a higher EO bandwidth (>59 GHz). A 300 Gbps rate has also been achieved using the DMT modulation format and a digital-preprocessed analog-multiplexed digital-to-analog converter, with the bandwidth of the employed EMLs exceeding 55 GHz.[81]

The length of EAMs can be a limiting factor when driven by a 50-Ω system because it is translated into low impedance values. Despite the suitability of the latter for high speeds, it poses limitations at lower frequencies due to increased RF reflection. Toward achieving a better impedance match throughout the bandwidth, traveling-wave electro-absorption modulators (TWEAMs) were suggested. Through the use of segmented structures, they manage to present a higher input impedance and thus effectively suppress reflections. In Ref. 82, a 100-GHz TWEAM has been reported, with a total length of $180\,\mu$m. The performance of the complete DFB-TWEAM module is shown in Fig. 6.[83] At a 100-Gbps (NRZ-OOK) bit rate, a dynamic ER of 4.2 dB is reported for a 2-V swing. Subsequent works based on this modulator demonstrated rates from 100-Gbps (NRZ-OOK)[83,84] up to 200 Gbps (DMT),[85] with a potential for even higher bit rates using more complex modulation formats.

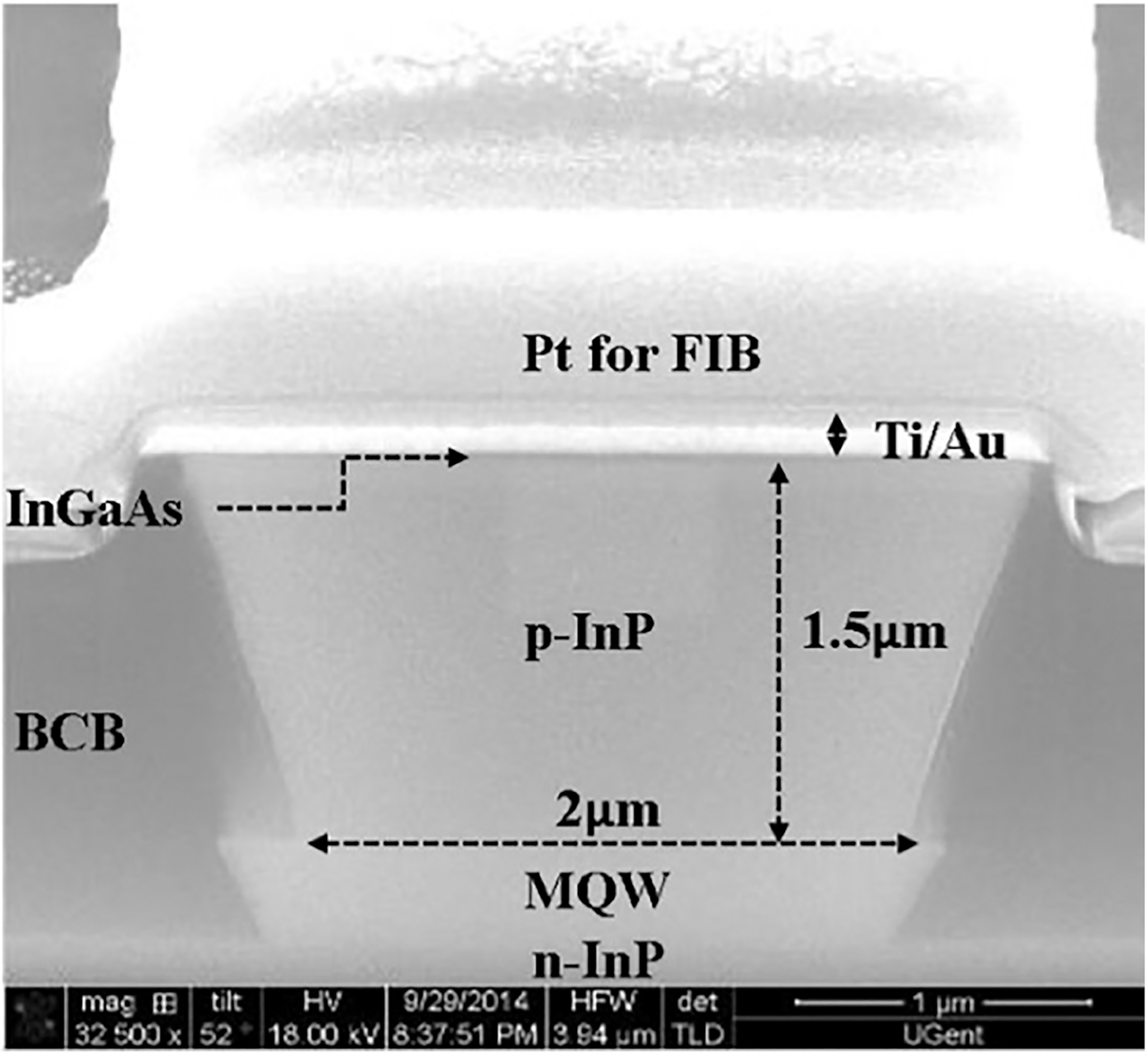

FIG. 5. SEM picture of the InP-based p–i–n junction in a MQW electro-absorption modulator.[72] Adapted with permission from Fu *et al.*, Opt. Express **23**, 18686 (2015). Copyright 2015 The Optical Society.

Mach–Zehnder modulators have also been demonstrated, requiring a compromise between index change and absorption to ensure short and low-loss phase shifters. Differentially driven, short, lumped electrodes result in compact 10-Gbps OOK MZMs, driven by voltages below 3 V and exhibiting a negative chirp.[86] Higher bit rates require traveling-wave electrodes, which are configured either as independent, coplanar microstrips for each interferometric arm or as a series push–pull configuration with a capacitance-loaded coplanar stripline electrode [Fig. 7(a)]. The latter design allows additionally for a reduction in the overlap between the RF mode and the doped regions of the p–i–n diode, reducing the RF loss, while allowing for controlling the velocity of the RF signal through changes in the distributed capacitance. Impedance matching to the typical 50 Ω value is generally challenging for InP-based MZMs due to the large capacitance per unit length introduced by the p–i–n waveguide structure. A 20-GHz TWE-MZM with a 25-dB ER has been demonstrated,[87] allowing for a bit rate exceeding 40 Gbps (DQPSK) for a 3V_{pp} driving

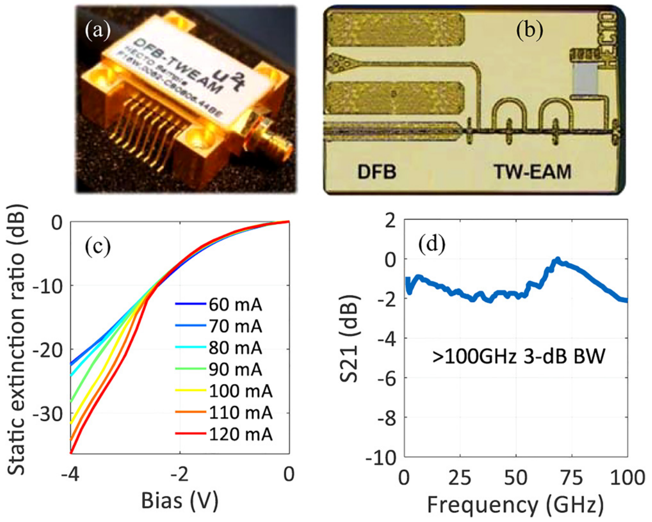

FIG. 6. Traveling-wave electro-absorption modulator.[82,83] (a) Picture of the packaged transmitter (DFB-TWEAM) module. (b) Microphotograph of the chip ($1 \times 0.5\,\text{mm}^2$). (c) Static extinction ratio as a function of the bias voltage for varying driving currents of the DFB. (d) Measurement of the 3-dB EO BW of the TWEAM. Adapted with permission from Estaran *et al.*, J. Lightwave Technol. **37**, 178 (2019). Copyright 2019 IEEE.

voltage. The more recent capacitance-loaded series push–pull TWE configuration[88] in Fig. 7 exhibits an enhanced bandwidth of 54 GHz, achieving bit rates up to 300 Gbps (8-PAM) for 0.57 pJ/bit.[89] The modulator has a static ER equal to 25 dB, IL = 6 dB, and $V_\pi L = 0.55$ V cm ($V_\pi = 2$ V). In Ref. 90, the use of high-speed SiGe driving electronics allowed for a 2-channel (TE and TM) bit rate of 1 Tbps using a 100-GBd 32-QAM InP-based TWE-MZM. The use of an n–i–p–n heterostructure in Ref. 91 instead of the conventional p–i–n diode reduces the RF losses of the InP-based, capacitance-loaded TWE-MZM at high frequencies, providing an 80-GHz EO bandwidth. A static 25-dB ER is demonstrated for $V_\pi = 1.5$ V and a 4-mm length with an on-chip 8.5-dB IL. Modulation performance up to 128 GBd (QPSK) is reported with the potential for even higher rates (333 Gbps, DMT).[92] Apart from the InP system, GaAs-based MZMs employing the GaAs/AlGaAs heterostructure have also been reported[93–95] due to their lower cost, superior electrical properties, and temperature stability. The large offset of standard telecom wavelengths from the band-edge wavelength of GaAs (∼880 nm) renders the weak Pockels effect as the primary modulation effect. Despite their broadband performance, they require mm-scale interaction lengths in order to maintain low driving voltages ($V_\pi \sim 3$ V). ER values exceeding 20 dB have been reported, with a typical fiber-to-fiber loss of ∼7–8 dB. Bandwidth values in the range of 25–30 GHz have been reported, demonstrating rates from 44.6 (DQPSK)[93] to 150 Gbps (64-QAM).[94]

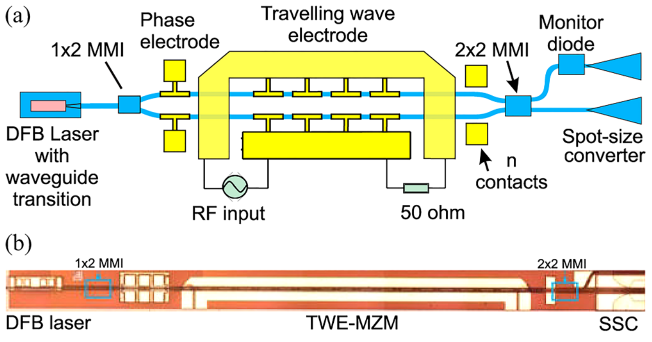

FIG. 7. (a) Schematic structure of the transmitter in Refs. 88 and 89, employing a capacitance-loaded traveling-wave-electrode MZM. (b) Photograph of the fabricated DFB-MZM module ($0.5 \times 8\,\text{mm}^2$). Adapted with permission from Lange *et al.*, J. Lightwave Technol. **34**, 401 (2016). Copyright 2016 IEEE.

The high efficiency of the III–V-based modulators as well as their opportunity to be integrated with optical gain devices (e.g., lasers, amplifiers) and high-speed electronics would be highly desirable on SOI-based platforms due to the low cost, index contrast, detection efficiency, and CMOS compatibility of the latter. To bridge the two technologies, a hybrid III–V silicon-photonic platform[96] has been introduced by bonding a III–V wafer (usually InP) on the top of a fully processed SOI wafer using molecular or divinylsiloxane–benzocyclobutene (DVS–BCB) adhesive wafer bonding. The coupling between the hybrid and silicon-photonic circuitry is achieved by tapering the III–V layer. Lumped[72,97] and TWEAM[98] as well as Mach–Zehnder modulators[99] can be formed on the III–V layer, supporting bandwidth values exceeding 67 GHz[98] and rates up to 100 Gbps (duobinary modulation).[97] Finally, III–V/Si modulators employing hybrid III–V/Si MOS capacitors have also been reported.[100–102] The large carrier-induced index change, the high electron mobility, and low plasma absorption of III–V semiconductors are beneficial for low-loss and compact phase shifters, which outperform their pure silicon counterparts (Sec. III C).

C. Silicon

Silicon is undoubtedly the most popular material in integrated nanophotonics, mostly due to its massive involvement in electronics, which gave Si an important fabrication-related head start compared to other materials considered for optical integration. As a result, SOI-based modulators are nowadays one of the most studied and well-developed component in photonics. Based on the seminal works by Soref and co-workers,[32,103] pure silicon modulators became possible by exploiting the free-carriers (plasma dispersion) effect, i.e., a small alteration in the refractive index of silicon ($\Delta n_{\text{Si}} \sim 3\%$ at most), induced by (electrically controlled) modifications in its free-carrier density. From the first experimental demonstration of an Si-based GHz modulator in 2004,[104] significant progress has been witnessed in modulator designs with high EO bandwidth (up to 50 GHz) and low energy consumption (<10 fJ/bit). Transmission rates up to several hundred Gbps have been reported by resorting to advanced modulation IQ schemes.[105–108]

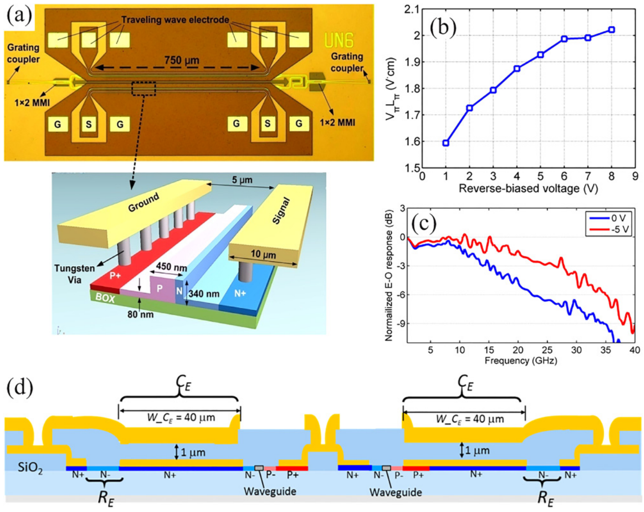

FIG. 8. Silicon MZMs. (a) Reverse-biased, horizontal p–n junction silicon modulator with its TW electrodes.[114] (b) Dependence of voltage-length product and (c) EO bandwidth on the applied reverse bias (and thus on the carrier-depletion level). Adapted with permission from Xiao *et al.*, Opt. Express **21**, 4116 (2013). Copyright 2013 The Optical Society. (d) Schematic of a forward-biased p–i–n junction MZM, showing in detail the design of the equalizing electrodes (C_E and R_E regions), which increase the EO bandwidth.[110] Adapted with permission from Baba *et al.*, Opt. Express **23**, 32950 (2015). Copyright 2015 The Optical Society.

Regarding the dynamic control of free carriers in silicon, various configurations have been explored over the years. These configurations include capacitor-like structures for carrier accumulation and appropriately biased p–n/p–i–n junctions for carrier depletion/injection. Carrier-accumulation schemes employ a thin insulator layer (typically below 10 nm) sandwiched between Si to form a capacitor (silicon–insulator–silicon capacitor, SISCAP) so that opposite charge carriers accumulate on each side of the insulator when an external bias is applied, modifying the properties of Si. Generally, highly doped silicon is preferred to lower the series resistance, but it is often the intrinsically high capacitance of SISCAPs that can be the limiting factor regarding EO bandwidth. Despite the potential limitations, high-speed operation with moderate additional (carrier-related) losses are the main characteristics of carrier-accumulation configurations, as reported in the literature.[15] Finally, SISCAPs typically involve a challenging fabrication process requiring a polysilicon layer above the oxide, which brings additional losses because it needs higher doping to increase modulation efficiency. Although recrystallizing is possible, this approach significantly deviates from standard commercialized CMOS techniques.[15]

Carrier depletion (injection) on the other hand relies on a reverse- (forward-) biased p–n or p–i–n junction to provide carrier inversion (current flow); such junctions are fabricated with standardized and CMOS-compatible processes. Carrier-depletion devices are generally characterized by high speed but also high voltage-length product; nonetheless, a number of design alternatives have been developed over the years to allow for more efficient carrier-concentration control, including horizontal, vertical, interchanged, interleaved, asymmetric, and profiled junctions.[109] On the contrary, the carrier-injection mechanism is more efficient due to the large diffusion capacitance and the carrier–light wave interaction taking place in larger areas at the expense of a speed reduction, which is mostly limited by carrier diffusion.[110]

The first GHz-scale modulator in silicon was demonstrated in an MZI SISCAP configuration.[104] Although its performance metrics are considered quite poor by today's standards (approximately 3-GHz EO bandwidth and a 8 V cm voltage-length product), it paved the way for the research that followed. Within the next year, the same group achieved a significant improvement of the phase shifter,[111] measuring $V_\pi L = 1.4\,\mathrm{V\,cm}$. However, the interest in carrier-accumulation devices quickly started to weaken despite their promising prospects. The interest shifted to the more fabrication-friendly carrier-depletion/injection configurations, with forward-biased p–i–n[110] and reverse-biased p–n/p–i–n (vertical[112] or horizontal[113–116]) junctions. In Ref. 114, a $340 \times 450\,\mathrm{nm}^2$ Si-slab waveguide (80-nm slab thickness) is used to configure 750-µm-long symmetric phase shifters, placed in both arms of an MZI [Fig. 8(a)]. A 50-nm horizontal offset of the p–n junction is introduced into the waveguide core [close-up view in Fig. 8(a)] to maximize the modulation efficiency, a standard practice that increases the overlap between the optical mode and the spatial free-carrier distribution. Applying a higher static reverse-bias to the phase shifters allows for a higher electrical bandwidth due to a reduction in the capacitance of the p–n/p–i–n junction (and thus the RC constant) as a result of the increase in its space-charge region but also results in higher voltage-length products [Figs. 8(b) and 8(c)]. Ultimately, a 28-GHz EO bandwidth is achieved with the demonstration of a 60 Gbps transmission rate (OOK) and a 3.6 dB dynamic ER; similar metrics have been reported in the literature for other reverse-biased junction configurations.[106,112,117] Alternatively, forward-biased p–i–n junctions [Fig. 8(d)] provide lower voltage-length products but require (passive) equalizing RF circuits, which mostly lower the equivalent electrical capacitance to allow for comparably high-speed operation at the expense of modulation efficiency: In Ref. 110, $V_\pi L = 0.62\,\mathrm{V\,cm}$ (60-µm-long device) is reported with a 17-GHz EO BW and a 2.1-dB dynamic ER at a 25-Gbps transmission rate (OOK).

In parallel with the development of MZI modulators, ring/disk cavities were also examined as possible candidates to significantly reduce the device footprint. This comes at the expense of optical bandwidth since cavities with high-quality factors (preferred for their increased pm/V tunability) are characterized by high cavity-photon lifetimes. The first demonstration of a silicon-ring modulator with a forward-biased p–i–n junction was reported in 2005 (shortly after the first high-speed silicon MZI demonstration) at a 1.5 Gbps transmission rate.[118] Soon, the different junction alternatives discussed above were adopted in ring cavities, leading to important improvements in the measured data rates and extinction ratios. Additionally, a significant part of the research was dedicated to the efficient thermal stabilization of the cavities, constituting nowadays the main energy-consumption mechanism. In Ref. 119, the fabricated 7.5-μm-radius ring (Fig. 9) has a horizontally shifted p–n junction in the guiding area, achieving a 14.2 pm/V resonance-frequency shift, translated

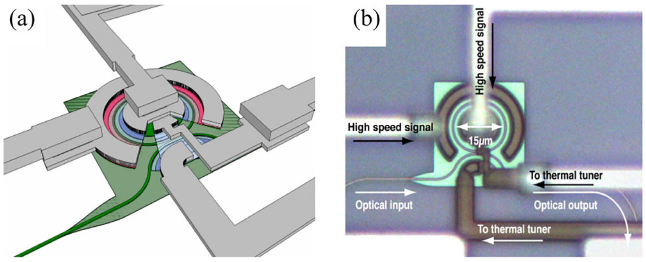

FIG. 9. (a) Schematic and (b) practical realization of a silicon-ring/disk modulator with a horizontal p–n junction.[119] The electrical and thermal tuning electrodes are depicted. Adapted with permission from Xuan *et al.*, Op. Express **22**, 28284 (2014). Copyright 2015 The Optical Society.

into a 6.2 dB dynamic ER under a 40 Gbps transmission rate (OOK) with a 4.8 V peak-to-peak RF signal and a moderate static (-2.6 V) reverse bias. SISCAP configurations also allow for similar performance, as demonstrated in Ref. 120 for a 2.4-μm-radius disk incorporating a vertical capacitor configuration (Fig. 10). An 8 dB dynamic ER at a 44 Gbps transmission rate (OOK) with a 2.2 V_{pp} RF signal and only a -0.5 V static reverse bias were shown. Notably, the reported resonance-frequency shift per volt reached 250 pm/V, an order of magnitude larger than configurations relying on carrier-depletion/injection mechanisms.[121,122]

Recently, more sophisticated modulation schemes were introduced to allow for a more efficient bandwidth usage. In ring cavities, for example, four or even eight levels of driving voltages were used to introduce 4-PAM and 8-PAM modulations, respectively. Such approaches led to a significant data-rate increase, with up to 160 Gbps transmission rates being reported in the literature.[108,122,123] MZMs on the other hand exhibit more flexibility in IQ modulation schemes, which can be realized using nested interferometers in each parent branch or by appropriately driven cascaded phase shifters.[15] Although such schemes require more complex electrical circuits, single- or double-polarization 4-PAM,[106] QPSK,[105] and 16-QAM[107,124] modulations have been successfully demonstrated, with the reported symbol rates typically reaching 50 GBd, resulting in data rates up to 240 Gbps for single-polarization[107] or 320 Gbps for dual-polarization 16-QAM.[124]

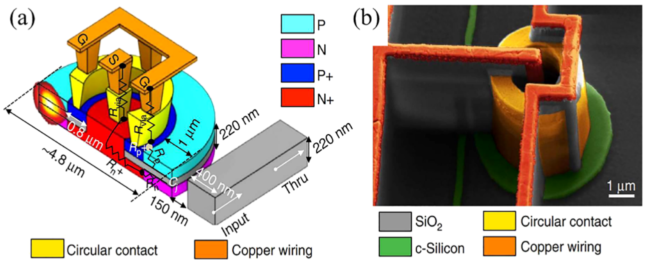

FIG. 10. (a) Schematic and (b) practical realization of a SISCAP-based disk resonator with a vertical capacitor configuration. The mode overlap with the carrier-accumulation region is marked.[120] Reproduced from Timurdogan *et al.*, Nat. Commun. **5**, 4008 (2014). Copyright 2014 Author(s), licensed under a CC BY-NC-SA 3.0 License.

Other alternatives have also been considered in Si modulators, such as slow-wave structures, which increase the phase-shifting efficiency due to the reduced group velocity of the guided light; works on Bragg gratings and photonic-crystal structures report notable metrics.[121,125,126] Nevertheless, the increased footprint and the relatively challenging design and fabrication processes limited the initial interest. A different alternative, systematically examined in the past few years, concerns the forced introduction of second order nonlinearity (Pockels effect) in Si. Being centrosymmetric by nature, $\chi^{(2)}$ nonlinearities in silicon are introduced by applying a mechanical strain on the crystal, which breaks its symmetry, typically by using silicon-nitride cladding and exploiting the introduced lattice mismatch.[127] Simulations indicate the introduction of a maximum $\chi^{(2)}$ of a few pm/V but unevenly distributed in the Si core.[128] Practical realization of such modulators is in its early stages and shows moderate potential.[129] Alternatively, the Pockels effect can be introduced through the integration of silicon with linear EO materials such as lithium niobate (Sec. III A) or EO polymers (Sec. III D).

Similarly, the lack of electro-absorption effects (the Franz–Keldysh effect and QCSE) in silicon can be overcome through integration with III–V semiconductors, as already discussed in Sec. III B. Due to its indirect (direct) bandgap of 1.12 eV (3.4 eV), electro-absorption at the NIR regime is principally not supported in silicon. In contrast, germanium, the second most popular group-IV semiconductor, exhibits, along with its fundamental indirect bandgap of 0.66 eV, a direct bandgap of 0.8 eV, which corresponds to telecom wavelengths and could be modulated for tunable absorption. The easy integration of germanium with silicon, already exploited in electronics, is a major advantage compared to the challenging III–V-on-silicon integration. EAMs exploiting the Franz–Keldysh effect in bulk Ge[130–134] and $Si_{1-x}Ge_x$ alloys[135–137] as well as the QCSE in Ge/SiGe quantum wells[138–140] have been successfully demonstrated. In each case, the wavelength of optimum modulation efficiency may differ, and suitable engineering is often required for adjusting to the frequently employed telecom wavelengths. The EO effect is almost exclusively induced through a reverse-biased p–i–n junction under the application of a few volt swings, and it can be comparable to that in III–V semiconductors. Insertion losses, however, appear increased due to absorption from the indirect lower-energy bandgap of Ge. The modulation length does not exceed a few tens of micrometers, allowing for sub-fJ/bit energy-consumption estimates.[140] Recent demonstrations have also reported EO-bandwidth values greater than 50 GHz,[132,133,137] which have been successfully translated into bit rates as high as 200 Gbps (16-QAM).[141] Phase modulation is also possible, exploiting electro-refractive effects in SiGe layers[142] and Ge/SiGe quantum wells,[143] with a $V_\pi L$ product equal to 0.81 V cm reported in Ref. 142 for a 4 dB/mm of propagation loss. We also note that strained SiGe has been experimentally verified to support enhanced free-carrier effects compared to silicon.[144]

Finally, as with lithium-niobate modulators, the electrode design plays a crucial role in the BW and energy consumption of silicon modulators.[15,109] TWEs exhibit the challenges discussed in Sec. III A; to overcome these issues, sophisticated designs are commonly adopted with the implementation of perpendicular metallic segments (wire- or T-shaped)[117] to modulate the transmission-line conductance/inductance and, thus, improve the phase-matching between RF and optical guided modes and, consequently, the EO bandwidth. Copper and aluminum are the most popular options for the electrodes, approaching heavily doped silicon with carefully designed, zigzagged vias to further control resistance and capacitance.[114,115,117] On the other hand, lumped electrodes have several advantages[15] such as significantly lower power consumption, more flexibility in their design to control the induced capacitance/inductance (given that EO BW is RF-limited), and the absence of the 50 Ω impedance-matching requirement. Electrodes implemented in resonant-modulator structures are by nature lumped (small dimensions compared to the RF-signal wavelength), but there exists an interest for lumped electrodes in MZI configurations as well. This becomes possible by using, e.g., folded (meandered) waveguides[109] or Sagnac loops to recycle light propagation.[145] The use of segmented MZMs has also been suggested.[146,147] Discretizing the long phase-shifting elements into multiple shorter segments allows each segment to be separately driven as a lumped element of a reduced RC constant. Typically, each segment is driven with an identical signal, suitably delayed to account for the optical delay between the segments. As a result, the EO bandwidth appears improved at the expense of increased driver power consumption. Compared to TWE approaches, the segmented scheme avoids the requirement for impedance terminations as well as the RF losses introduced by the transmission lines.

D. Electro-optic polymers

Electro-optic polymers provide an instantaneous pure phase shift, exactly as in lithium niobate. The active molecules are organic chromophores[148] with high molecular hyperpolarizability in a chromophore-polymer guest–host material system; chromophores are typically limited to 25 wt. %. Polymer deposition or filling is based on spin coating at low temperature, and the EO polymer can be combined with almost any material. After deposition, the electro-optic coefficient is zero due to the random orientation of the dipolar chromophores. Poling using a DC bias at a fabrication stage provides alignment of the active chromophores along the direction of the poling electric field and takes place at elevated temperatures close to their glass-transition temperature T_g; cooling is performed while still maintaining the poling field to freeze the chromophore orientation. With this process and after poling field removal, the chromophores remain aligned, and their high molecular hyperpolarizability translates into large macroscopic EO activity (r_{33}) in the material.[148] Polymers with r_{33} exceeding 300 pm/V are available,[149,150] and theoretical values of chromophore hyperpolarizability predict r_{33} values even above 1000 pm/V. Such EO coefficients exceed those of LN by a factor of 10 or higher. Refractive indices of most polymers in the near infrared are in the 1.5–1.7 range, with similar refractive indices exhibited at microwave frequencies as well. This facilitates the velocity matching between the propagating optical and RF fields when traveling-wave electrodes are used. Long-term stability of EO polymers is of importance, with materials having a higher glass-transition temperature being advantageous. Thermal stability can be improved by cross-linking performed during poling,[151] which results in lattice hardening and increases T_g.

Early polymeric electro-optic modulators were based on MZIs made of waveguides with a large cross section (width in the range of a few microns) and low index contrast, with the EO polymer being the waveguide core material. Successful examples included ridge structures defined by reactive ion etching[152–154] or channels/trenches filled with the EO polymer.[155–157] Popular choices for the host material were Poly(methyl methacrylate) (PMMA) and amorphous polycarbonate (APC). Poling required high, vertically applied voltages of hundreds of volts, and in many prototypes, poling electrodes were removed before the fabrication of the microstrip signal lines.[153,157] For this class of devices, $V_\pi L$ values of a few V cm were routinely reported in experimental demonstrations together with static extinction ratios above 20 dB, thus allowing for sub-1-V operation in devices that were 2–3 cm long.[151,155,156] Importantly, the potential for substantial EO bandwidth, well-exceeding 100 GHz, was experimentally demonstrated very early.[154]

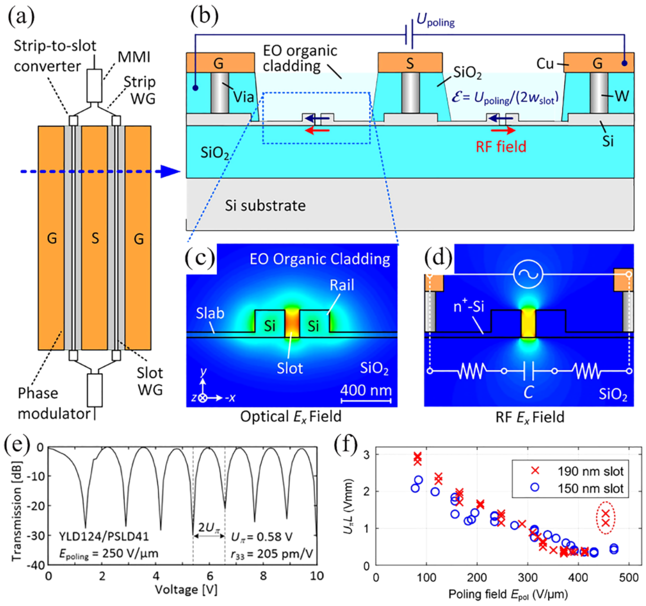

FIG. 11. Silicon-organic hybrid Mach–Zehnder modulator.[173] (a) Top-view schematic showing the slot-waveguide phase modulators and the coplanar waveguide carrying the modulation signal. (b) Cross section showing the Si-slots connected to the CPW with tungsten vias and the direction of the poling field (blue) and the RF field (red). (c) Optical mode profile. (d) RF mode profile. Adapted with permission from Koos *et al.*, J. Lightwave Technol. **34**, 256 (2016). Copyright 2016 IEEE. (e) Experimental voltage-dependent transmission for a 1-mm-long SOH MZM when the EO cladding is the binary-chromophore system YLD124/PSLD41.[168] Adapted with permission from Palmer *et al.*, J. Lightwave Technol. **32**, 2726 (2014). Copyright 2014 IEEE. (f) Measured $V_\pi L$ product for two different slot widths vs poling field.[171] Adapted with permission from Kieninger *et al.*, Optica **5**, 739 (2018). Copyright 2018 The Optical Society.

Alternatively, the EO polymer can be introduced as the cladding material in a silicon-core waveguide. A device characterized by fabrication simplicity was demonstrated in Ref. 158 with an ultra-thin (50 nm) silicon core overlaid by polymer; for a 10-mm-long device, a V_π of 0.9 V was measured together with a 3-dB bandwidth of 23 GHz.

It was theoretically understood in Ref. 159 that the silicon-slot waveguide holds significant potential as the underlying structure to accommodate the EO polymer due to the high mode confinement in the slot area, in particular, for narrow (sub-100 nm) slots. Shortly after, experimental demonstrations[160,161] reported polymer-clad silicon-slot modulators with $V_\pi L$ below 1 V cm.

The polymer-clad silicon-slot waveguide that provides phase modulation is the fundamental building block of more complex devices that subsequently implement various modulations formats, ranging from the simplest intensity modulation (OOK) to advanced multi-level formats; this is collectively referred to as the silicon-organic hybrid (SOH) platform[162–172] that was intensively developed for over a decade and reached high levels of performance. Figures 11(a) and 11(b) schematically depict a representative MZM of this class, together with the optical mode profile [Fig. 11(c)] and the RF mode profile [Fig. 11(d)].[173] Significant improvement in bandwidth was made possible by the application of a DC gate voltage between the ground electrodes and the silicon substrate inducing an electron-accumulation layer in the thin Si striploads (slabs) that connect to the Si rails, thus lowering their resistance.[162] Signal lines are coplanar waveguides that are advantageous as the poling voltage is efficiently applied between the two ground electrodes [Fig. 11(a)].[164] As shorter devices are sufficient due to the very low $V_\pi L$ product that falls below the limit of 1 V mm, it is also possible to operate the transmission line (CPW) without termination, resulting in further suppression of energy consumption.[169] In this case, energy consumption is mainly attributed to the losses from charging/discharging the slot capacitor and approaches fJ/bit levels. The electro-optic activity can be further boosted by employing mixtures of two chromophores (binary-chromophore organic glasses)[167,168] [Fig. 11(e)] or pure chromophores[169,171] instead of chromophore–polymer guest–host systems; in Ref. 171, the $V_\pi L$ product dropped to 0.32 V mm [Fig. 11(f)]. Improvements in the SOH platform lead to IQ modulators that can be directly driven by FPGA outputs[170] at voltages below 0.5 V, thus avoiding digital-to-analog converters or drive amplifiers. Many different modulation formats were successfully tested at different symbol rates, including OOK, 4-ASK, 8-ASK, BPSK, QPSK, and 16-QAM, with the highest reported rate being 100 GBd 16-QAM (400 Gbps) in Ref. 172.

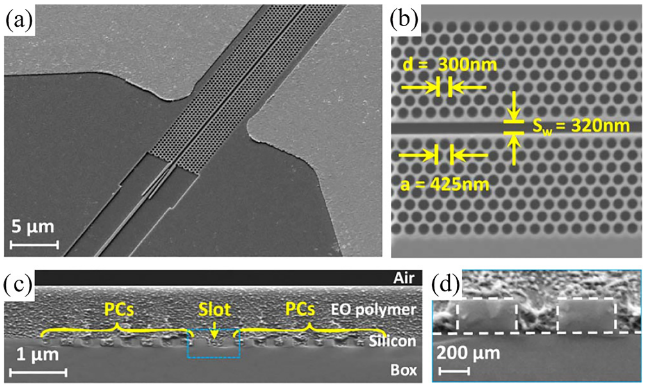

FIG. 12. Silicon photonic-crystal slot waveguide infiltrated with the EO polymer SEO125.[176] (a) Tilted view of the phase modulator showing part of the gold electrodes, the feeding strip waveguide, and the mode converter, (b) the photonic-crystal lattice and the slot, (c) the waveguide cross section after EO-polymer infiltration, and (d) expanded view of the blue rectangle in (c). Adapted with permission from Zhang *et al.*, Opt. Lett. **38**, 4931 (2013). Copyright 2013 The Optical Society.

EO-polymer infiltrated photonic-crystal slot waveguides in silicon were also investigated and successfully employed as the phase-shifting elements in MZIs.[157,174–177] For such devices, enhanced performance is anticipated due to the slow light effect close to the bandgap edge, with the effective (in-device) r_{33} acquiring very high values as intensified by the high group index n_g. Figure 12(a) depicts an SEM image of a photonic-crystal slot waveguide (phase modulator) fed by a silicon strip waveguide through a mode converter section, Fig. 12(b) shows the band-engineered photonic-crystal lattice and the slot, Fig. 12(c) is a cross-sectional view after polymer infiltration of the slot and lattice holes have taken place, and Fig. 12(d) zooms in the slot area.[176] The 300-μm-long device reported in Ref. 176 achieves an average group index $n_g \sim 20$ and exhibits a $V_\pi \sim 0.97$ V ($V_\pi L = 0.29$ V mm); slightly improved performance was reported in Ref. 177 together with a measured EO BW of 15 GHz.

Plasmonic modulators exploiting EO polymers offer a possible route to further footprint shrinkage, where practical devices will be a few tens of microns long. The plasmonic slot waveguide formed by the RF electrodes is the natural choice, with an almost perfect overlap between the RF field and the plasmonic mode.[173,178,179] Bandwidth limitations related to the RC constant are suppressed due to the presence of a highly conducting path that gives a capacitive nature to the device, leading to a theoretical EO response up to 1 THz. Transmission experiments with different rates and formats were conducted (OOK, BPSK, 4-ASK), including 100 Gbps OOK and 60 GBd 4-PAM (120 Gbps) in devices as short as 12.5 μm.[179]

Electro-optic polymer modulators based on resonant structures, such as microrings, are another possibility. Although less studied than MZI designs, many different alternatives have been assessed, theoretically or experimentally, including silicon-nitride rings with EO-polymer top cladding,[180] rings written by direct photo-definition in SU8 containing chromophores,[181] rings made of ultrathin silicon cores overlaid with an EO polymer,[182] micro-disks in hybrid plasmonic (conductor-gap-silicon) waveguides,[183] polymer-infiltrated sub-wavelength grating waveguide ring resonators,[184] and all-polymer rings.[185]

E. Transparent conducting oxides

Conventionally applied to liquid crystal displays and photovoltaics,[186] transparent conducting oxides (TCOs) have attracted considerable interest during the last decade for NIR electro-optic applications due to their large optical tunability and the manifestation of the epsilon-near-zero (ENZ) effect. The material class of TCOs consists of degenerately doped, usually n-type, wide bandgap semiconductors.[34] Well-known representatives include Sn-doped indium oxide (indium tin oxide, ITO), aluminum-doped zinc oxide (AZO), and gallium-doped zinc oxide (GZO). The high concentration of their free carriers, typically between $n_e \sim 10^{19}$–$10^{21}\,\mathrm{cm}^{-3}$, together with the absence of interband transitions allows for the adoption of the Drude model for describing their NIR permittivity $\varepsilon_{\mathrm{TCO}}$ with a plasma frequency $\omega_p \propto \sqrt{n_e}$. In contrast to the ultraviolet and far-infrared plasma frequencies of metals and typical degenerately doped semiconductors, respectively, the plasma frequency of TCOs lies in the NIR regime. This renders them transparent at visible frequencies, while the high concentration of their free carriers and their appreciable mobility ($\sim 50\,\mathrm{cm}^2/\mathrm{Vs}$) ensure high electrical conductivity. These properties have made TCOs the predominant option for realizing transparent electrodes at visible frequencies.

The interest in TCOs has recently been renewed for applications in the field of integrated photonics. Due to their NIR plasma frequency, TCOs exhibit highly dispersive NIR properties, with the carrier-induced change in the real part of the effective mode index, $\Delta n_{\mathrm{eff}}^{\mathrm{Re}}$, calculated an order of magnitude greater in TCO-loaded waveguides than in pure silicon ones.[187] The TCO permittivity spans from dielectric to metallic values, intermediately crossing an epsilon-near-zero region with $|\varepsilon_{\mathrm{TCO}}| \approx 0$. Integrating a thin TCO film ($\sim 10\,\mathrm{nm}$) into standard waveguide structures allows for the manifestation of the ENZ effect for the guided mode that is perpendicularly polarized to the TCO layer. The ENZ effect consists in the significant enhancement of the electric field in the ENZ medium as a result of the boundary condition demanding the continuity of the normal component of the displacement field. The field enhancement results in increased propagation losses that scale with $\mathrm{Im}\{\varepsilon_{\mathrm{TCO}}\}/|\varepsilon_{\mathrm{TCO}}|^2$, suggesting the potential for modulating the losses of a guided wave by changing the complex permittivity $\varepsilon_{\mathrm{TCO}}$ of the TCO layer.

The concept was first introduced in 2010 for an ITO layer sandwiched between two gold electrodes, adding an SiO_2 layer to form a MOS capacitor.[188] Applying an electrical bias between the gold electrodes increased the concentration of free carriers in a nm-region close to the SiO_2–ITO interface due to the field effect, changing the plasma frequency of ITO and, thus, the value of its complex permittivity at the operation wavelength (800 nm). This altered the effective mode index n_{eff} of the plasmonic mode guided in the equivalent metal–insulator–metal (MIM) waveguide. Tuning the free-carrier concentration in ITO through an external bias was suggested as a promising means of modulating the guided wave.

Since then, a plethora of TCO-based modulators has been reported at the telecommunication wavelengths of 1.31 and $1.55\,\mu\mathrm{m}$.[36] A MOS-type junction is almost exclusively selected for controlling the free-carrier concentration in TCO, with ITO being the most usual choice due to its well-studied properties as well as its low resistivity.[189,190] A few-nm thick high-κ dielectric[191] is usually employed for the oxide layer. Plasmonic[192–195] or hybrid plasmonic[196–199] waveguides are commonly preferred as physical structures due to providing enhanced light–matter interaction and easy access for applying the electrical signal. Silicon-photonic designs have also been investigated,[200–203] reporting reduced IL at the expense of larger footprint values. Most works study the simplest OOK modulation scheme in TCO-loaded straight waveguides, modulating the propagation loss by switching between the dielectric and the ENZ region of the TCO film. Fewer works prefer to exploit the carrier-induced changes in the real part of TCO permittivity to investigate MZI,[204,205] resonator-based,[206–208] or phase modulators,[187,209,210] capitalizing on the large changes in $\Delta n_{\mathrm{eff}}^{\mathrm{Re}}$ instead of the highly lossy ENZ region.

Theoretical studies on TCO-based waveguide modulators report a maximum ER of $\sim 1\,\mathrm{dB}/\mu\mathrm{m}$ for an optimally designed Si-slot design,[203] increased to 1.5–$2.5\,\mathrm{dB}/\mu\mathrm{m}$ for hybrid or purely plasmonic designs.[211,212] Regarding phase-modulation schemes, a voltage-length product of 0.15 V mm is calculated for an ITO-loaded Si-slot phase shifter.[187] In all cases, the required bias swing does not exceed 5 V due to the use of high-κ dielectrics, with the respective energy consumption calculated in the order of 1 pJ/bit or less for achieving a 10-dB ER or a π-phase shift.

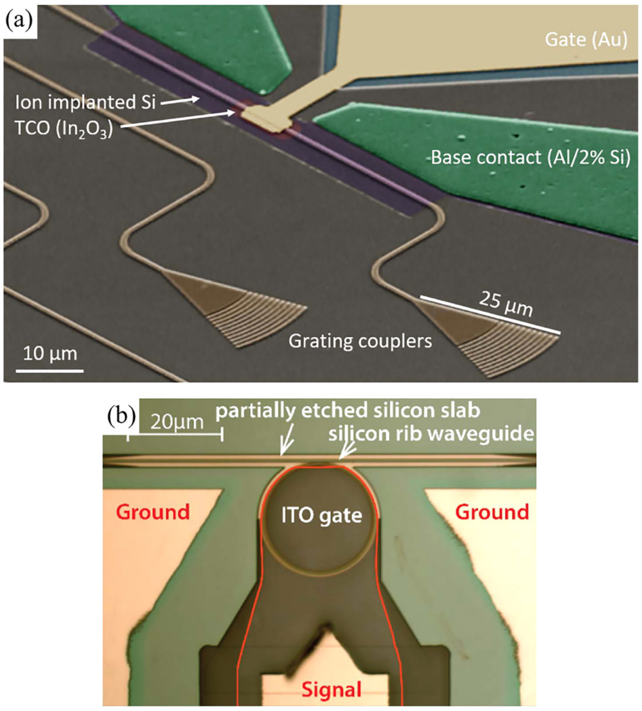

FIG. 13. (a) SEM image of the $Si/HfO_2/In_2O_3/Au$ waveguide modulator in Ref. 216. The bias is applied between the doped Si and Au. An ER of $1.62\,\mathrm{dB}/\mu\mathrm{m}$ is achieved for a 6-V bias swing. A maximum rate of 2.5 Gbps is reported. Adapted with permission from Wood *et al.*, Optica **5**, 233 (2018). Copyright 2018 The Optical Society. (b) Optical image of the $Si/HfO_2/ITO$ microring modulator (radius $12\,\mu\mathrm{m}$) in Ref. 207. The red line highlights ITO. The ground electrodes are connected to Si through a partially etched slab. An ER of 15 dB with an IL of $\sim 5\,\mathrm{dB}$ is reported using a 2-V bias swing. A 12-ns response time is achieved. Adapted with permission from Li *et al.*, Photonics Res. **7**, 473 (2019). Copyright 2019 Chinese Laser Press.

The theoretical EO BW of in-line TCO-based OOK modulators exceeds 100 GHz,[192,195,213,214] whereas that of phase modulators is restricted to a few tens of GHz.[187] Depending on the modulation scheme, the required interaction length spans from a few micrometers (10-dB-ER OOK) to a few tens of micrometers (BPSK) with reference to the Si-slot platform.[187,203] Due to the reduced footprint values of TCO-based modulators, the devices are safely considered lumped regarding the RF signal since the (electrical) length of the required electrodes is sufficiently short. As a result, no traveling-wave effects or termination issues are present, with both energy consumption and bandwidth being ultimately limited by the device capacitance and resistance values.

Recent experimental demonstrations have verified the principle of TCO-based modulators, mostly on hybrid plasmonic[215–217] or purely plasmonic platforms,[195] reporting ERs as high as 1.63[216] and 2.71 dB/μm, respectively, with a bias swing equal to 2 V. In Fig. 13(a), an SEM image of a hybrid plasmonic Si/HfO_2/In_2O_3/Au waveguide modulator is presented.[216] Silicon-photonic implementations have also been investigated,[218] achieving at best an ER of 0.15 dB/μm (Si-slot design) for a 12 V bias swing. A directional-coupling scheme using ITO-loaded silicon waveguides[219] has provided ER = 2 and IL = 2 dB for a 4 μm length and a 4 V bias. Resonator-based modulators[206–208] have reported a maximum wavelength tunability of 271 pm/V, achieving a 15-dB ER for the ITO-loaded silicon microring in Fig. 13(b) for a 2-V bias swing. Recent MZI implementations[204,205,220] have exploited ITO-based phase shifters, with the one in Fig. 14 achieving a markedly low $V_\pi L = 0.095$ V mm, resulting in a 3-dB static ER for a 20-V bias swing.

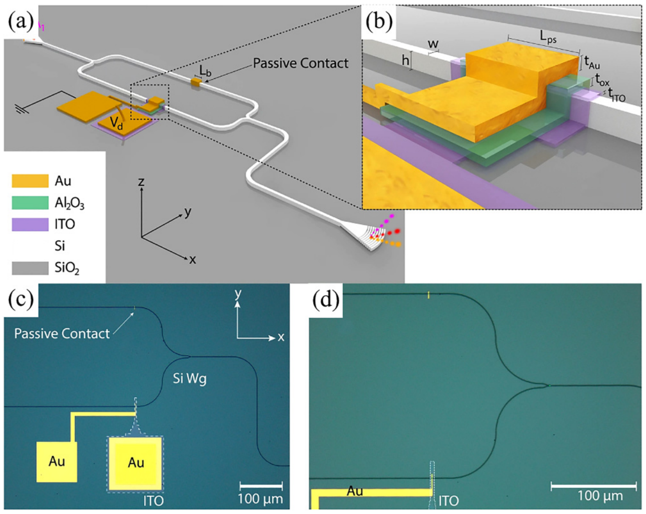

FIG. 14. (a) Schematic of an ITO-based MZM. The passive metallic contact L_b is utilized for loss balancing. (b) Close-up view of the tunable Si/ITO/Al_2O_3/Au region. (c) Optical microscope image of the modulator. The white dashes highlight the patterned ITO film. (d) Zoomed view at the device section formed by ITO (white dashes) and the Au contact, separated by Al_2O_3. The ITO-based phase shifter achieves a voltage-length product equal to 0.095 V mm. MZM exhibits a 3-dB ER, 6.7-dB IL, and a 1.1 GHz bandwidth for a 1.4-μm phase shifter and a 20-V bias swing. Reproduced from Amin *et al.*, Sci. Rep. **11**, 1287 (2021). Copyright 2021 Author(s), licensed under a CC BY 4.0 License.

The major drawback of the exhibited implementations is their excessive ILs as well as their limited bandwidth, which does not exceed the value of a few GHz.[205,216,221] Both issues were attributed to low mobility TCO films and/or non-optimal design options. Despite the open research questions, the metrics of TCO-based modulators appear compatible with state-of-the-art modulation requirements, competing genuinely with the performance of other material platforms.[204,205,214]

F. Two-dimensional materials

Two-dimensional (2D) materials exhibit tunable physical properties under moderate electrical or optical stimuli. Graphene is the best-known representative, but other materials such as silicene, germanene, and germanane, black phosphorus (BP), transition metal dichalcogenides (TMDs) (e.g., MoS_2, WS_2), MXenes (e.g., Ti_3CNT_x, $Ti_3C_2T_x$), and their combinations in Van der Walls heterostructures (e.g., graphene–BP, graphene–TMD, TMD–TMD) have gained a lot of interest lately.[222–225] Manifesting diverse electronic band structures (from the gapless graphene to the indirect to direct bandgap transition in TMDs), 2D materials exhibit diverse macroscopic physical properties. Importantly, their high-frequency (optical) electromagnetic properties (real and imaginary parts of the complex surface conductivity σ_s) are tunable under electrical stimulation and as such are considered for electro-optic (both electro-absorption and electro-refraction) modulation. Typically, the tunability is introduced by electrical gating, which modifies the carrier distribution and consequently affects the allowed electron transitions due to the Pauli blocking principle.

The first experimental demonstration of graphene-based electro-absorption modulators dates back to 2011.[226,227] In Ref. 226, a single-layer graphene (SLG) was overlaid on a standard 40-μm-long silicon-rib waveguide using a thin Al_2O_3 layer for insulation, while in Ref. 227, a stack of graphene–insulator–graphene (GIG) was implemented to increase the extinction ratio over the SLG case from 0.1 to 0.16 dB/μm under moderate voltage (6 V). Nevertheless, the 3-dB BW was limited to 1 GHz because of the RC constant owing to the configuration and quality of the contacts. In the following years, modulation speed was increased by improving the contact quality and positioning, resulting in an EO bandwidth up to 35 GHz,[228] retaining acceptable ERs and reasonable voltage requirements using SLG or GIG structures and optimizing the graphene–light interaction.[228–230] In Ref. 229, a 5.2-dB static ER was demonstrated experimentally in a 50-μm-long n-doped silicon-rib waveguide enhanced with an SLG on-top [Figs. 15(a) and 15(b)], operating in the fundamental TM mode. Light–graphene interactions in longer waveguide segments can lead to higher ERs at the expense of higher ILs [Fig. 15(c)] and a possible modulation speed reduction. On the other hand, in Ref. 231, a compact MIM plasmonic modulator with graphene was demonstrated; despite the relatively high ER per unit length (0.13 dB/μm), the reported extinction ratio was poor in order to keep ILs reasonable (0.68 dB/μm). Theoretical works with hybrid plasmonic

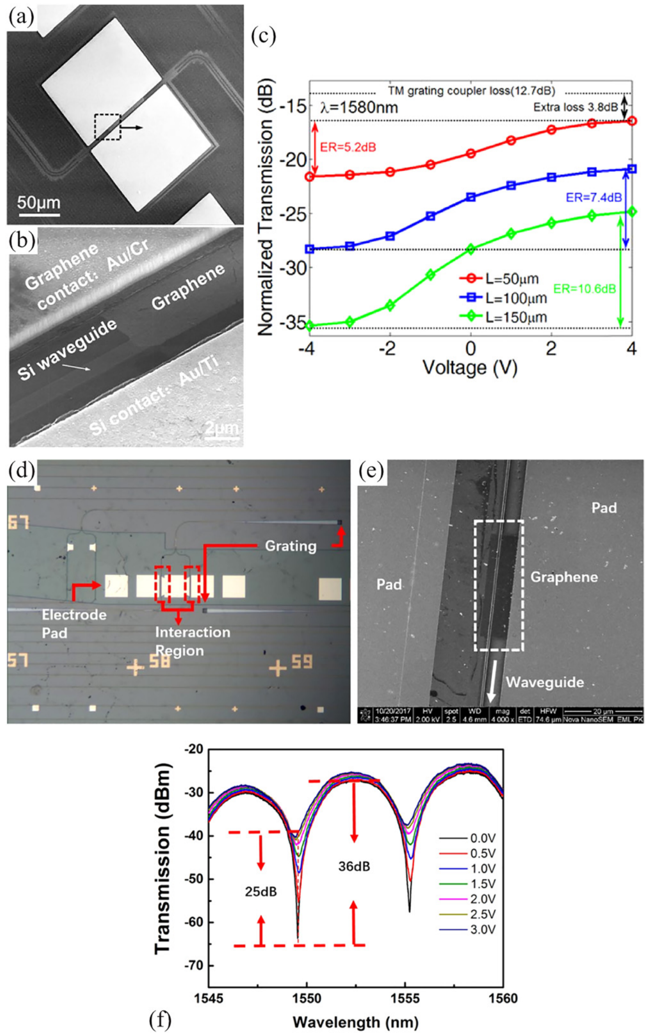

FIG. 15. Experimentally demonstrated graphene-based EAM and MZM in the silicon platform. (a)–(c) Silica-clad silicon-rib waveguide overlaid with a single graphene layer.[229] A 5.2-dB extinction ratio with a 6.1-GHz BW was demonstrated. Reproduced with permission from Hu *et al.*, Laser Photonics Rev. **10**, 307 (2016). Copyright 2016 Wiley-VCH. (d)–(f) Silica-clad silicon MZM. Both its arms were overlaid with an SLG. A very high static ER of 25 dB was demonstrated. Reproduced from Shu *et al.*, Sci. Rep. **8**, 991 (2018). Copyright 2018 Author(s), licensed under a CC BY 4.0 License.

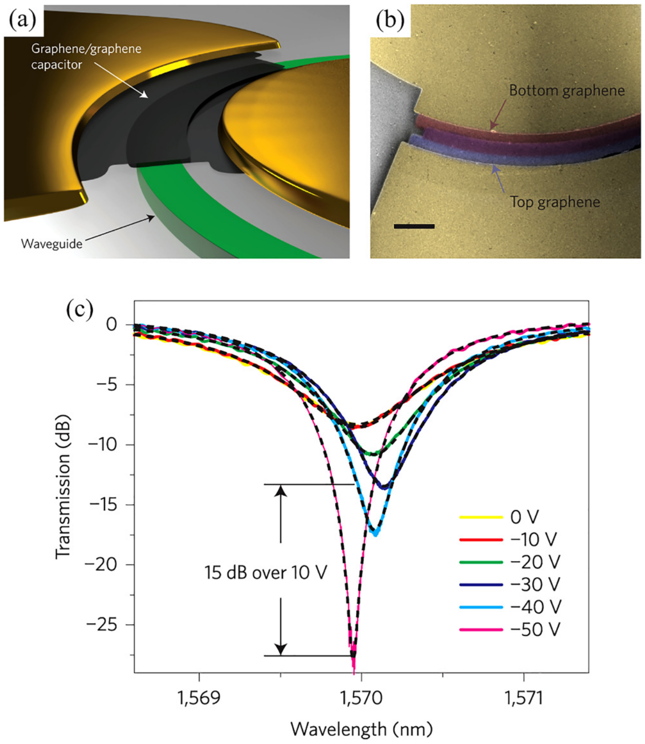

FIG. 16. Silica-clad silicon-nitride ring resonator overlaid with a GIG layer for optical modulation.[237] A notable 15-dB ER over 10 V was demonstrated, topping at ∼20 dB over 40 V, with a 30-GHz EO bandwidth. Adapted with permission from Phare *et al.*, Nat. Photonics **9**, 511 (2015). Copyright 2015 Springer Nature.

waveguides reveal a potential for modulation,[232,233] but practical realization and experimental verification remain challenging.

Electro-refractive modulators incorporating graphene have also been extensively studied because of the capability to tune graphene properties under moderate voltage. The first experimental demonstration of an integrated silicon MZI overlaid with graphene showed a poor $V_\pi L$ of 30 V cm with high insertion loss.[235] In Ref. 234, a significantly reduced $V_\pi L = 0.13$ V cm was demonstrated with a 25-dB static ER [Fig. 15(f)]. The MZI configuration (top view) is shown in Figs. 15(d) and 15(e) (optical and zoomed SEM images, respectively), having an SLG on the top of the silica-clad silicon-rib waveguide and a thin Al_2O_3 insulating layer. Each MZI branch has a 40 μm interaction length with graphene. A similar but larger design (300–400 μm interaction length) was also reported in the same year with a two times higher voltage-length product (0.28 V cm) and equally high static ER (35 dB), demonstrating a 5-GHz electro-optic bandwidth.[236]

Another possible configuration to minimize footprint (at the expense of optical bandwidth) is a ring-resonator cavity. In principle, for a cavity operating near the critical-coupling condition, tuning the properties of graphene will lead to abrupt changes in both frequency and lineshape of the resonance, allowing for high-performance metrics.[214] Early experimental confirmation in a silica-clad silicon-nitride ridge waveguide with a GIG on the top, covering only a fraction of the ring circumference [Figs. 16(a) and 16(b)], revealed a high static ER of 15 dB with an EO BW of 30 GHz (limited by the RC constant and not the photon lifetime of the cavity) and acceptable insertion losses [Fig. 16(c)].[237] On the contrary, a fully covered ring with an SLG layer turned out to be insufficient to induce the

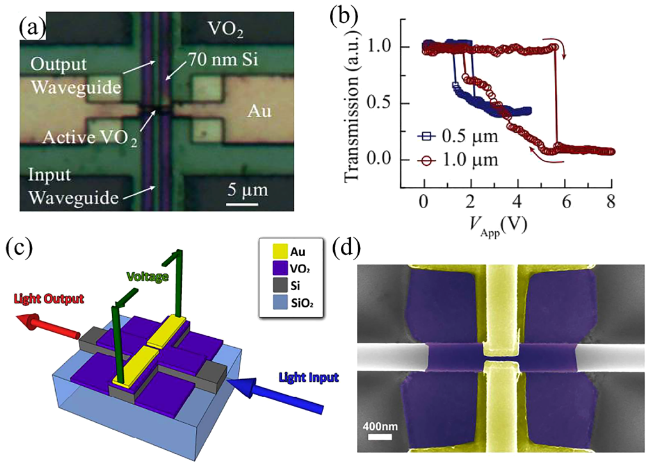

FIG. 17. Experimentally demonstrated VO$_2$-based modulators based on silicon-photonic waveguides. (a) and (b) Silicon-ridge waveguide coated with a 1 μm-long VO$_2$ strip.[242] An ER of 12 dB was experimentally demonstrated. A shorter modulator length (0.5 μm) reduces the voltage requirements at the expense of lower ER. Adapted with permission from Joushaghani *et al.*, Opt. Express **23**, 3657 (2015). Copyright 2015 The Optical Society. (c) and (d) Silicon wire coated with VO$_2$.[243] Using 10-ns voltage pulses and limiting the current passing through the device to harness only the electronically induced transition, switching speeds as fast as 2 ns were reported. Adapted with permission from Markov *et al.*, ACS Photonics **2**, 1175 (2015). Copyright 2015 American Chemical Society.

necessary changes in n_{eff}, resulting in a poor 3.5-dB ER,[238] owing possibly to the experimental conditions (relatively low bias voltage). A few works with photonic-crystal (standing-wave) resonators have also appeared in the literature[239,240] showing high performance (ER $>$ 10 dB).

G. Phase-change materials

Phase-change materials experience a phase transition that can be driven electrically and are being actively considered for both volatile (e.g., modulation) and nonvolatile (e.g., memory) electro-optic applications. In this section, we focus on the exploitation of VO$_2$ in integrated silicon-photonic modulators, which is the most widely investigated PCM-based modulator platform.[241]

Efficient electro-optic modulators can be demonstrated by integrating VO$_2$ inclusions in a waveguide and exploiting the different waveguiding characteristics at the two states of VO$_2$ (insulating and metallic) by engineering the mode overlap with the material. In Ref. 242, an EAM with a high extinction ratio reaching 12 dB has been experimentally demonstrated by coating a silicon-ridge waveguide with a strip of VO$_2$, which is only 1 μm long along the propagation direction [Fig. 17(a)]. The VO$_2$ strip can even be shorter (0.5 μm), reducing the voltage requirements for switching to the metallic state (corresponding to low transmission due to higher loss) but at the expense of a lower extinction ratio [Fig. 17(b)]. A similar geometry has been studied experimentally in Ref. 243 [Figs. 17(c) and 17(d)]. By using 10-ns voltage pulses and limiting the current passing through the device to avoid thermal effects and harness only the electronically induced transition, switching speeds as fast as 2 ns were reported.[243] However, in this case, only a small fraction of the material was switched to the metallic state, limiting the extinction ratio to ∼1 dB.

In recent years, several different approaches to the design of silicon-based VO$_2$ modulators have theoretically been explored in the literature[244–249] (lacking, however, experimental verification) and include tailoring the position of the VO$_2$ inclusion in the waveguide configuration, exploiting coupled waveguides, and harnessing plasmonic effects. In Ref. 247, VO$_2$ is integrated in the gap of a silicon-slot waveguide to enhance a mode overlap with the material and achieve maximum disparity of the waveguiding characteristics in the two states. As a result, an ER of 21 dB is attained with a component length of 1 μm. Plasmonic waveguiding effects aiming to miniaturize the waveguide cross section have also been exploited,[244–246,248,249] relying on variants of hybrid silicon-plasmonic waveguide configurations (conductor-gap-silicon[250] and symmetric/long-range conductor-gap-silicon[251] geometries). In Ref. 245, a CMOS-compatible electro-absorption modulator based on a Si/SiO$_2$/VO$_2$/Cu hybrid plasmonic waveguide has been proposed that offers extinction ratios of 3.9 and 8.7 dB for the fundamental TE and TM modes, respectively. Plasmonic effects in a chain of metallic disks patterned on a hybrid plasmonic waveguide have resulted in a modulator design with an ER of 9 dB/μm.[246] Instead of a single waveguide segment, synchronization effects between supermodes in coupled-waveguide systems can also be exploited for designing modulators (as well as switching and routing) devices.[244,248] In Ref. 244, a directional coupler scheme between a silicon waveguide and a hybrid plasmonic waveguide exploiting VO$_2$ as the plasmonic material was designed with an extinction ratio exceeding 3 dB in the entire C-band. However, the coupled-waveguide strategy results in an increased component length reaching 10 μm.

IV. PERFORMANCE TRENDS AND IMPORTANT DESIGN ASPECTS

A. State-of-the-art performance and trends

Electro-optic modulators employ either a loss- or a phase-tuning unit for modulating the guided wave. Figure 18 compiles and compares the modulation efficiency of such units for the material platforms discussed in Sec. III. In each case, modulation efficiency is quantified through the appropriate metric, extracted from the respective experimentally demonstrated modulators. Beginning with loss-modulating units [Fig. 18(a)], efficiency is quantified by the ER achieved per unit length and the respective IL penalty. The values are extracted from in-line modulators in the literature after excluding coupling losses stemming from, e.g., grating couplers and tapered sections. Loss-modulating units capitalize on the electro-absorption effect in III–V and Si-Ge platforms, as well as 2D materials. Alternatively, optical losses can be modulated by tuning the interaction between the optical electric field and free carriers in the material. This mechanism is highly efficient in TCO-based modulating units due to the field enhancement provided by the ENZ effect, and it is also exploited in phase-change materials through the transition from the insulating to metallic state. Adopting the ratio ER/IL as a metric of modulation efficiency [contour lines in

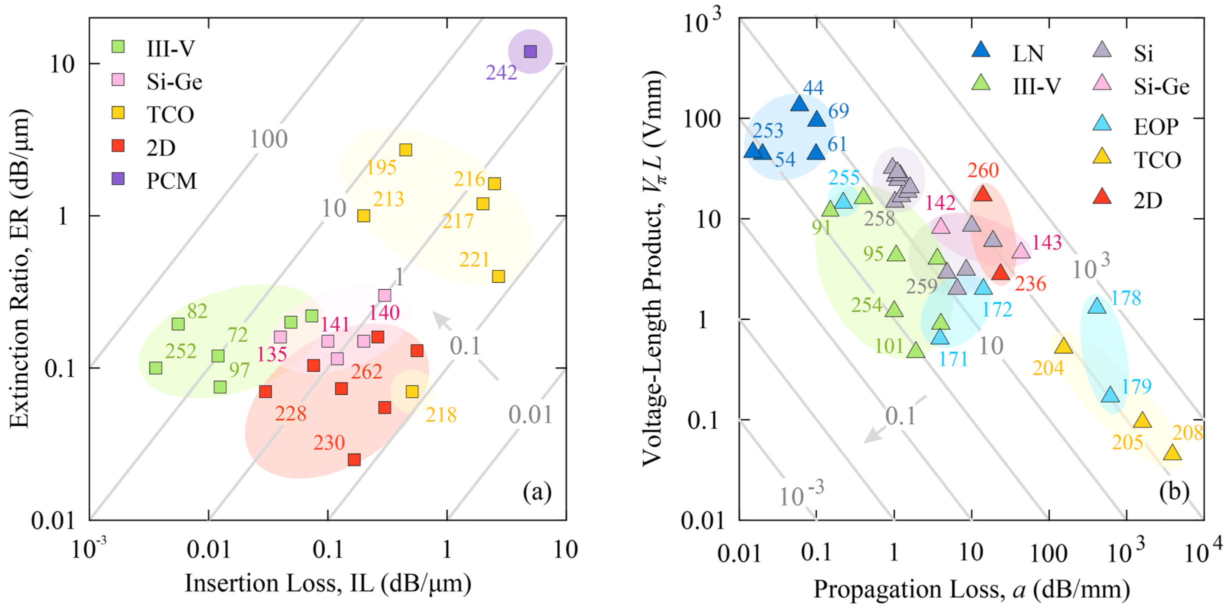

FIG. 18. Comparative assessment on the level of modulating unit. Efficiency of (a) loss- and (b) phase-modulating units, as extracted from experimentally demonstrated EO modulators in the literature. (a) Extinction ratio (dB/μm) as a function of introduced insertion loss (dB/μm) for loss-modulating units employed in waveguide amplitude modulators. Contour lines correspond to the modulation-efficiency figure of merit given by the ratio ER/IL. (b) Voltage-length product as a function of propagation loss for phase-shifting units, either standalone or integrated in MZI and resonant modulators. Contour lines correspond to the modulation-efficiency metric $V_\pi\, L\, a_{\mathrm{dB}}$ (units of V dB). Arrows in each panel indicate the direction of higher modulation efficiency. Characteristic references are included as well.

Fig. 18(a)], III–V-based modulating units exhibit the highest efficiency,[82,252] closely followed by the Si-Ge platform.[135] However, integration challenges of the former with standard silicon-photonic circuitry could render the latter more favorable. The less mature platforms comprising TCO and 2D materials exhibit a wider distribution of performance metrics, which could be attributed to varying quality of the deposited samples. The latter also affects the level of ILs, which could be reduced for samples with higher carrier mobility values. A thorough performance evaluation should also consider the required driving voltage, which does not exceed a few volts in the case of III–V and Si-Ge platforms. Higher values are typically reported for TCO and 2D platforms, where the use of high-κ dielectrics is suggested as a possible solution. Electro-optic bandwidth can also be proven as a limiting factor for some platforms (e.g., PCM) toward demonstrating high-speed modulators.

Next, phase-shifting units are examined in Fig. 18(b); their modulation efficiency is quantified in terms of their $V_\pi L$ product and the propagation loss a of the underlying waveguide. The metrics were extracted from literature works on phase shifters, MZMs, operating either in single-arm or push–pull configuration, and resonant modulators. To establish a common reference point, $V_\pi L$ was adjusted to indicate the required bias V_π in order for a standalone waveguide to accumulate phase π after length L. The propagation loss of the waveguide was deduced from the usually reported total IL of the modulator, subtracting contributions from grating or MMI couplers, Y-junctions, etc., to retrieve the loss introduced by the phase shifting unit itself. In the case of bias-dependent propagation loss (e.g., TCO-based examples), the low-loss state was considered. Note that complete data were not always available, and losses may be in some cases overestimated.[172,179] Figure 18(b) displays a large span for the $V_\pi L$ product, starting from ∼100 V mm in the case of LN-based phase shifters and reaching values as low as ∼0.1 V mm for TCO-based examples. The respective propagation loss spans many orders of magnitude as well. Introducing the loss-efficiency product $V_\pi\, L\, a_{\mathrm{dB}}$ (units of V dB) as a figure of merit for phase-shifting efficiency [contour lines in Fig. 18(b)], LN,[54,253] III–V,[91,101,254] and EOP[171,255] platforms demonstrate phase-shifting units of equivalent efficiency (∼1 dB V), each striking a different balance between the $V_\pi L$ product and the propagation loss. Pure silicon-photonic demonstrations fall slightly behind, and they can be roughly grouped in two main families depending on the employed control mechanism (depletion[256–258] or carrier-injection[110,259]). Depletion-based schemes provide higher $V_\pi L$ products but also lower propagation losses. The lower right quadrant of Fig. 18(b) is mainly occupied by plasmonic EOP-[178,179] and TCO-based[204,205,208] phase shifters, which achieve record-low $V_\pi L$ values, highly desirable for ultra-compact and/or low-voltage phase shifters. Their high propagation losses could be mitigated by restricting on-chip lengths to only a few microns, maintaining thus the total IL at acceptable levels.

Figure 19 collectively compares experimentally demonstrated modulators at the component (modulator) level, reporting the ER/IL ratio (modulation efficiency) [Fig. 19(a)] and the EO bandwidth [Fig. 19(b)]. In-line (squares), MZI (triangles), and resonant

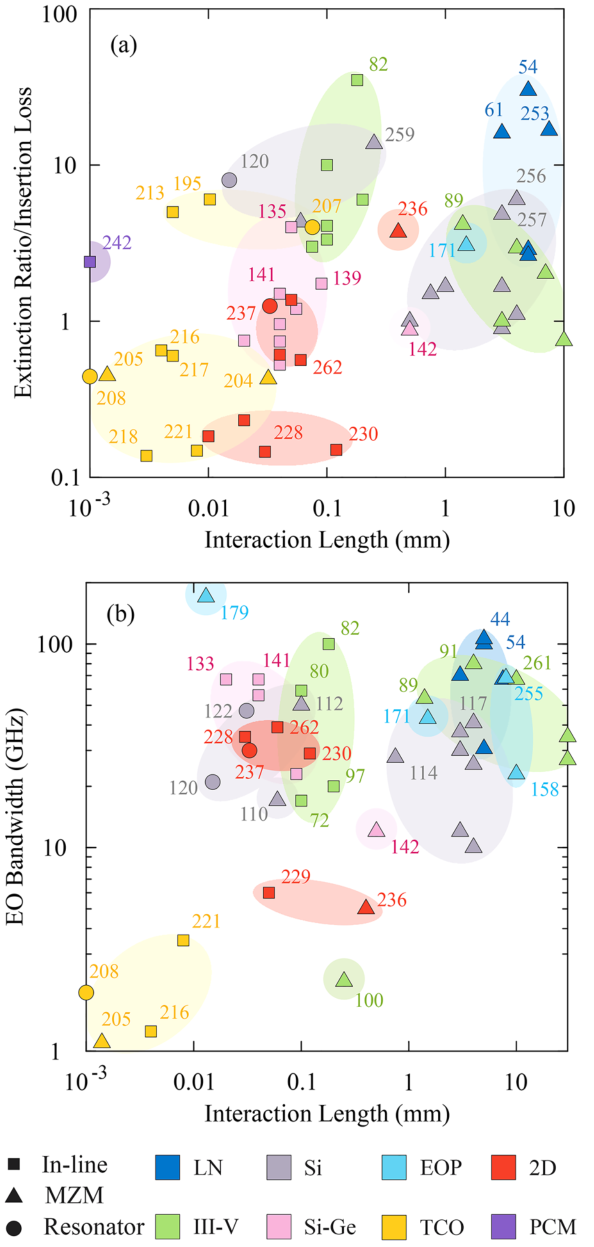

FIG. 19. Comparative assessment on the level of component. Performance metrics of demonstrated EO amplitude modulators employing in-line, MZI, or resonant configurations. (a) Ratio between the (static) ER and IL and (b) EO bandwidth, both as a function of the interaction length between the guided wave and the configurable material. Characteristic references are included as well.

(circles) modulator configurations are considered. One-to-one correspondence of data in the two panels of Fig. 19 is not always possible due to the lack of the corresponding data. We restrict the comparison to the case of amplitude modulators. For the ER/IL ratio [Fig. 19(a)], ER is the static ER and IL refers to the total on-chip loss, excluding coupling losses from input/output grating couplers. The basis of comparison (horizontal axis) is the *interaction length*, defined as the length of the interaction between the guided wave and the configurable material (e.g., the length of the phase shifter in an MZI arm or the arc in the circumference of a ring resonator where the configurable material is integrated). It is used in place of the footprint value, which cannot be safely calculated across the different experimental setups, where additional components such as grating and directional couplers or metallic contacts and TWEs are included. This is particularly evident in the case of MZMs, where the employed Y-junctions or MMIs contribute significantly to the overall component footprint. Since these contributions are not related to the modulation effect itself, we consider the interaction length as a more appropriate basis of comparison.

Two regimes are identified in Fig. 19(a); the majority of MZMs populate the right side of the panel, leaving in-line and resonant modulators on the left side. This is due to the bulky size of MZMs as a result of the requirement for phase accumulation. On the other hand, their interferometric operation grants them with high ER values well-exceeding 20 dB for an IL penalty of only a few dB.[54,61,253] Overall, their modulation efficiency does not drop below unity, with the exception of TCO-based MZMs,[204,205] which are challenged by maintaining both acceptable ILs (short interaction length) and low driving voltages to avoid dielectric breakdown.

In-line and resonant modulators are considerably more compact, which is very attractive for on-chip applications. Their modulation efficiency can be comparable to that of MZMs (reaching ∼10), even though challenges exist for the less mature material platforms. Samples of higher quality will reduce IL and improve the modulation efficiency. While in-line modulators leverage changes in the mode loss, resonant configurations are more suitable for material systems with a predominately electro-refractive behavior. Such materials include the conventional Si[120] as well as novel systems as the WS$_2$ monolayer.[260] Resonant modulators capitalize on the enhanced interaction between the guided mode and the configurable material in the cavity. Their performance, however, is sensitive to shifts in the resonance wavelength due to fabrication imperfections or thermal effects (in contrast to the more robust behavior of in-line modulators). Such shifts can usually be externally corrected with heaters at the expense of increased complexity and energy consumption.

In terms of EO bandwidth, Fig. 19(b) compiles and presents EO modulators with an experimentally demonstrated bandwidth greater than 1 GHz as a function of interaction length. Values around 50 GHz or above have been measured by the majority of the considered material platforms, including in-line EAMs based on III–V,[80,82] Ge,[133] and SiGe[141] semiconductors, as well as MZMs with phase shifters employing LN,[44,54,61,253] III–V,[89,91,261] Si,[112] SiGe,[133] and EOPs[171,179,255] in addition to an Si-based ring modulator.[122] Such values are suitable for achieving bit rates higher than 100 Gbps by simply employing a 4-PAM modulation scheme. Quite fewer modulators have demonstrated an EO bandwidth exceeding 100 GHz, including a III–V-based EAM[82] and two LN-based MZMs,[44,54] with the record-high 170-GHz EO bandwidth of Fig. 19(b) belonging to the plasmonic EOP-based

MZM reported in Ref. 179. Regarding the less mature material platforms, an EO bandwidth as high as 39 GHz has recently been demonstrated for a double-graphene EAM in Ref. 262, while the experimentally measured EO bandwidth of TCO-based modulators has yet to exceed 3.5 GHz.[221] Similarly, a III–V/Si MOS capacitor MZM has demonstrated an EO bandwidth as high as 2.2 GHz,[100] rather limited by the inefficient delivery of the RF signal.

Observing Figs. 18 and 19 from a materials perspective, conventional options such as LN, III–V, or Si are suitable for EO modulators of high modulation efficiency (ER/IL > 10) with bandwidth values exceeding 50 GHz, allowing thus for bit rates greater than 100 Gbps even with the aid of simple, low PAM modulation formats. However, they fall behind in terms of the $V_\pi L$ product and footprint when compared with contemporary options (TCOs, EOPs, 2D materials). The continuing research for novel materials is justified by the desire for reduced footprint, with the challenge being the experimental demonstration of low-loss and high-bandwidth modulators; both shortcomings related to the quality of the demonstrated samples, an issue that we believe will be resolved as the underlying physical effects become better understood and the fabrication techniques more mature. Of equal importance is the energy consumption of EO modulators, which, despite its significance, has not yet been discussed for reasons that are explained in detail in Sec. IV D.

B. Modeling considerations

The accurate modeling of the underlying physical phenomena is fundamental for fully understanding and correctly quantifying the modulation effect. This is essential for efficiently designing the EO modulators and realistically evaluating their modulation performance before actually fabricating the components. It has been observed that even for the same material platform, theoretical predictions can often vastly differ, occasionally reporting contradicting predictions; in addition, correlation of experimental to numerical data often appears very poor, with the experimental performance appreciably falling behind theory. This has been the case, for example, with graphene- and TCO-based modulators and strongly relates to the theoretical description of the underlying physical effects. In many instances, the origins of such discrepancies are traced to lack of rigor in adopted theoretical models.

Early works in graphene-comprising modulators treated graphene as a thin layer of bulk material, whose thickness was set from 0.33 nm up to a few nanometers, subject to the number of graphene layers assumed as well. Its optical properties were expressed in terms of an effective bulk permittivity. The ascribed value highly depended on the assumed thickness, as well as the adopted surface conductivity from which it originates, leading to ambiguous material properties. Initially, graphene was considered a thin *isotropic* bulk medium; this led to an artificial interaction with the electric-field component lying normal to its plane. As its chemical potential was varied and the effective permittivity shifted from dielectric to metallic values, a spurious ENZ effect was manifested (resembling the case of TCO materials), resulting in unnaturally impressive modulation metrics, especially for large values of its thickness.[263–265] Clearly, the most natural representation of graphene that avoids such issues is as a 2D conductive sheet that can support a surface current and that is characterized by a complex surface conductivity (measured in siemens). This approach is more straightforward, unambiguous, and computationally efficient.[266] Nevertheless, it has been shown that the effective bulk medium description can also be accurate as long as the thickness is set to physically reasonable values (~1 nm) and that the physical anisotropy of graphene, i.e., the inability to support an out-of-plane current, is correctly considered.[267]

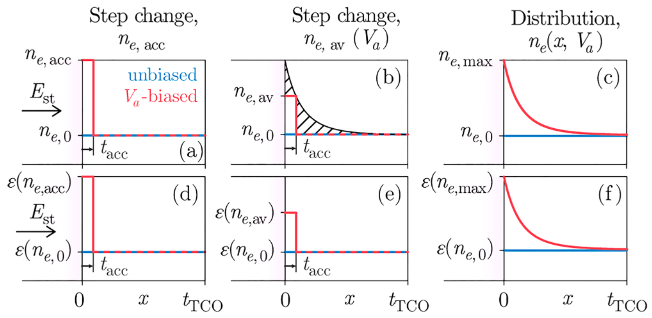

FIG. 20. Techniques for representing the TCO free-carrier concentration under the field effect. (a) and (b) Step index change over a thickness of t_{acc} from the flatband value of $n_{e,0}$ to $n_{e,\mathrm{acc}}$ and $n_{e,\mathrm{av}}(V_a)$, respectively, under the effect of field E_{st}. (c) Continuous distribution $n_e(x, V_a)$ with exponential decay from the peak located at the TCO/insulator interface to the $n_{e,0}$ level. (d)–(f) Respective changes in the optical permittivity profile (real part only).

On another topic, most publications in TCO-based modulators adopt approximate techniques for the description of the developing carrier density and for mapping the carrier density to variations in the TCO optical permittivity. Figure 20 outlines the three approaches that are followed in the literature. The simplest possible technique, Fig. 20(a), is that of appointing a step change in the carrier density under the field effect; carriers form an accumulation layer of thickness t_{acc}, outside of which the carrier density acquires the flatband level. Selection of t_{acc} is rather arbitrary, with values ranging between 1 and 10 nm, strongly impacting the computed performance, while no relation between the externally applied voltage and the constant carrier density $n_{e,\mathrm{acc}}$ can be established due to ignoring the underlying electrostatic problem. In the second alternative of Fig. 20(b), a relation between the carrier density $n_{e,\mathrm{acc}}$ and the applied voltage V_a is introduced either by using an equivalent capacitor model[198,201,209] or by averaging the spatial distribution of the carrier density across the TCO thickness $n_e(x, V_a)$, calculated with the aid of a semiconductor model (for instance, the Thomas–Fermi). The carrier distribution $n_e(x, V_a)$ is then weighted over the layer thickness t_{acc}, resulting in an average carrier density $n_{e,\mathrm{av}}(V_a)$ for the accumulation layer.[192,194,195] The above two alternatives are extensively used in the TCO-modulator literature due to their computational ease. Only recently, rigorous methods for calculating the carrier density relying on semiconductor physics have been introduced, including semi-classical[187,203] or quantum descriptions.[211,212] These studies introduce in the wave

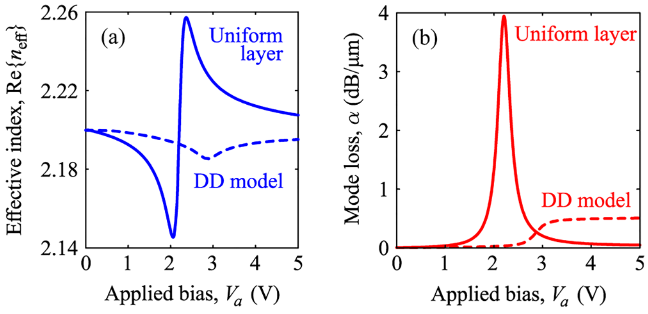

FIG. 21. Comparison between the step-change approach (uniform layer) and the drift-diffusion (DD) model for (a) the real part of the effective index and (b) the mode loss in an ITO-loaded silicon structure. Adapted with permission from G. Sinatkas and E. E. Kriezis, IEEE J. Quantum Electron. **54**, 1 (2018). Copyright 2018 IEEE.

optics the exact spatial dependence of the carrier density $n_e(x, V_a)$, as obtained by the semiconductor model of choice [Fig. 20(c)]. The spatial dependence of the carrier density in Figs. 20(a)–20(c) is translated in variations of both the real and imaginary part of the optical permittivity, as qualitatively illustrated for the real part in Figs. 20(d)–20(f), employing a carrier-dependent dispersion model.

It is very important to stress that the approaches of Figs. 20(a) and 20(b) frequently lead to overly optimistic or even unrealistic modulator performance when compared against the approach of Fig. 20(c) that is based on more rigorous semiconductor models. In Fig. 21, the step-change approach is directly compared to the more rigorous results of the drift–diffusion model for an ITO-loaded silicon structure.[187] A pronounced deviation is evidenced between the two calculations in terms of not only the intensity of the modulation effect, but also the dependence on the applied bias. Additionally, the step-change method is proven highly sensitive to the thickness of the accumulation layer, resulting in a significant overestimation of the ENZ effect as illustrated in Fig. 22(a) for the case of a hybrid plasmonic waveguide and thickness values up to 3 nm.[211] A 10-nm accumulation layer in the TCO-loaded Si-slot modulator of Ref. 200 results in a 17.4 dB/μm ER, further enhanced to 46 dB/μm in the case of a plasmonic waveguide.[197] Similarly, a $V_\pi L$ product as low as 0.004 V mm has been reported for the hybrid plasmonic waveguide in Ref. 209. Such performance metrics are at least overoptimistic and cannot be practically anticipated.

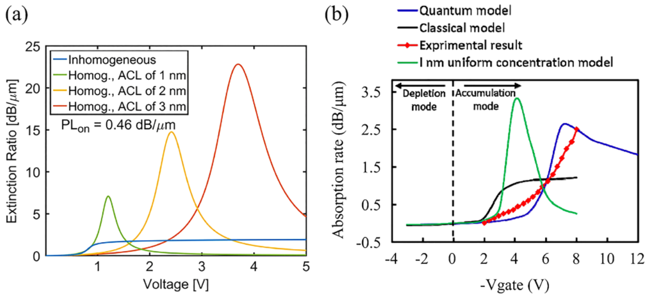

FIG. 22. (a) Comparison between the step-change approach and a more accurate inhomogeneous model (quantum hydrodynamic) for three values of the accumulation-layer thickness.[211] Adapted with permission from Koch *et al.*, IEEE Photonics J. **8**, 4800813 (2016). Copyright 2016 IEEE. (b) Collective illustration of the step-change approach, a classical (drift-diffusion) model, and a quantum model in comparison with experimental results.[212] Both figures refer to a hybrid plasmonic waveguide. Adapted with permission from Gao *et al.*, Opt. Mater. Express **8**, 2850 (2018). Copyright 2018 The Optical Society.

Figure 22(b) collectively presents a comparison among the theoretical descriptions of the step-change approach and the drift–diffusion and the quantum moment models in the case of a hybrid plasmonic waveguide.[212] All three approaches predict a different dependence for the mode loss of the guided mode as a function of the applied bias. The comparison to the included experimental results indicates that the quantum model seems closer to the measured data for this case, but a strong agreement is yet to be reported. Besides, nanometer or even subnanometer dimensions might require the consideration of quantum phenomena to accurately describe the effect. A nonlocal electron response[268] and quantum phenomena such as electron spill-out and quantum tunneling[269] can become important, as has been experimentally observed, for example, in plasmonic systems with subnanometer gaps.[270] They can be taken into account through "quantum-informed" semiclassical calculations[271] or quantum methods such as the density functional theory.

Moreover, fine structural features and thin material layers, encountered in all contemporary EO modulators, have material properties that can deviate from the typical bulk permittivity description, which should be taken into account when performing calculations. Thin film instead of bulk material properties need to be adopted where necessary. For example, in thin metallic films, material properties start deviating from the bulk values for thicknesses below 100 nm, and at values of 20 or 10 nm, they can differ significantly.[272] Similar deviations are evidenced for the optical and electrical properties of semiconductor materials, whose parameters can also depend on the deposition conditions as well as the underlying substrate. Specifically, in the case of the non-stoichiometric TCO semiconductors, controlling the oxygen concentration through the respective pressure can affect significantly their optical properties and shift the ENZ wavelength.[273] Furthermore, high-quality nm-thick TCOs can be proven particularly challenging. In Ref. 274, ultra-thin ITO films deposited on a silicon substrate have formed discontinuous islands for thicknesses below 15 nm due to becoming thinner than the critical percolation threshold. Decreasing the film thickness from 100 to 10 nm results in decreasing mobility values, attributed to the formation of a non-electrical, ∼14-nm dead layer at the ITO/Si interface due to interfacial defects.[274] Recalling the nm-thick ITO layers usually considered in theoretical works, these findings raise a significant uncertainty regarding the viability of the designed modulators. For this reason, high-quality material interfaces, with low trap and defect densities, are actively investigated, particularly for effectively integrating high-κ dielectrics into field-effect devices.[275,276]

The theoretical description of newly reported materials can also be sometimes a challenge. This is the case for graphene, whose surface conductivity is frequently a controversial topic. Although it is almost universally accepted that it is described by a Kubo formula,[277,278] introducing the physically correct parameters in the formula is not always straightforward. Among others, graphene conductivity depends on the Fermi level of the electrons and on phenomenological relaxation times of the various electron scattering mechanisms. The latter quantify graphene purity and is difficult to be *a priori* estimated, while the former strongly depends on the underlying structure upon which graphene is placed and should also be chosen carefully.[279]

In addition, the strong dispersion exhibited by some EO materials such as TCOs and graphene near their ENZ and half-photon-energy wavelength, respectively, has questioned the applicability of frequently employed methods in photonics. One of them concerns the correct calculation of the quality factor in structures based on resonant elements. The Q-factor is an important parameter of a resonant system since it measures the resonance linewidth, and, consequently, it reveals the capability of high-Q resonators to provide high ERs only with minor shifting of the resonance frequency under external stimuli. Furthermore, the correct calculation of the Q-factor in resonant devices is crucial since their design is based on that knowledge, ultimately determining the resonance shape and its peak/deep amplitude; a characteristic example is the operation of a ring resonator under critical coupling (equality of intrinsic and coupling losses, mathematically captured by the respective quality factors), resulting in a theoretically zero transmission. Q-factor can be assessed via time-domain, frequency-domain (time-harmonic), and eigenvalue simulations; correct calculations are well-established for traditional photonic platforms (LN, III–V, Si), and various computational techniques have been proposed and accurately applied.[214,280,281] Nevertheless, only recently, it has been pointed out that in contemporary systems where highly dispersive materials are involved, traditional approaches fail to give the correct Q-factor and other alternatives should be adopted, such as the careful choice of the calculation method/computational domain combination[281] or the expansion of the simulated system with additional auxiliary fields.[282] Thus, to accurately design a resonant modulator involving highly dispersive materials, an appropriate computational approach that respects their dispersive nature should be followed.

C. Electrodes and contacts

Efficient application of the RF signal highly depends on the design of the electrodes delivering the modulation signal as well as the quality of the metallic contacts. As discussed in Sec. III, two types of electrodes can be identified: traveling-wave (TW) and lumped electrodes. Electrically long modulators (e.g., LN-based MZMs) employ in principle TW electrodes, while short modulating units (e.g., based on TCOs) usually opt for lumped ones. A rough length criterion could be the one tenth of the free-space RF wavelength divided by the RF effective index. Both schemes aim the efficient modulation of the guided wave at minimum cost and maximum speed, with each one exhibiting, though, unique design challenges.

Traveling-wave electrodes require the often challenging matching between the phase velocity of the RF signal and the group velocity of the optical wave, while ensuring low losses for the propagating RF signal. Lumped electrodes are in principle much simpler, but they should maintain their lumped operation even at high frequencies. This could limit the modulation efficiency in the case of weaker modulation effects, which require in principle longer interaction lengths. For example, adequately long modulating elements are necessary in order to achieve high ER values in the case of EAMs or the required phase shift for full extinction in an MZM. Longer phase shifters also allow for maintaining low drive voltage requirements. On the other hand, increased interaction lengths raise insertion losses, reducing the overall efficiency of the modulator as well as its optical modulation amplitude. Thus, the optimal interaction length often results as a compromise among multiple performance criteria.[15]

In both TW and lumped electrodes, the use of standard 50-Ω systems can also be proven problematic. As described in Sec. III, impedance matching is generally challenging for InP-based MZMs due to the large capacitance per unit length of the p–i–n waveguide structure. Lumped-electrode modulators are also challenged from the in-series 50-Ω impedance. The latter adds to the total resistance of the modulator, increasing the intrinsic RC constant, reducing, thus, the maximum achievable EO bandwidth.[15] Moreover, the small impedance values of lumped-electrode modulators can also hinder the efficient delivery of the RF signal. Improved matching can be achieved through TWE schemes, which transform the impedance to a higher input value. Alternatively, the use of low output impedance lumped-element drivers is suggested.

Electrodes should be placed in close proximity to the modulating area in order to eliminate the series resistance from the contact to the core of the modulator as well as parasitic-capacitance effects, both of which hinder the efficient delivery of the modulation signal, raise the energy consumption, and limit the modulation speed. At the same time, however, metallic as well as highly doped semiconductor parts should lie sufficiently far from the guided optical wave to avoid excessive optical losses; this further extends to the contacts themselves. Techniques such as gradual doping[117] are often employed as a compromise between reducing series resistance and maintaining low ILs.

Contacts themselves can also impose significant limitations to the overall modulation performance. Even though the ideal ohmic representation is commonly considered in energy-consumption and bandwidth calculations, this approach is elementary and can only provide an estimate for the upper performance limit. In practice, metal–semiconductor interfaces often form Schottky junctions, further raising the series resistance; thus, metals that exhibit a zero or even a negative Schottky barrier Φ_B with the underlying semiconductors are favorable. For example, aluminum or copper contacts are used with Si,[114,117,126,168,170] gold with TCOs,[204,221] and platinum or nickel with InGaAsP.[283,284] Nevertheless, the series resistance reduction is not easily achievable, and sometimes stacked metals are used (e.g., Ti/Pt/Au,[236] Au/Cr,[174,229] Ti/Au,[49,219] Au/Ge/Ni,[100] etc.), complicating the fabrication process. On the contrary, metal–insulator interfaces are less challenging, with gold and aluminum contacts being popular among modulators based on the Pockels effect.[44,54,157,158] The complexity of electrical contacts usually discourages their rigorous consideration in theoretical calculations and is, therefore, ignored, resulting in more generous estimates for the energy consumption and bandwidth metrics.

D. Energy consumption

One of the key performance metrics of a modulator is its energy efficiency, usually expressed through the energy required for the transmission of a single bit of information. Its rigorous theoretical calculation is of utmost importance since it provides an estimate for the lowest anticipated consumption in practice. Landmark works in the field of EO modulation have become points of reference for understanding the origins of energy dissipation.[16] However, newly reported modulators often overlook such a precise (and sometimes cumbersome) calculation or perform rough estimates, which regularly result in record-low but unrealistic values. Here, we review key considerations for calculating the energy-per-bit performance for the indicative case of lumped-electrode, field-effect OOK modulators, which identify with some of the most promising designs reviewed in Sec. III. Erroneous practices encountered in the literature are also highlighted. In the examined cases, the electric field is introduced either through a reversely biased p–i–n junction or a MOS-like structure. Note that in the case of TWE designs, a transmission-line-theory description should be employed.[67,120,285]

The calculation of the energy-per-bit value E_b is usually limited to the energy $E_{b,\mathrm{el}}$ required for electrically charging/discharging the modulator. However, an equally important contribution originates from the actual optical energy required at the transmitter as well as the energy dissipated due to optical-loss mechanisms. Both contributions are collectively included in a term $E_{b,\mathrm{opt}}$. The total energy-per-bit consumption is then expressed as $E_b = E_{b,\mathrm{el}} + E_{b,\mathrm{opt}}$.

Starting with the calculation of $E_{b,\mathrm{el}}$, it originates from the dissipation in the resistive parts of the electrical junction due to the current flow during charging/discharging. Among the four possible state transitions, "0–0," "0–1," "1–0," and "1–1," only one complete charge/discharge cycle ("0–1," "1–0") is formed. The average dissipation per bit, thus, equals $E_{b,\mathrm{el}} = 1/4 \times E_{\mathrm{el}}$, where E_{el} is the total energy dissipated during a full charge/discharge cycle. The factor of one quarter is of statistical origin and equals the probability of a complete charge/discharge cycle in an equiprobable modulating signal.

Assuming the worst case scenario and the lack of an external recovery circuit, the total electrical dissipation E_{el} equals twice the stored energy in the structure, $E_{\mathrm{el}} = 2 \times E_{\mathrm{stored}}$.[16] The stored energy is usually calculated using the simple, ideal parallel-plate capacitor model, $E_{\mathrm{stored}} = C_g V_a^2/2$, with $C_g = Q/V_a$ denoting the *geometric* capacitance of the junction, V_a the applied bias, and Q the total charge. For simplicity, the junction is considered to be driven between the unbiased state and a maximum value V_a in the absence of any static bias.

However, revisiting the definition for the stored energy, it holds that

$$E_{\mathrm{stored}} = \int_Q V\,\mathrm{d}q, \tag{1}$$

where $Q = \int_{\Omega_1} \rho\,\mathrm{d}\Omega$ is the total charge in the structure, with ρ being the space-charge density in one plate of the capacitor (volume Ω_1) as long as the difference in the electrostatic potential between the two capacitor contacts is correspondingly defined as $V = \phi_{t,1} - \phi_{t,2}$. From Eq. (1), it is concluded that the ideal parallel-plate capacitor model presumes a junction of constant capacity C_g so that $Q = C_g V$. This is the case, however, for a capacitor whose plates have a high density of states (DOS) and are, thus, considered as equipotential volumes (e.g., metals). Practical junctions in photonic components are most usually of semiconductor nature, with the electrostatic potential decreasing exponentially toward the interior of the semiconductor under the application of an external electric field until reaching its flatband value (screening effect). The actual potential drop in the semiconductor, $V_{\mathrm{semi}} = \phi_t - \phi_s$ (ϕ_t is the electrostatic potential at the contact and ϕ_s at the semiconductor–insulator interface), and the developed charged Q are interrelated quantities, allowing for defining a bias-dependent semiconductor capacitance $C_{\mathrm{semi}}(V_{\mathrm{semi}}) = \partial Q/\partial V_{\mathrm{semi}}$, which contributes in series to the geometric capacitance. Expressing the total capacitance as $C_{\mathrm{tot}}^{-1} = C_g^{-1} + \sum_i C_{\mathrm{semi},i}^{-1}$, Eq. (1) is rewritten as

$$E_{\mathrm{stored}} = \int_0^{V_a} C_{\mathrm{tot}}(V)\,V\,\mathrm{d}V. \tag{2}$$

For the calculation of the electrostatic potential and the space-charge density, a rigorous solution of the underlying semiconductor problem is required. A fully equivalent, field-based expression is derived in Ref. 286,

$$E_{\mathrm{stored}} = \int_{\Omega-\Omega_{\mathrm{semi}}} \frac{1}{2}\,\mathbf{E}\cdot\mathbf{D}\,\mathrm{d}\Omega - \oint_{S_{\mathrm{semi}}} (\phi_s - \phi_t)\,\mathbf{D}\cdot\,\mathrm{d}\mathbf{S}, \tag{3}$$

with $\mathbf{E}$ ($\mathbf{D}$) denoting the electric field (electric displacement), ϕ_s (ϕ_t) the surface potential at the semiconductor–insulator (contact–semiconductor) interface, and Ω_{semi} (S_{semi}) the volume (external surface) of the semiconductor parts of the junction. Consequently, apart from the well-known and usually solely considered first term, there is an additional contribution to the total energy, which stems from the formation of non-neutral, space-charge regions in the semiconductor materials. It results from their lower DOS, in contrast to high DOS and equipotential metals, where it vanishes ($\phi_s \equiv \phi_t$). Its effect becomes even more pronounced in junctions comprising low-dimensional materials such as graphene. There, the injected carriers occupy increasingly higher energy levels as a result of the Pauli blocking, leading to an increase in the internal chemical potential μ_c of graphene. The latter is expressed as the difference in the total electrostatic potential, $\mu_c = e(\phi_s - \phi_t)$.[214] The new term in Eq. (3) reduces to

$$-\oint_{S_{\mathrm{semi}}} (\phi_s - \phi_t)\,\mathbf{D}\cdot\,\mathrm{d}\mathbf{S} \rightarrow -\frac{\mu_c}{e} Q_s, \tag{4}$$

where $Q_s = -e\oint n_s\,\mathrm{d}S$ is the surface charge density on graphene and n_s the net carrier density between electrons and holes, related to μ_c through Fermi–Dirac statistics. The stored energy in graphene can be equivalently represented by a *quantum capacitance* $C_q = \partial Q_s/\partial V_{\mathrm{ch}}$, in series to the geometric capacitance C_g of the structure, where $V_{\mathrm{ch}} = \mu_c/e$ is defined as a local channel electrostatic potential.[287] The effect of C_q is frequently overlooked in graphene-comprising junctions, underestimating their energy requirements as well.

After having calculated the stored energy at steady-state conditions through Eqs. (1)–(3), the total dissipated energy due to charging/discharging E_{el} equals twice this value. Opting for a time-dependent solution scheme, this energy could be alternatively calculated by integrating the absolute value of the power $W = VI$ provided by the source (or returned to it) during charging (discharging). No external recovery circuit is employed, and thus, the energy returned to the source is dissipated, generating heat.[16] Letting T being the time period of a complete charging/discharging cycle, the total electrical dissipation can be expressed as

$$E_{\mathrm{el}} = \int_0^T |V(t)I(t)|\,\mathrm{d}t, \tag{5}$$

where $V(t) = \phi_{t,1}(t) - \phi_{t,2}(t)$ is the time-dependent electrostatic potential difference between the contacts of the junction and $I(t) = \partial Q/\partial t$ is the total current flow. Equation (5) should result in twice the stored energy at steady-state conditions [Eqs. (1)–(3)], provided that the bit period exceeds the minimum required time T for a complete charging/discharging cycle of the structure. Equivalently, the power W provided by the source (or returned to it) can be calculated as $W = \mathrm{d}E_{\mathrm{stored}}(t)/\mathrm{d}t$, with the stored energy E_{stored} being now expressed as a function of time using any of Eqs. (1)–(3). Integrating the absolute value of W over the bit period T, one should arrive again at E_{el}. A point of attention when switching from a steady-state to temporal calculations is the generic dependency of capacitance on the frequency of the applied signal, with its high-frequency value being reduced compared to its low-frequency one. This effect manifests predominately under inversion conditions and originates from the inability of minority carriers to respond to increasingly alternating fields.

For reasons of comprehensiveness, we take a step further toward a brief discussion of the key points for calculating the optical energy per bit $E_{b,\mathrm{opt}}$ required at the transmitter, with a detailed analysis presented in Ref. 16. Employing an EAM as a case study, let $E_{\mathrm{in,o}}$ be the total optical energy introduced to the modulator during the period of a symbol. The dissipated energy can be distinguished in the energy absorbed E_{abs} but also in the energy E_{pc} associated with the photocurrent flow as a result of the generation of free carriers and their sweeping in the reverse-biased diode structures. Accepting the generation of one electron–hole pair for each photon absorbed (perfect quantum efficiency), the total generated charge equals $Q_{\mathrm{pc}} = eE_{\mathrm{abs}}/\hbar\omega$, collected under a reverse (or small forward) bias V. For each modulation state, the dissipated power can be expressed as

$$E_{\mathrm{diss}} = E_{\mathrm{abs}} + E_{\mathrm{pc}} = E_{\mathrm{abs}} + \frac{eE_{\mathrm{abs}}}{\hbar\omega}|V|, \tag{6}$$

where V is the reverse bias applied to the diode. The transmitted optical energy equals

$$E_{\mathrm{trans}} = E_{\mathrm{in,o}} - E_{\mathrm{abs}}. \tag{7}$$

Considering the case of an OOK modulator, the energy $E_{b,\mathrm{opt}}$ can now be expressed as the average energy dissipated and transmitted between the low and high energy states,

$$E_{b,\mathrm{opt}} = \frac{1}{2}\left[(E_{\mathrm{diss}} + E_{\mathrm{trans}})_L + (E_{\mathrm{diss}} + E_{\mathrm{trans}})_H\right]. \tag{8}$$

Substituting Eqs. (6) and (7) in Eq. (8),

$$E_{b,\mathrm{opt}} = \frac{1}{2}\left(2E_{\mathrm{in,o}} + \frac{eE_{\mathrm{abs},L}}{\hbar\omega}|V_L| + \frac{eE_{\mathrm{abs},H}}{\hbar\omega}|V_H|\right). \tag{9}$$

Introducing the absorption coefficient η so that $E_{\mathrm{abs}} = \eta E_{\mathrm{in,o}}$ and the photocurrent dissipation multiplier $\mu = e|V|/\hbar\omega$, Eq. (9) can be expressed as

$$E_{b,\mathrm{opt}} = \frac{1}{2}\left(2 + \eta_L\mu_L + \eta_H\mu_H\right)E_{\mathrm{in,o}}. \tag{10}$$

The final step consists of determining the required input optical energy $E_{\mathrm{in,o}}$ at the transmitter. Its value should ensure that the minimum required optical energy per bit $E_{b,\mathrm{rec}}$ arrives at the receiver. Since the detection performance depends on the energy difference between the two logic states, $E_{b,\mathrm{rec}}$ should be expressed as a function of the useful energy launched at the transmitter. In the case of an ideal modulator ($\eta_H = 0$, $\eta_L = 1$), the average useful launched energy per bit equals $E_{b,\mathrm{trans}} = E_{\mathrm{in,o}}/2$. However, in practical modulators, the energy difference is shrunk, and $E_{b,\mathrm{trans}}$ reduces to

$$E_{b,\mathrm{trans}} = \frac{1}{2}\left(\eta_L - \eta_H\right)E_{\mathrm{in,o}}. \tag{11}$$

Using Eqs. (10) and (11), the average optical energy per bit is expressed as

$$E_{b,\mathrm{opt}} = \frac{2 + \eta_L\mu_L + \eta_H\mu_H}{\eta_L - \eta_H}E_{b,\mathrm{trans}}. \tag{12}$$

Considering the best case scenario of a zero-loss transmission, $E_{b,\mathrm{trans}}$ will equal the required energy $E_{b,\mathrm{rec}}$ at the receiver, which is determined by the specifications of the photodetector. The total energy-per-bit value is finally calculated as

$$E_b = E_{b,\mathrm{el}} + E_{b,\mathrm{opt}} = \frac{1}{4}E_{\mathrm{el}} + E_{b,\mathrm{opt}} = \frac{1}{2}E_{\mathrm{stored}} + E_{b,\mathrm{opt}}. \tag{13}$$

Quoting the calculations for the InGaAsP-embedded photonic-crystal EAM in Ref. 77 for a scale estimate, a total of $E_b = 4.3\,\mathrm{fJ/bit}$ is calculated for the 105-μm design, from which $E_{b,\mathrm{el}} = 1.6\,\mathrm{fJ/bit}$ and $E_{b,\mathrm{opt}} = 2.7\,\mathrm{fJ/bit}$ (0.2 fJ/bit attributed to photocurrent dissipation), when a $E_{b,\mathrm{rec}} = 0.5\,\mathrm{fJ/bit}$ specification is defined at the receiver. It is evidenced, thus, that the required optical energy at the modulator can have a considerable contribution to its total energy consumption despite being frequently disregarded. Given also the low wall-plug efficiency of NIR semiconductor lasers (the power ratio of the optical output to the required electrical input), currently around 15%,[288] it can be argued that the optical term $E_{\mathrm{in,o}}$ in Eq. (9) has to be suitably weighted to reflect the increased cost of losing optical energy compared to a direct loss in an electrical one as quantified by $E_{b,\mathrm{el}}$ and the last two photocurrent terms in Eq. (9).

In practice, the share of the required optical energy at the modulator in its total energy consumption is further increased when additional sources of loss are considered such as coupling losses between the laser and/or the input/output waveguides and the modulator, free-carrier absorption losses due to the overlap of the guided mode with doped semiconductor regions, etc. These additional optical losses result in a raise of $E_{\mathrm{in,o}}$ for maintaining the same $E_{b,\mathrm{rec}}$ specification at the receiver. For the previous example of PhC-EAM,[77] considering an additional on-chip IL of 3 dB doubles the required $E_{\mathrm{in,o}}$, resulting in a twofold increase in $E_{b,\mathrm{opt}}$ based on Eqs. (11) and (12), raising the total E_b to 7 fJ/bit. However, given the low efficiency of the respective laser source, this value could be in reality quite higher.[15] It is important, therefore, to account for all major sources of dissipation in the calculation of the energy consumption so as to perform a fair comparison among markedly different modulation technologies (e.g., Pockels effect and QCSE) and physical systems (photonic, plasmonic), which are characterized by quite different levels of optical loss. Additional contributions to the total energy consumption, and specifically to the $E_{b,\mathrm{el}}$ term, could include the energy dissipated for temperature control either for tuning or cooling operations. The latter can be avoided in the case of robust and athermal modulators, which therefore appear promising for future ultra-low energy applications.

The very ambitious goal of 10 fJ/bit or even lower has been set for the total energy consumption of future optical interconnects with lengths from ~1 to ~10 cm.[13] Therefore, the consumption of the respective modulators should be limited to 1 fJ/bit or below. Strong indications for such a low consumption have been evidenced in the case of, e.g., a modulator based on a silicon-photonic resonator,[120] an Si-slot SOH MZM,[169] a plasmonic slot waveguide filled with an organic EO material,[285] a double-layer graphene silicon waveguide,[228] and an InGaAsP-embedded photonic-crystal waveguide.[289] In the latter case, a record-low consumption of 42 aJ/bit is estimated. All these modulators demonstrate bandwidth values at least in the order of tens of GHz. However, such an assortment of literature works is not always directly comparable since, in some cases, the energy-per-bit value is theoretically calculated rather than actually measured based on simple models that neglect parasitic effects and can significantly underestimate the energy consumption. In addition, the majority of works considers almost exclusively the dissipation due to the charging/discharging operation, disregarding the occasionally high ILs. Thus, a rough comparison can often be deceptive. A representative example is plasmonic modulators, which report much lower energy-per-bit values compared to purely photonic platforms thanks to their considerably smaller footprint, which reduces the charging/discharging dissipation, failing, however, to account for their considerably higher optical losses. In conclusion, promising future directions toward energy efficient modulators should include the use of a strong EO effect, such as the Pockels effect in polymeric materials of an extraordinary EO coefficient or the QCSE in MQW structures, as well as an efficient compromise between strong optical confinement and low optical losses, using, for example, the silicon-slot or photonic-crystal platforms.

E. Reliability

The practical success of an electro-optic modulator platform also depends on reliability issues given that devices in lightwave communication systems are required to operate reliably for at least 20 years in field conditions. Very different issues of reliability apply to different types of modulators. For instance, InP modulators may suffer from leakage current problems or phase changes, quantified in hard-aging conditions.[91] Lithium-niobate modulators may suffer from mechanical strain attributed to the electrodes (which is thermally dependent), pyroelectric charges that influence stability by shifting the operation point, and DC bias drifts related to dielectric relaxation processes.[290] Electro-optic polymer modulators may suffer from stability issues, especially when operation at elevated temperatures is required; significant improvement is attained by employing EO polymers with high glass-transition temperatures.[158] Accelerated-aging tests, including high-temperature storage or temperature-cycling, are mainly conducted for assessing the reliability levels of modulators made of III–V semiconductors, silicon, lithium niobate, or electro-optic polymers. Far less details on long-term stability or reliability are currently available for modulators based on 2D materials or transparent conducting oxides.

V. DIRECTLY MODULATED LASERS

Apart from external modulation schemes, directly modulated lasers (DMLs) are also commercially employed, especially for short-distance optical fiber communications. Recent developments in DMLs have highlighted their suitability for low-consumption and high-capacity optical interconnects as well.[291] Next, key elements of direct modulation are discussed together with indicative metrics of their state-of-the-art modulation performance.

First demonstrated in the 1970s,[292] DMLs use variations of the driving electrical current to modulate the intensity of the emitted light. Changes in the carrier and photon density inside the optical cavity result in wavelength and power oscillation effects, respectively, which degrade the transmission characteristics (adiabatic chirp). In contrast, external electro-absorption modulators exhibit only transient chirping, manifesting during the "0–1" bit transitions, which results in phase changes for the transmitted wave.[293] As a result, external modulators are preferable for high-speed, long-haul transmission distances at the low-loss wavelength of 1.55 μm. DMLs have been rather limited to 10- and 100-Gbps transmissions up to 100 km at the zero-dispersion wavelength of 1.3 μm.

A direct comparison with external modulators would only be possible in the context of optical transceivers, which means that in the case of external modulators, one should take into account the performance metrics of the required laser source as well. In general, DMLs demonstrate higher output power, proportional to their bias current, and they are considered more cost effective. Their small footprint renders them also attractive for optical interconnects. However, decreasing the transmission distance also requires a reduction in their operating energy (equivalently their bias current) to values that could compete with those of their electrical counterparts. The bias current can be reduced by decreasing the active laser volume, maintaining this way the current density above the lasing threshold. The active volume can be decreased using structures of higher reflectivity that increase the optical confinement, ensuring additionally an adequately high quality factor despite the reduction in the cavity volume. Moreover, a larger differential gain (the rate of the increase in gain with respect to the injected carriers) is also beneficial for the modulation efficiency and reduces the bias current. The differential gain depends on the underlying material platform, usually comprised of quantum-confined III–V-semiconductor structures, and it can be increased by enhancing the quantum confinement of carriers, the optical confinement, and the optical feedback from the reflector, as well as adjusting the detuning between the lasing wavelength and the gain peak wavelength.

The modulation bandwidth of DMLs is intrinsically limited by the relaxation oscillation frequency f_r, the damping effect, and the RC constant. The parameter f_r refers to the frequency of the output-power oscillations until the laser stabilizes, and it should be as high as possible. The damping effect suppresses the relaxation oscillation, mainly due to a nonlinear gain effect, and it should be weak enough to avoid over-damping and a subsequent decrease in the achievable bandwidth. Frequency f_r increases with decreasing the active volume as well as increasing the differential gain and injection current. The latter implies a trade-off relation between energy consumption and bandwidth for the case of DMLs. Major factors that determine the damping effect are the nonlinear properties of the gain material, the differential gain, and the photon lifetime.[294] Consequently, despite their simple modulation concept, low-energy and high-bandwidth DMLs constitute a challenging engineering problem.

DMLs can be in-plane structures, such as distributed-feedback (DFB) and distributed reflector (DR) lasers, or vertical-cavity surface-emitting lasers (VCSELs). The former use either a ridge waveguide or a buried mesa heterostructure and exhibit active lengths from 100 to 200 μm and modulation rates up to 56 Gbps (NRZ-OOK).[295,296] InGaAlAs-based MQWs are usually employed for the active region due to their large conduction band offset, which allows for stronger quantum confinement and semi-cooled or even uncooled operation, which reduces the energy cost. A consumption in the order of a few pJ/bit is typically reported for DMLs. However, this value cannot be safely compared with the frequently reported fJ/bit values of external modulators since the latter also require a laser source, which is usually very inefficient.

Short-wavelength (850–1060 nm) multi-mode VCSELs are based on the GaAs material system, which provides the opportunity for highly reflective GaAs/AlAs distributed Bragg reflectors (DBRs). GaAs-based VCSELs are characterized by low fabrication cost, a bandwidth exceeding 30 GHz, and an energy consumption of less than 100 fJ/bit due to a ten times smaller cavity volume compared to in-plane lasers.[297–299] They are commercially used for short-reach (<300 m) intra-datacenter optical links and supercomputers, limited by the modal dispersion. Transmission distances above 500 m can be achieved by few- or single-mode VCSELs, which, however, have limited output power and require more elaborate optical alignment.[300] Long-wavelength VCSELs (1.3 or 1.55 μm) are based on the InP material system and target longer transmission applications. However, high-reflectivity InP-based DBRs are challenging, and hybrid dielectric–semiconductor mirrors have been proposed instead. The reduced conduction band offset in InP-based MQWs negatively affects operation at high temperatures, while the precise control of the lasing wavelength is challenging due to fabrication imperfections of the wavelength-scale cavity length, hindering their use in wavelength-division-multiplexing (WDM) networks. The use of high-contrast gratings (HCGs) has been proposed as a possible solution.[301] InP-based VCSELs have demonstrated a bandwidth of 22 GHz, allowing for rates up to 50 Gbps (NRZ-OOK) for an energy consumption of 130 fJ/bit.[302] Current research on InP-based VCSELs targets the reduction of their active volume and the continuous tuning of their lasing wavelength.

Toward reducing the active laser volume, the photonic-crystal (PhC) platform provides significantly higher reflectivity values compared to the semiconductor DBRs used in VCSELs. PhC lasers demonstrate high-Q, ultra-small cavities together with the opportunity for a lateral current injection scheme.[303] Heating issues are addressed by embedding the active region in an InP-based PhC line-defect waveguide. This kind of laser is referred to as a λ-scale embedded active-region PhC (LEAP) laser. A 10-Gbps rate with consumption as low as 4.4 fJ/bit has been demonstrated for a LEAP laser with a 2.5-μm-long and 0.3-μm-wide active region.[304] Despite the decrease in their operating energy, lasers with reduced active volumes usually provide low output optical powers that are often insufficient for typical detection schemes. Reducing optical losses through the monolithic integration of lasers with photodetectors as well as the minimum receivable optical power at the photodetector could ease the requirement for higher optical power. For this reason, photodetectors with capacitances in the range of tens of attofarads are targeted through their close integration with electronics.[13,305]

In future, the integration of DMLs with silicon wafers can reduce significantly the fabrication costs. This can be achieved by methods similar to those described for the externally modulated lasers in Sec. III B. Differences in lattice constants and thermal expansion coefficients as well as the current injection scheme (vertical or lateral) should be considered for selecting the optimal integration method. Membrane DMLs with a rate of 25 Gbps (NRZ-OOK) and an ∼100 fJ/bit operation have already been demonstrated.[306]

Overall, DMLs exhibit bandwidth values that typically do not exceed 35 GHz,[307] with commonly reported rates up to ∼56 Gbps (NRZ-OOK).[296] The use of advanced modulation formats (PAM, QAM, DMT), digital-signal-processing techniques as well as optical domain effects (e.g., optical feedback) can increase their modulation rate beyond 200 Gbps per lane.[24] In Ref. 308, a membrane DR laser on a silicon carbide substrate with a 50-μm-long active region exhibits a 60-GHz intrinsic bandwidth, enhanced to 108-GHz using the effect of optical feedback. The DML demonstrated a rate of 256 Gbps (4-PAM) with an energy consumption of 475 fJ/bit.

Spin-lasers have also attracted attention as an alternative means of overcoming the bandwidth bottleneck. By injecting spin-polarized carriers into conventional VCSELs, spin-lasers modulate the polarization of the output light instead of its intensity, exploiting the coupling between carrier spin and light polarization. The dynamics of polarization modulation has proven much faster compared to intensity modulation,[309] allowing for a bandwidth exceeding 240 GHz at room temperature, which is nearly an order of magnitude greater than the respective of conventional DMLs.[310] In addition, the bandwidth is decoupled from the requirement for strong pumping, which dictates the performance of conventional VCSELs and results in increased heating and low efficiency. Spin-lasers can demonstrate their highest bit rates just above their lasing threshold, promising ultra-low power optical communication.

VI. FUTURE OUTLOOK

In this section, the future prospects of the different EO materials employed in external modulators are discussed.

A. Lithium niobate

The recent rapid developments in thin film lithium-niobate technology has created new prospects and revolutionized the LN modulator landscape. Despite the progress, $V_\pi L$ values below 1 V cm are still very challenging (excluding plasmonic devices). In 2020, the highest reported value for a uniform LN thin film loaded with a silicon-nitride core was 2.1 V cm ($V_\pi = 0.875$ V, length 2.4 cm).[311] Given the fixed r_{33} value, it is hard to anticipate spectacular improvements in this performance metric. However, further improvement is anticipated in integration techniques of LN thin films in silicon platforms, with high foundry compatibility achieved when the lithium-niobate film is bonded on the top of the silicon chip in an additional back-end step at room temperature.[312] Demonstrations of IQ modulators operating at higher modulation formats in LN thin film technology are very limited and only very recently emerged. In 2020, Ref. 253 reported 110 GBd QPSK (220 Gbps) and 80 GBd 16-QAM (320 Gbps) in a monolithic device based on an etched LN thin film. In terms of other metrics such as the bandwidth-voltage ratio (BW/V_π), contemporary LN modulators can deliver values up to 25 GHz/V, which, however, fall behind those achievable with modulators based on electro-optic polymers.

With further reasonable improvements in various aspects, including the RF electrodes, bit rates above 1.2 Tbps are anticipated, for instance, raising the symbol rates above 200 GBd and using the 64-QAM format. Monolithic lithium-niobate modulators (i.e., those based on etched LN thin films) will probably substitute in the near future the widespread conventional LN modulators. They outperform their conventional counterparts in every metric while being aligned with current requirements of reduced footprint and are able to meet the demands of emerging applications. Hybrid LN modulators capitalizing on the silicon platform are a technology of a medium term that is expected to further mature in the coming years, being a strong competitor to the purely silicon-based modulators that exploit carrier effects. Compatibility to the CMOS process is a prerequisite, and related issues have to be resolved before extensive deployment can take place.

B. III–V semiconductors

Since the first demonstrations of GaAs- and InP-based EAMs in the 1960s and 1980s, respectively, III–V-based modulators have become the conventional choice for long-haul optical communications at rates over 2.5 Gbps (OOK) due to the low or even negative chirp values. Today, state-of-the-art designs have experimentally demonstrated 100-GHz bandwidth values[82] as well as bit rates up to 200 Gbps and beyond.[24] The reported 400-Gbps single-lane rate[92] is very encouraging for next-generation 1.6-Tbps transmissions. Such rates will offer a significant reduction in the complexity of transmitters, which could be simply configured in a 4 × 400-Gbps architecture, as well as simpler detection configurations. Current challenges for III–V-based modulators include their uncooled operation for reducing their energy consumption as well as a decrease in their driving voltages to CMOS-compatible levels (<1 V) to avoid the need for amplification.[79]

The intrinsic capability of III–V photonics to support the full spectrum of functionalities (lasers, amplifiers, modulators, detectors, routers, etc.) on-chip, with the aid also of high-speed III–V electronics, constitutes a competitive technological advantage. Intense research is carried out toward combining the benefits of III–V photonics with the low-cost and large-scale CMOS technology of silicon electronics and photonics. InP membranes bonded on SOI wafers appear as a promising means for adding photonic functions to silicon electronics.[313] The interconnection between the III–V photonic layer and the underlying CMOS-chip is achieved using vias through the BCB bonding layer, which provides reduced series resistances and thermal isolation. The InP-Membrane-on-Silicon (IMOS) technique does not interfere with the fabrication processes of electronic circuits and allows for devices of reduced footprint and energy consumption. Hybrid III–V/Si photonics consisting of a highly functional III–V layer bonded on the top of a passive silicon-photonic circuitry have also attracted attention.[96] The outlook of III–V-based modulators appears also promising for future integrated quantum-photonic circuits, where direct-bandgap semiconductors, and particularly GaAs, are employed.[314]

C. Silicon

Pure silicon modulators have undergone an immense evolution in the past 15 years since the first GHz realization.[104] Transmission rates as high as 50 or 60 Gbps with a few dB dynamic ER are typically reported experimentally. Having reached the aforementioned speed limit, which is practically the upper achievable with the plasma dispersion effect due to the limited carrier mobility in Si,[315] interest has shifted toward more advanced modulation formats to further extend the data transmission rates; data rates as high as 400 Gbps have been demonstrated despite the physically achievable upper limit of ∼50 GBd. Transmission rates up to 1 Tbps are set as the next milestone of the platform. The maturity of the silicon platform is reflected in the current research topics, which mostly rotate around more commercial issues such as external bias minimization, power consumption limitation, footprint reduction, efficient monolithic integration with other passive or active components, packaging issues, etc. More fundamental concepts (e.g., interior modulator designs, modulation speed limits, etc.) are widely accepted as being well understood and conceptually resolved.

Interest is also shifting toward hybrid platforms, which can bridge the advantages of silicon with other materials. This topic is extensively covered in Sec. III and is expected to gather the scientific and engineering effort in the foreseeable future. Compared with the pure silicon-on-insulator, hybrid platforms constitute a relatively new alternative and need significant improvement to reach maturity. However, given the promising prospects of hybrid integration, as already highlighted for the Si-LN, III–V-on-Si, and Si-Ge platforms, it constitutes one of the important scientific challenges for coming years.

D. Electro-optic polymers

EO-polymer modulators evolved during a 25-year period and gradually reached impressive performance levels. Sub-1-mm length, sub-1-V half-wave voltage (V_π), bandwidth exceeding 100 GHz, and loss in the range of 1 dB per phase-shifter can all be met in silicon-based implementations. Such modulators can be directly driven by a CMOS output, avoiding a driver amplifier that heavily contributes to the energy consumption, and making it possible to access the fJ/bit level. The possibilities for radically improved waveguide designs are limited, and the slot waveguide appears as the optimal choice, featuring excellent optical confinement, almost a perfect overlap between the optical and RF modes, convenient EO material poling by the RF lines, easy infilling, small footprint, and all advantages associated with the silicon platform. Plasmonic slot waveguides provide a successful route to device miniaturization and ultrahigh BW; they are accompanied, however, by the well-anticipated increase in losses, and the loss-efficiency product ($V_\pi L a_{\mathrm{dB}}$) deteriorates by a factor of at least 10 with respect to photonic counterparts. It is hard to envisage any other waveguide that can encompass in the same degree the above set of features. Thus, future advancements are mainly anticipated from improvements in EO materials, with progress in device engineering contributing to a lesser degree.

Advances in EO materials include self-assembled multichromophore dendrimers with maximized acentric order and minimized dipole–dipole interaction of the chromophores at high loading density, with the $n^3 r_{33}$ figure-of-merit outperforming traditional guest–host systems and reaching values as high as 2400 pm/V.[316] Although electro-optic activities in the range of 500–600 pm/V are possible in thick films,[317] in restricted geometries (such as in slot waveguides), the EO activity drops to values below 400 pm/V; this suggests that specific surface modification techniques are welcomed for shrinking dimensions. Further improvement in EO polymers will lead to devices that can efficiently and stably operate at elevated temperatures (as high as 100°C), which is beneficial for installation in harsh environments or translates into reduced energy consumption for the cooling systems and lowers running costs in datacenters. Such devices were very recently demonstrated in Ref. 255, where a high glass-transition temperature is essential for the thermal reliability and long-term operation; T_g values exceeding 200 °C have already been reported.[318] Poling in sub-100 nm slots is a challenging process, and improvements are also expected, as they will allow for a higher acentric order in high number density materials. In view of all of the above, values of $V_\pi L \sim 0.1$ V mm are envisaged in the silicon platform with the corresponding metric dropping to ∼0.01 V mm for EO-polymer plasmonic modulators.

E. Transparent conducting oxides

During the last decade, the renewed interest in TCOs for NIR modulation applications has demonstrated modulators of record-low interaction lengths. In-line modulators with ER ~ 1.63 dB/μm[216] and MZMs with $V_\pi L$ products in the order of 0.095 V mm are among the most impressive experimentally verified performances. However, TCO-based modulators have exhibited high ILs, driving voltages from a few to tens of volts, and have yet to demonstrate the theoretically expected bandwidth values (>100 GHz), being limited to a few GHz.

A bandwidth increase would require a reduction in the total RC constant by improving the quality of electrical contacts, optimizing the semiconductor doping profiles, as well as employing TCO films with high electron-mobility values. The latter has stimulated research toward nm-thick TCO films with improved electrical and optical properties, which usually differ from the respective bulk ones.[274,319] Alternative compounds such as dysprosium-doped CdO (cadmium oxide) have also attracted attention for the same reason.[221,320,321] High-quality TCO films could also reduce optical losses due to weaker damping of the oscillating free carriers. The use of silicon-photonic physical systems, instead of plasmonic or even hybrid plasmonic ones,[203] could also mitigate ILs in TCO-based components, especially in phase-shifting units, since the lack of a predominately electro-refractive regime for TCOs inevitably results in high losses.[187] Currently, loss-balancing mechanisms are employed to avoid ER-degradation in MZMs[205] and ensure balanced constellations, free from any residual intensity-modulation effect.[187] Furthermore, the required driving voltages could reach CMOS-compatible levels by employing nm-thick dielectrics with high dielectric constant as well as breakdown voltage.[322] Such dielectrics would also be beneficial for a reduction of the energy consumption, which is currently estimated in the order of pJ/bit or below. In the years to follow, a convergence between theoretical calculations and experimental measurements will provide insight into the underlying physical effects, and it will allow for alleviating the weaknesses of the demonstrated TCO-based modulators.

F. Two-dimensional materials

Modulators based on 2D materials are expected to remain in the research spotlight due to their high potential (large upper bandwidth limit, low footprint). Apart from the well-studied graphene, new 2D materials are gradually emerging, constantly renewing the interest in 2D-material-based modulators. High-ER and high-speed graphene modulators have already been experimentally reported, maintaining the interest for even greater metrics due to the inherently high carrier mobility in graphene. Theoretical predictions highlight potential EO bandwidths nominally exceeding 100 GHz,[264] limited mostly by the RC constant; at the same time, energy consumption from a few up to a few tens of fJ/bit is expected[264] and has been experimentally reported.[237] Generally, the optimum configuration of graphene upon a dielectric waveguide/resonator and the estimation of the upper performance metrics of amplitude and phase modulators is an open topic in the literature.[214,323–326] All publications converge that graphene has the potential for ultrahigh-speed modulation with high ER and acceptable ILs.

On the other hand, TDMs, MXenes, and BP, although exhibiting promising properties in principle, have more fundamental barriers to overcome, such as the achievement of efficient integration compatibility, accompanied with an overall low-cost and large-scale fabrication process. Besides, only recently, BP- and WS_2-based modulators were realized for the first time, showing promising performance metrics.[260,327] Low-cost and large-scale integration is an essential topic for graphene as well, since a wafer-scale transfer method for pure graphene sheets has yet to be achieved; the usage of reduced graphene oxide instead can be considered an alternative approach.[328] Finally, the most scientifically challenging but highly promising prospect is the design of Van der Waals heterostructures. Considering the numerous stacking variations, Van der Waals heterostructures are considered the future of 2D materials and can possibly enhance the performance of the respective modulators.

G. Phase-change materials

PCM-based modulators feature competitive performance in terms of footprint, extinction ratio, and insertion loss. However, they fall behind in switching speed, especially when the thermally induced transition cannot be suppressed. Relatively high switching speed and low power consumption can be achieved by selectively exploiting the electronically induced transition (nanosecond time scale) and successfully separating it from the much slower thermal one (microsecond time scale at best).[243,329] This can be achieved by designing the electrical addressing circuit to limit the current flow through the material,[243] minimizing Joule heating. This has a positive impact on energy consumption as well, but reduces the achievable extinction ratio. In addition, the experimentally observed hysteresis behavior seen in Fig. 17(b) is a limiting factor for modulator operation. As a result, there are still several open research questions to be solved in order for phase-change materials to compete with other alternatives and experience wider applicability.

VII. CONCLUSION

The state of the art in integrated electro-optic modulators has been reviewed, covering the different EO materials, integrated platforms, and physical phenomena that are involved in contemporary implementations. The current performance trends and the anticipated prospect of different material and modulator types have been highlighted. In addition, important physical aspects and frequently overlooked intricacies in the analysis and design of EO modulators have been identified and discussed.

AUTHORS' CONTRIBUTIONS

G.S. and T.C. contributed equally to this work.

ACKNOWLEDGMENTS

This research work was supported by the Hellenic Foundation for Research and Innovation (HFRI) under the "First Call for HFRI Research Projects to support Faculty members and Researchers and the procurement of high-cost research equipment grant" (Project No. HFRI-FM17-2086).

DATA AVAILABILITY

Most of the data included in this work are presented after consensual agreement of the corresponding author and/or the copyright owner; thus, data sharing is not applicable. The data that support the findings of this study are available from the corresponding author upon reasonable request.

REFERENCES

[1] A. Gnauck, R. Tkach, A. Chraplyvy, and T. Li, J. Lightwave Technol. **26**, 1032 (2008).
[2] P. Winzer, D. Neilson, and A. Chraplyvy, Opt. Express **26**, 24190 (2018).
[3] C. Kachris and I. Tomkos, IEEE Commun. Surv. Tutor. **14**, 1021 (2012).
[4] Q. Cheng, M. Bahadori, M. Glick, S. Rumleyand, and K. Bergman, Optica **5**, 1354 (2018).
[5] G. Roelkens, L. Liu, D. Liang, R. Jones, A. Fang, B. Koch, and J. Bowers, Laser Photonics Rev. **4**, 751 (2010).
[6] D. Rosenblatt, A. Sharon, and A. Friesem, IEEE J. Quantum Electron. **33**, 2038 (1997).
[7] Y.-W. Huang, H. Lee, R. Sokhoyan, R. Pala, K. Thyagarajan, S. Han, D. Tsai, and H. Atwater, Nano Lett. **16**, 5319 (2016).
[8] S. Yu, X. Wu, Y. Wang, X. Guo, and L. Tong, Adv. Mater. **29**, 1606128 (2017).
[9] D. C. Zografopoulos, G. Sinatkas, E. Lotfi, L. A. Shahada, M. A. Swillam, E. E. Kriezis, and R. Beccherelli, Appl. Phys. A **124**, 105 (2018).
[10] G. Isic, G. Sinatkas, D. Zografopoulos, B. Vasic, A. Ferraro, R. Beccherelli, E. Kriezis, and M. Belic, IEEE J. Sel. Top. Quantum Electron. **25**, 1 (2019).
[11] S. Doukas, A. Chatzilari, A. Dagkli, A. Papagiannopoulos, and E. Lidorikis, Appl. Phys. Lett. **113**, 011102 (2018).
[12] K. Liu, C. Ye, S. Khan, and V. Sorger, Laser Photonics Rev. **9**, 172 (2015).
[13] D. Miller, J. Lightwave Technol. **35**, 346 (2017).
[14] X. Chen, M. Milosevic, S. Stanković, S. Reynolds, T. Bucio, K. Li, D. Thomson, F. Gardes, and G. Reed, Proc. IEEE **106**, 2101 (2018).
[15] J. Witzens, Proc. IEEE **106**, 2158 (2018).
[16] D. Miller, Opt. Express **20**, A293 (2012).
[17] G. Li, Adv. Opt. Photonics **1**, 279 (2009).
[18] K. Kikuchi, IEICE Electron. Express **8**, 1642 (2011).
[19] K. Kikuchi, J. Lightwave Technol. **34**, 157 (2016).
[20] S. Lee, F. Breyer, S. Randel, R. Gaudino, G. Bosco, A. Bluschke, M. Matthews, P. Rietzsch, R. Steglich, H. van den Boom, and A. Koonen, J. Lightwave Technol. **27**, 1503 (2009).
[21] M. Olmedo, T. Zuo, J. Jensen, Q. Zhong, X. Xu, S. Popov, and I. Monroy, J. Lightwave Technol. **32**, 798 (2014).
[22] K. Akande and W. Popoola, J. Lightwave Technol. **36**, 4190 (2018).
[23] K. Zhong, X. Zhou, J. Huo, C. Yu, C. Lu, and A. Lau, J. Lightwave Technol. **36**, 377 (2018).
[24] X. Pang, O. Ozolins, R. Lin, L. Zhang, A. Udalcovs, L. Xue, R. Schatz, U. Westergren, S. Xiao, W. Hu, G. Jacobsen, S. Popov, and J. Chen, J. Lightwave Technol. **38**, 492 (2020).
[25] K. Iizuka, *Elements of Photonics, Volume I: In Free Space and Special Media*, 1st ed. (John Wiley & Sons, New York, 2002).
[26] V. Degiorgio and I. Cristiani, *Photonics: A Short Course*, 2nd ed. (Springer, New York, 2016).
[27] R. Weis and T. Gaylord, Appl. Phys. A: Solids Surf. **37**, 191 (1985).
[28] J. I. Pankove, *Optical Processes in Semiconductors*, 2nd ed. (Dover Publications, New York, 2010).
[29] D. A. B. Miller, D. S. Chemla, T. C. Damen, A. C. Gossard, W. Wiegmann, T. H. Wood, and C. A. Burrus, Phys. Rev. Lett. **53**, 2173 (1984).
[30] B. Bennett and R. Soref, IEEE J. Quantum Electron. **23**, 2159 (1987).
[31] G. T. Reed and A. P. Knights, *Silicon Photonics: An Introduction*, 1st ed. (John Wiley & Sons, Chicester, England, 2004).
[32] R. Soref and B. Bennett, IEEE J. Quantum Electron. **23**, 123 (1987).
[33] J. G. Mendoza-Alvarez, F. D. Nunes, and N. B. Patel, J. Appl. Phys. **51**, 4365 (1980).
[34] X. Yu, T. J. Marks, and A. Facchetti, Nat. Mater. **15**, 383 (2016).

[35]D. Zhan, J. Yan, L. Lai, Z. Ni, L. Liu, and Z. Shen, Adv. Mater. **24**, 4055 (2012).
[36]V. E. Babicheva, A. Boltasseva, and A. V. Lavrinenko, Nanophotonics **4**, 165 (2015).
[37]Z. Sun, A. Martinez, and F. Wang, Nat. Photonics **10**, 227 (2016).
[38]M. Wuttig, H. Bhaskaran, and T. Taubner, Nat. Photonics **11**, 465 (2017).
[39]E. Wooten, K. Kissa, A. Yi-Yan, E. Murphy, D. Lafaw, P. Hallemeier, D. Maack, D. Attanasio, D. Fritz, G. McBrien, and D. Bossi, IEEE J. Sel. Top. Quantum Electron. **6**, 69 (2000).
[40]M. Levy, R. M. Osgood, R. Liu, L. E. Cross, G. S. Cargill, A. Kumar, and H. Bakhru, Appl. Phys. Lett. **73**, 2293 (1998).
[41]P. Rabiei and P. Gunter, Appl. Phys. Lett. **85**, 4603 (2004).
[42]Y. Lee, G.-D. Kim, W.-J. Kim, S.-S. Lee, W.-G. Lee, and W. Steier, Opt. Lett. **36**, 1119 (2011).
[43]L. Chen, J. Chen, J. Nagy, and R. M. Reano, Opt. Express **23**, 13255 (2015).
[44]P. O. Weigel, J. Zhao, K. Fang, H. Al-Rubaye, D. Trotter, D. Hood, J. Mudrick, C. Dallo, A. T. Pomerene, A. L. Starbuck, C. T. DeRose, A. L. Lentine, G. Rebeiz, and S. Mookherjea, Opt. Express **26**, 23728 (2018).
[45]X. Wang, P. O. Weigel, J. Zhao, M. Ruesing, and S. Mookherjea, APL Photonics **4**, 096101 (2019).
[46]N. Boynton, H. Cai, M. Gehl, S. Arterburn, C. Dallo, A. Pomerene, A. Starbuck, D. Hood, D. C. Trotter, T. Friedmann, C. T. DeRose, and A. Lentine, Opt. Express **28**, 1868 (2020).
[47]P. Rabiei, J. Ma, S. Khan, J. Chiles, and S. Fathpour, Opt. Express **21**, 25573 (2013).
[48]A. Rao, A. Patil, J. Chiles, M. Malinowski, S. Novak, K. Richardson, P. Rabiei, and S. Fathpour, Opt. Express **23**, 22746 (2015).
[49]S. Jin, L. Xu, H. Zhang, and Y. Li, IEEE Photonics Technol. Lett. **28**, 736 (2016).
[50]L. Chang, M. H. P. Pfeiffer, N. Volet, M. Zervas, J. D. Peters, C. L. Manganelli, E. J. Stanton, Y. Li, T. J. Kippenberg, and J. E. Bowers, Opt. Lett. **42**, 803 (2017).
[51]A. N. R. Ahmed, S. Shi, A. J. Mercante, and D. W. Prather, Opt. Express **27**, 30741 (2019).
[52]M. Zhang, C. Wang, R. Cheng, A. Shams-Ansari, and M. Loncar, Optica **4**, 1536 (2017).
[53]A. J. Mercante, S. Shi, P. Yao, L. Xie, R. M. Weikle, and D. W. Prather, Opt. Express **26**, 14810 (2018).
[54]C. Wang, M. Zhang, X. Chen, M. Bertrand, A. Shams-Ansari, S. Chandrasekhar, P. Winzer, and M. Lončar, Nature **562**, 101 (2018).
[55]C. Wang, M. Zhang, B. Stern, M. Lipson, and M. Lončar, Opt. Express **26**, 1547 (2018).
[56]M. Bahadori, Y. Yang, L. L. Goddard, and S. Gong, Opt. Express **27**, 22025 (2019).
[57]B. Desiatov, A. Shams-Ansari, M. Zhang, C. Wang, and M. Lončar, Optica **6**, 380 (2019).
[58]T. Ren, M. Zhang, C. Wang, L. Shao, C. Reimer, Y. Zhang, O. King, R. Esman, T. Cullen, and M. Loncar, IEEE Photonics Technol. Lett. **31**, 889 (2019).
[59]M. Bahadori, L. L. Goddard, and S. Gong, Opt. Express **28**, 13731 (2020).
[60]M. Xu, W. Chen, M. He, X. Wen, Z. Ruan, J. Xu, L. Chen, L. Liu, S. Yu, and X. Cai, APL Photonics **4**, 100802 (2019).
[61]M. He, M. Xu, Y. Ren, J. Jian, Z. Ruan, Y. Xu, S. Gao, S. Sun, X. Wen, L. Zhou, L. Liu, C. Guo, H. Chen, S. Yu, L. Liu, and X. Cai, Nat. Photonics **13**, 359 (2019).
[62]A. Honardoost, F. A. Juneghani, R. Safian, and S. Fathpour, Opt. Express **27**, 6495 (2019).
[63]J. Jian, M. Xu, L. Liu, Y. Luo, J. Zhang, L. Liu, L. Zhou, H. Chen, S. Yu, and X. Cai, Opt. Express **27**, 18731 (2019).
[64]M. Thomaschewski, V. A. Zenin, C. Wolff, and S. I. Bozhevolnyi, Nat. Commun. **11**, 748 (2020).
[65]J. Macario, P. Yao, S. Shi, A. Zablocki, C. Harrity, D. Martin, C. A. Schuetz, and D. W. Prather, Opt. Express **20**, 23623 (2012).
[66]A. Rao, A. Patil, P. Rabiei, A. Honardoost, R. DeSalvo, A. Paolella, and S. Fathpour, Opt. Lett. **41**, 5700 (2016).
[67]A. Honardoost, R. Safian, A. Rao, and S. Fathpour, J. Lightwave Technol. **36**, 5893 (2018).
[68]M. Jazbinšek and M. Zgonik, Appl. Phys. B: Lasers Opt. **74**, 407 (2002).
[69]A. J. Mercante, P. Yao, S. Shi, G. Schneider, J. Murakowski, and D. W. Prather, Opt. Express **24**, 15590 (2016).
[70]C.-A. Berseth, C. Wuethrich, and F. K. Reinhart, J. Appl. Phys. **71**, 2821 (1992).
[71]R. Walker, J. Lightwave Technol. **5**, 1444 (1987).
[72]X. Fu, J. Cheng, Q. Huang, Y. Hu, W. Xie, M. Tassaert, J. Verbist, K. Ma, J. Zhang, K. Chen, C. Zhang, Y. Shi, J. Bauwelinck, G. Roelkens, L. Liu, and S. He, Opt. Express **23**, 18686 (2015).
[73]E. Alkhazraji, A. M. Ragheb, M. A. Esmail, Q. Tareq, H. Fathallah, S. A. Alshebeili, K. K. Qureshi, and M. Z. M. Khan, IEEE Photonics J. **12**, 1 (2020).
[74]T. Ido, S. Tanaka, M. Suzuki, M. Koizumi, H. Sano, and H. Inoue, J. Lightwave Technol. **14**, 2026 (1996).
[75]H. Fukano, T. Yamanaka, and M. Tamura, J. Lightwave Technol. **25**, 1961 (2007).
[76]W. Kobayashi, M. Arai, T. Yamanaka, N. Fujiwara, T. Fujisawa, T. Tadokoro, K. Tsuzuki, Y. Kondo, and F. Kano, J. Lightwave Technol. **28**, 164 (2010).
[77]K. Nozaki, A. Shakoor, S. Matsuo, T. Fujii, K. Takeda, A. Shinya, E. Kuramochi, and M. Notomi, APL Photonics **2**, 056105 (2017).
[78]M. A. Mestre, H. Mardoyan, C. Caillaud, R. Rios-Muller, J. Renaudier, P. Jenneve, F. Blache, F. Pommereau, J. Decobert, F. Jorge, P. Charbonnier, A. Konczykowska, J.-Y. Dupuy, K. Mekhazni, J.-F. Paret, M. Faugeron, F. Mallecot, M. Achouche, and S. Bigo, J. Lightwave Technol. **34**, 1572 (2016).
[79]Y. Nakai, A. Nakanishi, Y. Yamaguchi, S. Yamauchi, A. Nakamura, H. Asakura, H. Takita, S. Hayakawa, M. Mitaki, Y. Sakuma, and K. Naoe, J. Lightwave Technol. **37**, 1658 (2019).
[80]S. Kanazawa, Y. Nakanishi, S. Tsunashima, H. Yamazaki, Y. Ueda, W. Kobayashi, Y. Muramoto, H. Ishii, and H. Sanjoh, J. Lightwave Technol. **35**, 775 (2017).
[81]H. Yamazaki, M. Nagatani, F. Hamaoka, S. Kanazawa, H. Nosaka, T. Hashimoto, and Y. Miyamoto, J. Lightwave Technol. **35**, 1300 (2017).
[82]M. Chaciński, U. Westergren, B. Stoltz, R. Driad, R. E. Makon, V. Hurm, and A. G. Steffan, IEEE J. Sel. Top. Quantum Electron. **16**, 1321 (2010).
[83]J. M. Estaran, H. Mardoyan, F. Jorge, O. Ozolins, A. Udalcovs, A. Konczykowska, M. Riet, B. Duval, V. Nodjiadjim, J.-Y. Dupuy, X. Pang, U. Westergren, J. Chen, S. Popov, and S. Bigo, J. Lightwave Technol. **37**, 178 (2019).
[84]O. Ozolins, X. Pang, M. I. Olmedo, A. Kakkar, A. Udalcovs, S. Gaiarin, J. R. Navarro, K. M. Engenhardt, T. Asyngier, R. Schatz, J. Li, F. Nordwall, U. Westergren, D. Zibar, S. Popov, and G. Jacobsen, J. Lightwave Technol. **35**, 1174 (2017).
[85]L. Zhang, X. Hong, X. Pang, O. Ozolins, A. Udalcovs, R. Schatz, C. Guo, J. Zhang, F. Nordwall, K. M. Engenhardt, U. Westergren, S. Popov, G. Jacobsen, S. Xiao, W. Hu, and J. Chen, Opt. Lett. **43**, 182 (2018).
[86]M. L. Nielsen, K. Tsuruoka, T. Kato, T. Morimoto, S. Sudo, T. Okamoto, K. Mizutani, K. Sato, and K. Kudo, IEEE Photonics Technol. Lett. **20**, 1270 (2008).
[87]Y. Sasahata, T. Saito, T. Takiguchi, K. Takagi, K. Matsumoto, T. Nagira, H. Sakuma, D. Suzuki, R. Makita, M. Takabayashi, M. Gotoda, and E. Ishimura, IEEE J. Sel. Top. Quantum Electron. **19**, 1501507 (2013).
[88]S. Lange, M. Gruner, C. Meuer, R. Kaiser, M. Hamacher, K.-O. Velthaus, and M. Schell, J. Lightwave Technol. **34**, 401 (2016).
[89]S. Lange, S. Wolf, J. Lutz, L. Altenhain, R. Schmid, R. Kaiser, M. Schell, C. Koos, and S. Randel, J. Lightwave Technol. **36**, 97 (2018).
[90]R. W. Going, M. Lauermann, R. Maher, H.-S. Tsai, A. Hosseini, M. Lu, N. Kim, P. Studenkov, S. W. Corzine, J. Summers, M. Anagnosti, M. Montazeri, J. Zhang, B. Behnia, J. Tang, S. Buggaveeti, T. Vallaitis, J. Osenbach, M. Kuntz, X. Xu, K. Croussore, V. Lal, P. Evans, J. T. Rahn, T. Butrie, A. Karanicolas, K.-T. Wu, M. Mitchell, M. Ziari, D. Welch, and F. Kish, IEEE J. Quantum Electron. **54**, 1 (2018).
[91]Y. Ogiso, Y. Hashizume, H. Tanobe, N. Nunoya, M. Ida, Y. Miyamoto, M. Ishikawa, J. Ozaki, Y. Ueda, H. Wakita, M. Nagatani, H. Yamazaki, M. Nakamura, T. Kobayashi, and S. Kanazawa, J. Lightwave Technol. **38**, 249 (2020).

[92] H. Yamazaki, M. Nagatani, H. Wakita, Y. Ogiso, M. Nakamura, M. Ida, H. Nosaka, T. Hashimoto, and Y. Miyamoto, J. Lightwave Technol. **37**, 1772 (2019).

[93] R. G. Walker, N. I. Cameron, Y. Zhou, and S. J. Clements, IEEE J. Sel. Top. Quantum Electron. **19**, 138 (2013).

[94] P. C. Schindler, D. Korn, C. Stamatiadis, M. F. OKeefe, L. Stampoulidis, R. Schmogrow, P. Zakynthinos, R. Palmer, N. Cameron, Y. Zhou, R. G. Walker, E. Kehayas, S. Ben-Ezra, I. Tomkos, L. Zimmermann, K. Petermann, W. Freude, C. Koos, and J. Leuthold, J. Lightwave Technol. **32**, 760 (2014).

[95] J. H. Shin and N. Dagli, IEEE J. Sel. Top. Quantum Electron. **19**, 150 (2013).

[96] M. J. R. Heck, H.-W. Chen, A. W. Fang, B. R. Koch, D. Liang, H. Park, M. N. Sysak, and J. E. Bowers, IEEE J. Sel. Top. Quantum Electron. **17**, 333 (2011).

[97] A. Abbasi, J. Verbist, L. A. Shiramin, M. Verplaetse, T. D. Keulenaer, R. Vaernewyck, R. Pierco, A. Vyncke, X. Yin, G. Torfs, G. Morthier, J. Bauwelinck, and G. Roelkens, IEEE Photonics Technol. Lett. **30**, 1095 (2018).

[98] Y. Tang, J. D. Peters, and J. E. Bowers, Opt. Express **20**, 11529 (2012).

[99] T. Hiraki, T. Aihara, T. Fujii, K. Takeda, T. Kakitsuka, T. Tsuchizawa, and S. Matsuo, J. Lightwave Technol. **38**, 3030 (2020).

[100] T. Hiraki, T. Aihara, K. Hasebe, K. Takeda, T. Fujii, T. Kakitsuka, T. Tsuchizawa, H. Fukuda, and S. Matsuo, Nat. Photonics **11**, 482 (2017).

[101] J.-H. Han, F. Boeuf, J. Fujikata, S. Takahashi, S. Takagi, and M. Takenaka, Nat. Photonics **11**, 486 (2017).

[102] Q. Li, C. P. Ho, S. Takagi, and M. Takenaka, IEEE Photonics Technol. Lett. **32**, 345 (2020).

[103] M. Nedeljkovic, R. Soref, and G. Z. Mashanovich, IEEE Photonics J. **3**, 1171 (2011).

[104] A. Liu, R. Jones, L. Liao, D. Samara-Rubio, D. Rubin, O. Cohen, R. Nicolaescu, and M. Paniccia, Nature **427**, 615 (2004).

[105] P. Dong, C. Xie, L. Chen, L. L. Buhl, and Y.-K. Chen, Opt. Express **20**, B624 (2012).

[106] A. Samani, M. Chagnon, D. Patel, V. Veerasubramanian, S. Ghosh, M. Osman, Q. Zhong, and D. V. Plant, IEEE Photonics J. **7**, 1 (2015).

[107] H. Sepehrian, J. Lin, L. A. Rusch, and W. Shi, J. Lightwave Technol. **37**, 3078 (2019).

[108] R. Dubé-Demers, S. LaRochelle, and W. Shi, Optica **3**, 622 (2016).

[109] S. S. Azadeh, F. Merget, S. Romero-García, A. Moscoso-Mártir, N. von den Driesch, J. Müller, S. Mantl, D. Buca, and J. Witzens, Opt. Express **23**, 23526 (2015).

[110] T. Baba, S. Akiyama, M. Imai, and T. Usuki, Opt. Express **23**, 32950 (2015).

[111] L. Liao, A. Liu, R. Jones, D. Rubin, D. Samara-Rubio, O. Cohen, M. Salib, and M. Paniccia, IEEE J. Quantum Electron. **41**, 250 (2005).

[112] G. Kim, J. W. Park, I. G. Kim, S. Kim, K.-S. Jang, S. A. Kim, J. H. Oh, J. Joo, and S. Kim, Opt. Lett. **39**, 2310 (2014).

[113] D. J. Thomson, F. Y. Gardes, Y. Hu, G. Mashanovich, M. Fournier, P. Grosse, J.-M. Fedeli, and G. T. Reed, Opt. Express **19**, 11507 (2011).

[114] X. Xiao, H. Xu, X. Li, Z. Li, T. Chu, Y. Yu, and J. Yu, Opt. Express **21**, 4116 (2013).

[115] M. Streshinsky, R. Ding, Y. Liu, A. Novack, Y. Yang, Y. Ma, X. Tu, E. K. S. Chee, A. E.-J. Lim, P. G.-Q. Lo, T. Baehr-Jones, and M. Hochberg, Opt. Express **21**, 30350 (2013).

[116] S. Jain, S. Rajput, V. Kaushik, and M. Kumar, Opt. Commun. **434**, 49 (2019).

[117] D. Patel, S. Ghosh, M. Chagnon, A. Samani, V. Veerasubramanian, M. Osman, and D. V. Plant, Opt. Express **23**, 14263 (2015).

[118] Q. Xu, B. Schmidt, S. Pradhan, and M. Lipson, Nature **435**, 325 (2005).

[119] Z. Xuan, Y. Ma, Y. Liu, R. Ding, Y. Li, N. Ophir, A. E.-J. Lim, G.-Q. Lo, P. Magill, K. Bergman, T. Baehr-Jones, and M. Hochberg, Opt. Express **22**, 28284 (2014).

[120] E. Timurdogan, C. M. Sorace-Agaskar, J. Sun, E. S. Hosseini, A. Biberman, and M. R. Watts, Nat. Commun. **5**, 4008 (2014).

[121] A. Shakoor, K. Nozaki, E. Kuramochi, K. Nishiguchi, A. Shinya, and M. Notomi, Opt. Express **22**, 28623 (2014).

[122] Y. Tong, Z. Hu, X. Wu, S. Liu, L. Chang, A. Netherton, C.-K. Chan, J. E. Bowers, and H. K. Tsang, IEEE Photonics Technol. Lett. **32**, 125 (2020).

[123] J. Sun, R. Kumar, M. Sakib, J. B. Driscoll, H. Jayatilleka, and H. Rong, J. Lightwave Technol. **37**, 110 (2019).

[124] B. Milivojevic, S. Wiese, S. Anderson, T. Brenner, M. Webster, and B. Dama, J. Lightwave Technol. **35**, 768 (2017).

[125] A. Brimont, D. J. Thomson, P. Sanchis, J. Herrera, F. Gardes, J. M. Fedeli, G. T. Reed, and J. Martí, Opt. Express **19**, 20876 (2011).

[126] M. Caverley, X. Wang, K. Murray, N. A. F. Jaeger, and L. Chrostowski, IEEE Photonics Technol. Lett. **27**, 2331 (2015).

[127] R. S. Jacobsen, K. N. Andersen, P. I. Borel, J. Fage-Pedersen, L. H. Frandsen, O. Hansen, M. Kristensen, A. V. Lavrinenko, G. Moulin, H. Ou, C. Peucheret, B. Zsigri, and A. Bjarklev, Nature **441**, 199 (2006).

[128] P. Damas, M. Berciano, G. Marcaud, C. A. Ramos, D. Marris-Morini, E. Cassan, and L. Vivien, J. Appl. Phys. **122**, 153105 (2017).

[129] M. Berciano, G. Marcaud, P. Damas, X. L. Roux, P. Crozat, C. A. Ramos, D. P. Galacho, D. Benedikovic, D. Marris-Morini, E. Cassan, and L. Vivien, Commun. Phys. **1**, 64 (2018).

[130] N.-N. Feng, D. Feng, S. Liao, X. Wang, P. Dong, H. Liang, C.-C. Kung, W. Qian, J. Fong, R. Shafiiha, Y. Luo, J. Cunningham, A. V. Krishnamoorthy, and M. Asghari, Opt. Express **19**, 7062 (2011).

[131] A. E.-J. Lim, T.-Y. Liow, F. Qing, N. Duan, L. Ding, M. Yu, G.-Q. Lo, and D.-L. Kwong, Opt. Express **19**, 5040 (2011).

[132] S. A. Srinivasan, M. Pantouvaki, S. Gupta, H. T. Chen, P. Verheyen, G. Lepage, G. Roelkens, K. Saraswat, D. V. Thourhout, P. Absil, and J. V. Campenhout, J. Lightwave Technol. **34**, 419 (2016).

[133] J. Fujikata, M. Noguchi, K. Kawashita, R. Katamawari, S. Takahashi, M. Nishimura, H. Ono, D. Shimura, H. Takahashi, H. Yaegashi, T. Nakamura, and Y. Ishikawa, Opt. Express **28**, 33123 (2020).

[134] Z. Liu, X. Li, C. Niu, J. Zheng, C. Xue, Y. Zuo, and B. Cheng, Photonics Res. **8**, 1648 (2020).

[135] J. Liu, M. Beals, A. Pomerene, S. Bernardis, R. Sun, J. Cheng, L. C. Kimerling, and J. Michel, Nat. Photonics **2**, 433 (2008).

[136] D. Feng, S. Liao, H. Liang, J. Fong, B. Bijlani, R. Shafiiha, B. J. Luff, Y. Luo, J. Cunningham, A. V. Krishnamoorthy, and M. Asghari, Opt. Express **20**, 22224 (2012).

[137] L. Mastronardi, M. Banakar, A. Khokhar, N. Hattasan, T. Rutirawut, T. D. Bucio, K. M. Grabska, C. Littlejohns, A. Bazin, G. Mashanovich, and F. Gardes, Opt. Express **26**, 6663 (2018).

[138] Y.-H. Kuo, Y. K. Lee, Y. Ge, S. Ren, J. E. Roth, T. I. Kamins, D. A. B. Miller, and J. S. Harris, Nature **437**, 1334 (2005).

[139] P. Chaisakul, D. Marris-Morini, M.-S. Rouifed, G. Isella, D. Chrastina, J. Frigerio, X. L. Roux, S. Edmond, J.-R. Coudevylle, and L. Vivien, Opt. Express **20**, 3219 (2012).

[140] S. Ren, Y. Rong, S. A. Claussen, R. K. Schaevitz, T. I. Kamins, J. S. Harris, and D. A. B. Miller, IEEE Photonics Technol. Lett. **24**, 461 (2012).

[141] A. Melikyan, N. Kaneda, K. Kim, Y. Baeyens, and P. Dong, J. Lightwave Technol. **38**, 2872 (2020).

[142] J. Fujikata, M. Noguchi, Y. Kim, J. Han, S. Takahashi, T. Nakamura, and M. Takenaka, Appl. Phys. Express **11**, 032201 (2018).

[143] J. Frigerio, P. Chaisakul, D. Marris-Morini, S. Cecchi, M. S. Roufied, G. Isella, and L. Vivien, Appl. Phys. Lett. **102**, 061102 (2013).

[144] Y. Kim, J. Fujikata, S. Takahashi, M. Takenaka, and S. Takagi, Opt. Express **24**, 1979 (2016).

[145] Y.-C. Chang, S. P. Roberts, B. Stern, I. Datta, and M. Lipson, in *Conference on Lasers and Electro-Optics* (OSA, 2017).

[146] T. N. Huynh, N. Dupuis, R. Rimolo-Donadio, J. E. Proesel, D. M. Gill, C. W. Baks, A. V. Rylyakov, C. L. Schow, W. M. J. Green, and B. G. Lee, J. Lightwave Technol. **34**, 5129 (2016).

[147] B. G. Lee, N. Dupuis, R. Rimolo-Donadio, T. N. Huynh, C. W. Baks, D. M. Gill, and W. M. J. Green, in *Optical Fiber Communication Conference* (OSA, 2017).

[148] H. Ma, A. K. Jen, and L. R. Dalton, Adv. Mater. **14**, 1339 (2002).

[149] J. Luo, S. Huang, Y. J. Cheng, T. D. Kim, Z. Shi, X. H. Zhou, and A. K. Jen, Org. Lett. **9**, 4471 (2007).

[150] L. R. Dalton, P. A. Sullivan, and D. H. Bale, Chem. Rev. **110**, 25 (2010).
[151] Y. Enami, D. Mathine, C. T. Derose, R. A. Norwood, J. Luo, A. K. Jen, and N. Peyghambarian, Appl. Phys. Lett. **91**, 093505 (2007).
[152] M.-C. Oh, H. Zhang, A. Szep, V. Chuyanov, W. Steier, C. Zhang, L. Dalton, H. Erlig, B. Tsap, and H. Fetterman, Appl. Phys. Lett. **76**, 3525 (2000).
[153] H. Zhang, M. C. Oh, A. Szep, W. H. Steier, C. Zhang, L. R. Dalton, H. Erlig, Y. Chang, D. H. Chang, and H. R. Fetterman, Appl. Phys. Lett. **78**, 3136 (2001).
[154] M. Lee, H. E. Katz, C. Erben, D. M. Gill, P. Gopalan, J. D. Heber, and D. J. Mcgee, Science **298**, 1401 (2002).
[155] Y. Shi, W. Lin, D. J. Olson, J. H. Bechtel, H. Zhang, W. H. Steier, C. Zhang, and L. R. Dalton, Appl. Phys. Lett. **77**, 1 (2000).
[156] Y. Shi, C. Zhang, H. Zhang, J. H. Bechtel, L. R. Dalton, B. H. Robinson, and W. H. Steier, Science **288**, 119 (2000).
[157] X. Zhang, A. Hosseini, X. Lin, H. Subbaraman, and R. T. Chen, IEEE J. Sel. Top. Quantum Electron. **19**, 196 (2013).
[158] H. Sato, H. Miura, F. Qiu, A. M. Spring, T. Kashino, T. Kikuchi, M. Ozawa, H. Nawata, K. Odoi, and S. Yokoyama, Opt. Express **25**, 768 (2017).
[159] M. Hochberg, T. Baehr-Jones, G. Wang, J. Huang, P. Sullivan, L. Dalton, and A. Scherer, Opt. Express **15**, 8401 (2007).
[160] T. Baehr-Jones, B. Penkov, J. Huang, P. Sullivan, J. Davies, J. Takayesu, J. Luo, T. D. Kim, L. Dalton, A. Jen, M. Hochberg, and A. Scherer, Appl. Phys. Lett. **92**, 10 (2008).
[161] R. Ding, T. Baehr-Jones, Y. Liu, R. Bojko, J. Witzens, S. Huang, J. Luo, S. Benight, P. Sullivan, J. M. Fedeli, M. Fournier, L. Dalton, A. Jen, and M. Hochberg, Opt. Express **18**, 15618 (2010).
[162] L. Alloatti, D. Korn, R. Palmer, D. Hillerkuss, J. Li, A. Barklund, R. Dinu, M. Fournier, J. Fedeli, H. Yu, W. Bogaerts, P. Dumon, and R. Baets, Opt. Express **19**, 11841 (2011).
[163] D. Korn, R. Palmer, H. Yu, P. C. Schindler, L. Alloatti, M. Baier, R. Schmogrow, W. Bogaerts, S. K. Selvaraja, G. Lepage, M. Pantouvaki, J. M. Wouters, P. Verheyen, J. Van Campenhout, B. Chen, R. Baets, P. Absil, R. Dinu, C. Koos, W. Freude, and J. Leuthold, Opt. Express **21**, 13219 (2013).
[164] J. Leuthold, C. Koos, W. Freude, L. Alloatti, R. Palmer, D. Korn, J. Pfeifle, M. Lauermann, R. Dinu, S. Wehrli, M. Jazbinsek, P. Günter, M. Waldow, T. Wahlbrink, J. Bolten, H. Kurz, M. Fournier, J. M. Fedeli, H. Yu, and W. Bogaerts, IEEE J. Sel. Top. Quantum Electron. **19**, 114 (2013).
[165] R. Palmer, L. Alloatti, D. Korn, P. C. Schindler, M. Baier, J. Bolten, T. Wahlbrink, M. Waldow, R. Dinu, W. Freude, C. Koos, and J. Leuthold, IEEE Photonics Technol. Lett. **25**, 1226 (2013).
[166] L. Alloatti, R. Palmer, S. Diebold, K. P. Pahl, B. Chen, R. Dinu, M. Fournier, J. M. Fedeli, T. Zwick, W. Freude, C. Koos, and J. Leuthold, Light: Sci. Appl. **3**, 5 (2014).
[167] M. Lauermann, R. Palmer, S. Koeber, P. C. Schindler, D. Korn, T. Wahlbrink, J. Bolten, M. Waldow, D. L. Elder, L. R. Dalton, J. Leuthold, W. Freude, and C. Koos, Opt. Express **22**, 29927 (2014).
[168] R. Palmer, S. Koeber, D. L. Elder, M. Woessner, W. Heni, D. Korn, M. Lauermann, W. Bogaerts, L. Dalton, W. Freude, J. Leuthold, and C. Koos, J. Lightwave Technol. **32**, 2726 (2014).
[169] S. Koeber, R. Palmer, M. Lauermann, W. Heni, D. L. Elder, D. Korn, M. Woessner, L. Alloatti, S. Koenig, P. C. Schindler, H. Yu, W. Bogaerts, L. R. Dalton, W. Freude, J. Leuthold, and C. Koos, Light: Sci. Appl. **4**, e255 (2015).
[170] S. Wolf, M. Lauermann, P. Schindler, G. Ronniger, K. Geistert, R. Palmer, S. Kober, W. Bogaerts, J. Leuthold, W. Freude, and C. Koos, J. Lightwave Technol. **33**, 1425 (2015).
[171] C. Kieninger, Y. Kutuvantavida, D. L. Elder, S. Wolf, H. Zwickel, M. Blaicher, J. N. Kemal, M. Lauermann, S. Randel, W. Freude, L. R. Dalton, and C. Koos, Optica **5**, 739 (2018).
[172] S. Wolf, H. Zwickel, C. Kieninger, M. Lauermann, W. Hartmann, Y. Kutuvantavida, W. Freude, S. Randel, and C. Koos, Opt. Express **26**, 220 (2018).
[173] C. Koos, J. Leuthold, W. Freude, S. Member, M. Kohl, L. Dalton, S. Member, W. Bogaerts, S. Member, A. L. Giesecke, M. Lauermann, A. Melikyan, S. Koeber, S. Wolf, C. Weimann, S. Muehlbrandt, K. Koehnle, J. Pfeifle, W. Hartmann, Y. Kutuvantavida, S. Ummethala, R. Palmer, D. Korn, L. Alloatti, P. C. Schindler, D. L. Elder, T. Wahlbrink, and J. Bolten, J. Lightwave Technol. **34**, 256 (2016).
[174] C. Y. Lin, X. Wang, S. Chakravarty, B. S. Lee, W. Lai, J. Luo, A. K. Jen, and R. T. Chen, Appl. Phys. Lett. **97**, 093304 (2010).
[175] X. Wang, C.-Y. Lin, S. Chakravarty, J. Luo, A. K.-Y. Jen, and R. T. Chen, Opt. Lett. **36**, 882 (2011).
[176] X. Zhang, A. Hosseini, S. Chakravarty, J. Luo, A. K.-Y. Jen, and R. T. Chen, Opt. Lett. **38**, 4931 (2013).
[177] X. Zhang, C. J. Chung, A. Hosseini, H. Subbaraman, J. Luo, A. K. Jen, R. L. Nelson, C. Y. Lee, and R. T. Chen, J. Lightwave Technol. **34**, 2941 (2016).
[178] A. Melikyan, L. Alloatti, A. Muslija, D. Hillerkuss, P. Schindler, J. Li, R. Palmer, D. Korn, S. Muehlbrandt, D. Van Thourhout, W. Freude, and J. Leuthold, Nat. Photonics **8**, 229 (2014).
[179] C. Hoessbacher, A. Josten, B. Baeuerle, Y. Fedoryshyn, H. Hettrich, Y. Salamin, W. Heni, C. Haffner, C. Kaiser, R. Schmid, D. L. Elder, D. Hillerkuss, M. Möller, L. R. Dalton, and J. Leuthold, Opt. Express **25**, 1762 (2017).
[180] B. A. Block, T. R. Younkin, P. S. Davids, M. R. Reshotko, P. Chang, B. M. Polishak, S. Huang, J. Luo, and A. K. Y. Jen, Opt. Express **16**, 18326 (2008).
[181] M. Balakrishnan, M. Faccini, M. Diemeer, E. Klein, G. Sengo, A. Driessen, W. Verboom, and D. Reinhoudt, Appl. Phys. Lett. **92**, 153310 (2008).
[182] F. Qiu, A. M. Spring, H. Miura, D. Maeda, M. A. Ozawa, K. Odoi, and S. Yokoyama, ACS Photonics **3**, 780 (2016).
[183] D. C. Zografopoulos, M. Swillam, and R. Beccherelli, IEEE Photonics Technol. Lett. **28**, 818 (2016).
[184] Z. Pan, X. Xu, C.-J. Chung, H. Dalir, H. Yan, K. Chen, Y. Wang, B. Jia, and R. Chen, Laser Photonics Rev. **12**, 1700300 (2018).
[185] A. Hosseinzadeh and C. T. Middlebrook, J. Lightwave Technol. **37**, 755 (2019).
[186] K. Ellmer, Nat. Photonics **6**, 809 (2012).
[187] G. Sinatkas and E. E. Kriezis, IEEE J. Quantum Electron. **54**, 1 (2018).
[188] E. Feigenbaum, K. Diest, and H. A. Atwater, Nano Lett. **10**, 2111 (2010).
[189] P. P. Edwards, A. Porch, M. O. Jones, D. V. Morgan, and R. M. Perks, Dalton Trans. **2004**, 2995.
[190] Z. Ma, Z. Li, K. Liu, C. Ye, and V. J. Sorger, Nanophotonics **4**, 198 (2015).
[191] G. D. Wilk, R. M. Wallace, and J. M. Anthony, J. Appl. Phys. **89**, 5243 (2001).
[192] A. Melikyan, N. Lindenmann, S. Walheim, P. M. Leufke, S. Ulrich, J. Ye, P. Vincze, H. Hahn, T. Schimmel, C. Koos, W. Freude, and J. Leuthold, Opt. Express **19**, 8855 (2011).
[193] A. V. Krasavin and A. V. Zayats, Phys. Rev. Lett. **109**, 053901 (2012).
[194] V. E. Babicheva and A. V. Lavrinenko, Opt. Commun. **285**, 5500 (2012).
[195] H. W. Lee, G. Papadakis, S. P. Burgos, K. Chander, A. Kriesch, R. Pala, U. Peschel, and H. A. Atwater, Nano Lett. **14**, 6463 (2014).
[196] C. Huang, R. J. Lamond, S. K. Pickus, Z. R. Li, and V. J. Sorger, IEEE Photonics J. **5**, 2202411 (2013).
[197] V. E. Babicheva, N. Kinsey, G. V. Naik, M. Ferrera, A. V. Lavrinenko, V. M. Shalaev, and A. Boltasseva, Opt. Express **21**, 27326 (2013).
[198] S. Zhu, G. Q. Lo, and D. L. Kwong, Opt. Express **22**, 17930 (2014).
[199] T. Amemiya, E. Murai, Z. Gu, N. Nishiyama, and S. Arai, J. Opt. Soc. Am. B **31**, 2908 (2014).
[200] Z. Lu, W. Zhao, and K. Shi, IEEE Photonics J. **4**, 735 (2012).
[201] A. P. Vasudev, J.-H. Kang, J. Park, X. Liu, and M. L. Brongersma, Opt. Express **21**, 26387 (2013).
[202] H. Zhao, Y. Wang, A. Capretti, L. D. Negro, and J. Klamkin, IEEE J. Sel. Top. Quantum Electron. **21**, 3300207 (2015).
[203] G. Sinatkas, A. Pitilakis, D. C. Zografopoulos, R. Beccherelli, and E. E. Kriezis, J. Appl. Phys. **121**, 023109 (2017).
[204] R. Amin, R. Maiti, C. Carfano, Z. Ma, M. H. Tahersima, Y. Lilach, D. Ratnayake, H. Dalir, and V. J. Sorger, APL Photonics **3**, 126104 (2018).
[205] R. Amin, R. Maiti, Y. Gui, C. Suer, M. Miscuglio, E. Heidari, R. T. Chen, H. Dalir, and V. J. Sorger, Optica **7**, 333 (2020).

[206] E. Li, Q. Gao, R. T. Chen, and A. X. Wang, Nano Lett. **18**, 1075 (2018).

[207] E. Li, B. A. Nia, B. Zhou, and A. X. Wang, Photonics Res. **7**, 473 (2019).

[208] E. Li, B. Zhou, Y. Bo, and A. X. Wang, J. Lightwave Technol. **39**, 178 (2021).

[209] C. Lin and A. S. Helmy, Sci. Rep. **5**, 12313 (2015).

[210] I. C. Reines, M. G. Wood, T. S. Luk, D. K. Serkland, and S. Campione, Opt. Express **26**, 21594 (2018).

[211] U. Koch, C. Hoessbacher, J. Niegemann, C. Hafner, and J. Leuthold, IEEE Photonics J. **8**, 4800813 (2016).

[212] Q. Gao, E. Li, and A. X. Wang, Opt. Mater. Express **8**, 2850 (2018).

[213] V. J. Sorger, N. D. Lanzillotti-Kimura, R.-M. Ma, and X. Zhang, Nanophotonics **1**, 17 (2012).

[214] G. Sinatkas, T. Christopoulos, O. Tsilipakos, and E. E. Kriezis, Phys. Rev. Appl. **12**, 064023 (2019).

[215] Q. Gao, E. Li, and A. X. Wang, Photonics Res. **6**, 277 (2018).

[216] M. G. Wood, S. Campione, S. Parameswaran, T. S. Luk, J. R. Wendt, D. K. Serkland, and G. A. Keeler, Optica **5**, 233 (2018).

[217] Q. Gao, E. Li, B. Zhou, and A. X. Wang, J. Nanophotonics **13**, 036005 (2019).

[218] X. Liu, K. Zang, J.-H. Kang, J. Park, J. S. Harris, P. G. Kik, and M. L. Brongersma, ACS Photonics **5**, 4484 (2018).

[219] M. H. Tahersima, Z. Ma, Y. Gui, S. Sun, H. Wang, R. Amin, H. Dalir, R. Chen, M. Miscuglio, and V. J. Sorger, Nanophotonics **8**, 1559 (2019).

[220] R. Amin, R. Maiti, Y. Gui, C. Suer, M. Miscuglio, E. Heidari, J. B. Khurgin, R. T. Chen, H. Dalir, and V. J. Sorger, Sci. Rep. **11**, 1287 (2021).

[221] B. Zhou, E. Li, Y. Bo, and A. X. Wang, J. Lightwave Technol. **38**, 3338 (2020).

[222] T. Tan, X. Jiang, C. Wang, B. Yao, and H. Zhang, Adv. Sci. **7**, 2000058 (2020).

[223] S. Psilodimitrakopoulos, L. Mouchliadis, I. Paradisanos, A. Lemonis, G. Kioseoglou, and E. Stratakis, Light: Sci. Appl. **7**, 18005 (2018).

[224] Q. Chen, L. Liang, G. Potsi, P. Wan, J. Lu, T. Giousis, E. Thomou, D. Gournis, P. Rudolf, and J. Ye, Nano Lett. **19**, 1520 (2019).

[225] I. Papadakis, A. Stathis, A. B. Bourlinos, and S. Couris, Nano Select **1**, 395 (2020).

[226] M. Liu, X. Yin, E. Ulin-Avila, B. Geng, T. Zentgraf, L. Ju, F. Wang, and X. Zhang, Nature **474**, 64 (2011).

[227] M. Liu, X. Yin, and X. Zhang, Nano Lett. **12**, 1482 (2012).

[228] H. Dalir, Y. Xia, Y. Wang, and X. Zhang, ACS Photonics **3**, 1564 (2016).

[229] Y. Hu, M. Pantouvaki, J. V. Campenhout, S. Brems, I. Asselberghs, C. Huyghebaert, P. Absil, and D. V. Thourhout, Laser Photon. Rev. **10**, 307 (2016).

[230] M. A. Giambra, V. Sorianello, V. Miseikis, S. Marconi, A. Montanaro, P. Galli, S. Pezzini, C. Coletti, and M. Romagnoli, Opt. Express **27**, 20145 (2019).

[231] Y. Ding, X. Guan, X. Zhu, H. Hu, S. I. Bozhevolnyi, L. K. Oxenløwe, K. J. Jin, N. A. Mortensen, and S. Xiao, Nanoscale **9**, 15576 (2017).

[232] X. Peng, R. Hao, Z. Ye, P. Qin, W. Chen, H. Chen, X. Jin, D. Yang, and E. Li, Opt. Lett. **42**, 1736 (2017).

[233] X. Hu and J. Wang, IEEE J. Quantum Electron. **53**, 1 (2017).

[234] H. Shu, Z. Su, L. Huang, Z. Wu, X. Wang, Z. Zhang, and Z. Zhou, Sci. Rep. **8**, 991 (2018).

[235] M. Mohsin, D. Neumaier, D. Schall, M. Otto, C. Matheisen, A. L. Giesecke, A. A. Sagade, and H. Kurz, Sci. Rep. **5**, 10967 (2015).

[236] V. Sorianello, M. Midrio, G. Contestabile, I. Asselberghs, J. V. Campenhout, C. Huyghebaert, I. Goykhman, A. K. Ott, A. C. Ferrari, and M. Romagnoli, Nat. Photonics **12**, 40 (2018).

[237] C. T. Phare, Y.-H. D. Lee, J. Cardenas, and M. Lipson, Nat. Photonics **9**, 511 (2015).

[238] C. Qiu, W. Gao, R. Vajtai, P. M. Ajayan, J. Kono, and Q. Xu, Nano Lett. **14**, 6811 (2014).

[239] X. Gan, R.-J. Shiue, Y. Gao, K. F. Mak, X. Yao, L. Li, A. Szep, D. Walker, J. Hone, T. F. Heinz, and D. Englund, Nano Lett. **13**, 691 (2013).

[240] T. Pan, C. Qiu, J. Wu, X. Jiang, B. Liu, Y. Yang, H. Zhou, R. Soref, and Y. Su, Opt. Express **23**, 23357 (2015).

[241] K. J. Miller, R. F. Haglund, and S. M. Weiss, Opt. Mater. Express **8**, 2415 (2018).

[242] A. Joushaghani, J. Jeong, S. Paradis, D. Alain, J. Stewart Aitchison, and J. K. S. Poon, Opt. Express **23**, 3657 (2015).

[243] P. Markov, R. E. Marvel, H. J. Conley, K. J. Miller, R. F. Haglund, and S. M. Weiss, ACS Photonics **2**, 1175 (2015).

[244] J. T. Kim, Opt. Lett. **39**, 3997 (2014).

[245] J. H. Choe and J. T. Kim, IEEE Photonics Technol. Lett. **27**, 514 (2015).

[246] P. Markov, K. Appavoo, R. F. Haglund, and S. M. Weiss, Opt. Express **23**, 6878 (2015).

[247] B. Janjan, M. Miri, A. Zarifkar, and M. Heidari, J. Lightwave Tech. **35**(14), 3020–3028 (2017).

[248] L. D. S. Diana, F. C. Juan, A. R. Escutia, and P. S. Kilders, J. Opt. **19**, 035401 (2017).

[249] H. M. Wong and A. S. Helmy, J. Lightwave Technol. **36**, 797 (2018).

[250] O. Tsilipakos and E. E. Kriezis, J. Opt. Soc. Am. B **31**, 1698 (2014).

[251] O. Tsilipakos, T. Christopoulos, and E. E. Kriezis, J. Lightwave Technol. **34**, 1333 (2016).

[252] H.-W. Chen, Y. Kuo, and J. E. Bowers, Chin. Opt. Lett. **7**, 280 (2009).

[253] M. Xu, M. He, H. Zhang, J. Jian, Y. Pan, X. Liu, L. Chen, X. Meng, H. Chen, Z. Li, X. Xiao, S. Yu, S. Yu, and X. Cai, Nat. Commun. **11**, 3911 (2020).

[254] S. Dogru and N. Dagli, J. Lightwave Technol. **32**, 435 (2014).

[255] G. W. Lu, J. Hong, F. Qiu, A. M. Spring, T. Kashino, J. Oshima, M. aki Ozawa, H. Nawata, and S. Yokoyama, Nat. Commun. **11**, 4224 (2020).

[256] X. Tu, T.-Y. Liow, J. Song, X. Luo, Q. Fang, M. Yu, and G.-Q. Lo, Opt. Express **21**, 12776 (2013).

[257] Y. Yang, Q. Fang, M. Yu, X. Tu, R. Rusli, and G.-Q. Lo, Opt. Express **22**, 29978 (2014).

[258] C. Xiong, D. M. Gill, J. E. Proesel, J. S. Orcutt, W. Haensch, and W. M. J. Green, Optica **3**, 1060 (2016).

[259] S. Akiyama, T. Baba, M. Imai, T. Akagawa, M. Takahashi, N. Hirayama, H. Takahashi, Y. Noguchi, H. Okayama, T. Horikawa, and T. Usuki, Opt. Express **20**, 2911 (2012).

[260] I. Datta, S. H. Chae, G. R. Bhatt, M. A. Tadayon, B. Li, Y. Yu, C. Park, J. Park, L. Cao, D. N. Basov, J. Hone, and M. Lipson, Nat. Photonics **14**, 256 (2020).

[261] S. Dogru and N. Dagli, Opt. Lett. **39**, 6074 (2014).

[262] H. Agarwal, B. Terrés, L. Orsini, A. Montanaro, V. Sorianello, M. Pantouvaki, K. Watanabe, T. Taniguchi, D. V. Thourhout, M. Romagnoli, and F. H. L. Koppens, Nat. Commun. **12**, 1070 (2021).

[263] J. Gosciniak and D. T. H. Tan, Nanotechnology **24**, 185202 (2013).

[264] J. Gosciniak and D. T. H. Tan, Sci. Rep. **3**, 1897 (2013).

[265] K. J. A. Ooi, L. K. Ang, and D. T. H. Tan, Appl. Phys. Lett. **105**, 111110 (2014).

[266] D. Chatzidimitriou, A. Pitilakis, and E. E. Kriezis, J. Appl. Phys. **118**, 023105 (2015).

[267] B. Majérus, E. Dremetsika, M. Lobet, L. Henrard, and P. Kockaert, Phys. Rev. B **98**, 125419 (2018).

[268] C. Tserkezis, J. R. Maack, Z. Liu, M. Wubs, and N. A. Mortensen, Sci. Rep. **6**, 28441 (2016).

[269] J. Zuloaga, E. Prodan, and P. Nordlander, Nano Lett. **9**, 887 (2009).

[270] J. A. Scholl, A. García-Etxarri, A. L. Koh, and J. A. Dionne, Nano Lett. **13**, 564 (2013).

[271] G. Toscano, J. Straubel, A. Kwiatkowski, C. Rockstuhl, F. Evers, H. Xu, N. A. Mortensen, and M. Wubs, Nat. Commun. **6**, 7132 (2015).

[272] C. Reale, Infrared Phys. **10**, 173 (1970).

[273] S. Xian, L. Nie, J. Qin, T. Kang, C. Li, J. Xie, L. Deng, and L. Bi, Opt. Express **27**, 28618 (2019).

[274] J. W. Cleary, E. M. Smith, K. D. Leedy, G. Grzybowski, and J. Guo, Opt. Mater. Express **8**, 1231 (2018).

[275] F. Palumbo, C. Wen, S. Lombardo, S. Pazos, F. Aguirre, M. Eizenberg, F. Hui, and M. Lanza, Adv. Funct. Mater. **30**, 1900657 (2019).

[276] T. Li, T. Tu, Y. Sun, H. Fu, J. Yu, L. Xing, Z. Wang, H. Wang, R. Jia, J. Wu, C. Tan, Y. Liang, Y. Zhang, C. Zhang, Y. Dai, C. Qiu, M. Li, R. Huang, L. Jiao, K. Lai, B. Yan, P. Gao, and H. Peng, Nat. Electron. **3**, 473 (2020).

[277] L. A. Falkovsky and S. S. Pershoguba, Phys. Rev. B **76**, 153410 (2007).

[278] G. W. Hanson, J. Appl. Phys. **103**, 064302 (2008).

[279] C. Backes, A. M. Abdelkader, C. Alonso, A. Andrieux-Ledier, R. Arenal, J. Azpeitia, N. Balakrishnan, L. Banszerus, J. Barjon, R. Bartali, S. Bellani, C. Berger, R. Berger, M. M. B. Ortega, C. Bernard, P. H. Beton, A. Beyer, A. Bianco, P. Bøggild, F. Bonaccorso, G. B. Barin, C. Botas, R. A. Bueno, D. Carriazo, A. Castellanos-Gomez, M. Christian, A. Ciesielski, T. Ciuk, M. T. Cole, J. Coleman, C. Coletti, L. Crema, H. Cun, D. Dasler, D. D. Fazio, N. Díez, S. Drieschner, G. S. Duesberg, R. Fasel, X. Feng, A. Fina, S. Forti, C. Galiotis, G. Garberoglio, J. M. García, J. A. Garrido, M. Gibertini, A. Gölzhäuser, J. Gómez, T. Greber, F. Hauke, A. Hemmi, I. Hernandez-Rodriguez, A. Hirsch, S. A. Hodge, Y. Huttel, P. U. Jepsen, I. Jimenez, U. Kaiser, T. Kaplas, H. Kim, A. Kis, K. Papagelis, K. Kostarelos, A. Krajewska, K. Lee, C. Li, H. Lipsanen, A. Liscio, M. R. Lohe, A. Loiseau, L. Lombardi, M. F. López, O. Martin, C. Martín, L. Martínez, J. A. Martin-Gago, J. I. Martínez, N. Marzari, Á. Mayoral, J. McManus, M. Melucci, J. Méndez, C. Merino, P. Merino, A. P. Meyer, E. Miniussi, V. Miseikis, N. Mishra, V. Morandi, C. Munuera, R. Muñoz, H. Nolan, L. Ortolani, A. K. Ott, I. Palacio, V. Palermo, J. Parthenios, I. Pasternak, A. Patane, M. Prato, H. Prevost, V. Prudkovskiy, N. Pugno, T. Rojo, A. Rossi, P. Ruffieux, P. Samorì, L. Schué, E. Setijadi, T. Seyller, G. Speranza, C. Stampfer, I. Stenger, W. Strupinski, Y. Svirko, S. Taioli, K. B. K. Teo, M. Testi, F. Tomarchio, M. Tortello, E. Treossi, A. Turchanin, E. Vazquez, E. Villaro, P. R. Whelan, Z. Xia, R. Yakimova, S. Yang, G. R. Yazdi, C. Yim, D. Yoon, X. Zhang, X. Zhuang, L. Colombo, A. C. Ferrari, and M. Garcia-Hernandez, 2D Mater. **7**, 022001 (2020).

[280] W. Bogaerts, P. D. Heyn, T. V. Vaerenbergh, K. D. Vos, S. K. Selvaraja, T. Claes, P. Dumon, P. Bienstman, D. V. Thourhout, and R. Baets, Laser Photonics Rev. **6**, 47 (2011).

[281] T. Christopoulos, O. Tsilipakos, G. Sinatkas, and E. E. Kriezis, Opt. Express **27**, 14505 (2019).

[282] W. Yan, R. Faggiani, and P. Lalanne, Phys. Rev. B **97**, 205422 (2018).

[283] J.-K. Park, S. Takagi, and M. Takenaka, Opt. Express **26**, 4842 (2018).

[284] M. Takenaka, S. Takahashi, S. Takagi, J.-H. Han, F. Boeuf, J.-K. Park, Q. Li, C. P. Ho, D. Lyu, S. Ohno, and J. Fujikata, J. Lightwave Technol. **37**, 1474 (2019).

[285] W. Heni, Y. Fedoryshyn, B. Baeuerle, A. Josten, C. B. Hoessbacher, A. Messner, C. Haffner, T. Watanabe, Y. Salamin, U. Koch, D. L. Elder, L. R. Dalton, and J. Leuthold, Nat. Commun. **10**, 1694 (2019).

[286] J.-M. Sallese, Eur. Phys. J. B **89**, 136 (2016).

[287] T. Fang, A. Konar, H. Xing, and D. Jena, Appl. Phys. Lett. **91**, 092109 (2007).

[288] R. Jones, P. Doussiere, J. B. Driscoll, W. Lin, H. Yu, Y. Akulova, T. Komljenovic, and J. E. Bowers, IEEE Nanotechnol. Mag. **13**, 17 (2019).

[289] K. Nozaki, S. Matsuo, T. Fujii, K. Takeda, A. Shinya, E. Kuramochi, and M. Notomi, Nat. Photonics **13**, 454 (2019).

[290] A. Chen and E. Murphy, *Broadband Optical Modulators: Science, Technology, and Applications*, 1st ed. (CRC Press, Boca Raton, FL, 2012).

[291] S. Matsuo and T. Kakitsuka, Adv. Opt. Photonics **10**, 567 (2018).

[292] N. H. Zhu, Z. Shi, Z. K. Zhang, Y. M. Zhang, C. W. Zou, Z. P. Zhao, Y. Liu, W. Li, and M. Li, IEEE J. Sel. Top. Quantum Electron. **24**, 1 (2018).

[293] X. Dai, H. Debregeas, G. D. Rold, D. Carrara, K. Louarn, E. D. Valdeiglesias, and F. Lelarge, IEEE J. Sel. Top. Quantum Electron. **27**, 1 (2021).

[294] T. Yamamoto, in *Optical Fiber Communication Conference* (OSA, 2012).

[295] W. Kobayashi, T. Ito, T. Yamanaka, T. Fujisawa, Y. Shibata, T. Kurosaki, M. Kohtoku, T. Tadokoro, and H. Sanjoh, IEEE J. Sel. Top. Quantum Electron. **19**, 1500908 (2013).

[296] K. Nakahara, Y. Wakayama, T. Kitatani, T. Taniguchi, T. Fukamachi, Y. Sakuma, and S. Tanaka, IEEE Photonics Technol. Lett. **27**, 534 (2015).

[297] P. Moser, J. Lott, P. Wolf, G. Larisch, H. Li, N. Ledentsov, and D. Bimberg, Electron. Lett. **48**, 1292 (2012).

[298] E. Haglund, P. Westbergh, J. Gustavsson, E. Haglund, A. Larsson, M. Geen, and A. Joel, Electron. Lett. **51**, 1096 (2015).

[299] E. Simpanen, J. Gustavsson, E. Haglund, E. Haglund, A. Larsson, W. Sorin, S. Mathai, and M. Tan, Electron. Lett. **53**, 869 (2017).

[300] H.-Y. Kao, C.-T. Tsai, S.-F. Leong, C.-Y. Peng, Y.-C. Chi, J. J. Huang, H.-C. Kuo, T.-T. Shih, J.-J. Jou, W.-H. Cheng, C.-H. Wu, and G.-R. Lin, Opt. Express **25**, 16347 (2017).

[301] Y. Rao, W. Yang, C. Chase, M. C. Y. Huang, D. D. P. Worland, S. Khaleghi, M. R. Chitgarha, M. Ziyadi, A. E. Willner, and C. J. Chang-Hasnain, IEEE J. Sel. Top. Quantum Electron. **19**, 1701311 (2013).

[302] S. Spiga, D. Schoke, A. Andrejew, G. Boehm, and M.-C. Amann, J. Lightwave Technol. **35**, 3130 (2017).

[303] T. Sato, K. Takeda, A. Shinya, M. Notomi, K. Hasebe, T. Kakitsuka, and S. Matsuo, IEEE J. Sel. Top. Quantum Electron. **21**, 728 (2015).

[304] K. Takeda, T. Sato, A. Shinya, K. Nozaki, W. Kobayashi, H. Taniyama, M. Notomi, K. Hasebe, T. Kakitsuka, and S. Matsuo, Nat. Photonics **7**, 569 (2013).

[305] D. Miller, Proc. IEEE **97**, 1166 (2009).

[306] T. Fujii, K. Takeda, N.-P. Diamantopoulos, E. Kanno, K. Hasebe, H. Nishi, R. Nakao, T. Kakitsuka, and S. Matsuo, IEEE J. Sel. Top. Quantum Electron. **24**, 1 (2018).

[307] N. Haghighi, G. Larisch, R. Rosales, M. Zorn, and J. A. Lott, in *2018 IEEE International Semiconductor Laser Conference (ISLC)* (IEEE, 2018), pp. 1–2.

[308] S. Yamaoka, N.-P. Diamantopoulos, H. Nishi, R. Nakao, T. Fujii, K. Takeda, T. Hiraki, T. Tsurugaya, S. Kanazawa, H. Tanobe, T. Kakitsuka, T. Tsuchizawa, F. Koyama, and S. Matsuo, Nat. Photonics **15**, 28 (2020).

[309] P. E. F. Junior, G. Xu, J. Lee, N. C. Gerhardt, G. M. Sipahi, and I. Žutić, Phys. Rev. B **92**, 075311 (2015).

[310] M. Lindemann, G. Xu, T. Pusch, R. Michalzik, M. R. Hofmann, I. Žutić, and N. C. Gerhardt, Nature **568**, 212 (2019).

[311] A. N. R. Ahmed, S. Nelan, S. Shi, P. Yao, A. Mercante, and D. W. Prather, Opt. Lett. **45**, 1112 (2020).

[312] R. Safian, M. Teng, L. Zhuang, and S. Chakravarty, Opt. Express **28**, 25843 (2020).

[313] J. J. G. M. van der Tol, Y. Jiao, J. P. V. Engelen, V. Pogoretskiy, A. A. Kashi, and K. Williams, IEEE J. Quantum Electron. **56**, 1 (2020).

[314] C. P. Dietrich, A. Fiore, M. G. Thompson, M. Kamp, and S. Höfling, Laser Photon. Rev. **10**, 870 (2016).

[315] F. Y. Gardes, G. T. Reed, N. G. Emerson, and C. E. Png, Opt. Express **13**, 8845 (2005).

[316] H. Xu, J. Liu, J. Liu, C. Yu, Z. Zhai, G. Qin, and F. Liu, Mater. Chem. Front. **4**, 168 (2020).

[317] L. R. Dalton, D. L. Elder, L. E. Johnson, A. F. Tillack, and B. H. Robinson, Nonlinear Opt. Quantum Opt. **50**, 67 (2019).

[318] A. M. Spring, F. Qiu, J. Hong, A. Bannaron, T. Kashino, T. Kikuchi, M. Ozawa, H. Nawata, K. Odoi, and S. Yokoyama, Eur. Polym. J. **97**, 263 (2017).

[319] Z. Chen, Y. Zhuo, W. Tu, Z. Li, X. Ma, Y. Pei, and G. Wang, Opt. Express **26**, 22123 (2018).

[320] E. Sachet, C. T. Shelton, J. S. Harris, B. E. Gaddy, D. L. Irving, S. Curtarolo, B. F. Donovan, P. E. Hopkins, P. A. Sharma, A. L. Sharma, J. Ihlefeld, S. Franzen, and J.-P. Maria, Nat. Mater. **14**, 414 (2015).

[321] S. Campione, M. G. Wood, D. K. Serkland, S. Parameswaran, J. Ihlefeld, T. S. Luk, J. R. Wendt, K. M. Geib, and G. A. Keeler, IEEE Photonics J. **9**, 1 (2017).

[322] B. Wang, W. Huang, L. Chi, M. Al-Hashimi, T. J. Marks, and A. Facchetti, Chem. Rev. **118**, 5690 (2018).

[323] V. Sorianello, M. Midrio, and M. Romagnoli, Opt. Express **23**, 6478 (2015).

[324] A. Phatak, Z. Cheng, C. Qin, and K. Goda, Opt. Lett. **41**, 2501 (2016).

[325] Y. Meng, S. Ye, Y. Shen, Q. Xiao, X. Fu, R. Lu, Y. Liu, and M. Gong, IEEE Photonics J. **10**, 1 (2018).

[326] J. Su, X. He, and C. Li, J. Opt. Soc. Am. B **37**, 709 (2020).

[327] C. Lin, R. Grassi, T. Low, and A. S. Helmy, Nano Lett. **16**, 1683 (2016).

[328] R. Tarcan, O. Todor-Boer, I. Petrovai, C. Leordean, S. Astilean, and I. Botiz, J. Mater. Chem. C **8**, 1198 (2020).

[329] A. Joushaghani, J. Jeong, S. Paradis, D. Alain, J. S. Aitchison, and J. K. Poon, Photonics **2**, 916 (2015).